THESIS FOR THE DEGREE OF LICENTIATE OF ENGINEERING

On Control of Permanent-Magnet Synchronous Motors in Hybrid-Electric Vehicle Applications

OSKAR WALLMARK

Department of Electric Power Engineering
CHALMERS UNIVERSITY OF TECHNOLOGY
Göteborg, Sweden 2004

On Control of Permanent-Magnet Synchronous Motors in Hybrid-Electric Vehicle Applications
OSKAR WALLMARK

Technical Reports at the School of Electrical Engineering
Technical Report no. 495L
ISSN 1651-4998

Department of Electric Power Engineering
Chalmers University of Technology
SE–412 96 Göteborg
Sweden
Telephone +46 (0)31–772 1000

Cover: “Phase portrait”. Artist: AnnSofie Hahne. Compare also with Fig. 4.3.

Chalmers Bibliotek, Reproservice
Göteborg, Sweden 2004

To my grandmother Anna-Lisa Wallmark

On Control of Permanent-Magnet Synchronous Motors in Hybrid-Electric Vehicle Applications

OSKAR WALLMARK
Department of Electric Power Engineering
Chalmers University of Technology

Abstract

This thesis deals with design and analysis of the control system structure for electric drives equipped with permanent-magnet synchronous motors with a salient rotor. The intended application is propulsion in electric- and hybrid-electric vehicles. Particulary, sensorless control, meaning vector control without a mechanical rotor position sensor, is considered.

A speed and position estimator of phase-locked loop type, previously reported in the literature, is analyzed with respect to the salient rotor and impact of parameter errors. Modifications are proposed to allow for operation in the whole speed range and the estimator's capacity to handle large speed estimation errors is improved. As a result of the analysis, simple parameter selection rules are derived, reducing the amount of trial-and-error work required in the design and tuning of the drive.

A transient model taking harmonics into account is reviewed and its impact on current harmonics, when utilizing synchronous-frame PI current controllers, is investigated, both through simulations and experiments. Field-weakening operation is also considered. The closed-loop dynamics of a field-weakening controller, previously reported in the literature, is analyzed and verified experimentally, considering salient permanent-magnet synchronous motors.

The theory considering loss minimization, by means of control, is reviewed and some analytical results are presented which can function as a useful tool when designing the control system of any electrical drive consisting of a permanent-magnet synchronous motor and corresponding inverter.

Index Terms: Electric drive, electric vehicle, harmonics, hybrid-electric vehicle, permanent-magnet synchronous motor, phase-locked loop, position estimation, sensorless control, signal injection, speed estimation, vector control.

Acknowledgements

This research project was fully funded by the Swedish National Energy Administration, within the “Energisystem i vägfordon” research program, which is gratefully acknowledged.

I would like to thank my supervisors Assoc. Prof. Ola Carlson, for help and encouragement, and Prof. Lennart Harnefors, for excellent technical guidance, encouragement, and for persistently revising the manuscript.

I also would like to thank my examiner, Prof. Tore Undeland, and all my colleagues at the department who have assisted me during the work on this thesis, particulary Dr. Rolf Ottersten and Tech. Lic. Andreas Peterson, for good companionship and fruitful discussions regarding my project.

I further would like to thank my family, including my grandmother, Anna-Lisa Wallmark; this thesis is dedicated to you. Last, but surely not least, I would like to thank my fiancée AnnSofie Hahne for her endless love and support.

Oskar Wallmark
Gothenburg, Sweden
February, 2004

Contents

Chapter 1

Introduction

In this chapter, the concept of electric propulsion is briefly reviewed. The focus is put on the electrical drive system, consisting of an electric machine and corresponding power electronics. The outline of the thesis, as well as scientific contributions, are also presented.

1.1 Why Hybrid Electric Vehicles?

The electric vehicle (EV) concept was invented in 1834 and has thus been around for almost 200 years. However, the EV had almost vanished from the market by 1930. This was mainly because of insufficient range, due to limited battery capacity, as compared to vehicles equipped with internal combustion engines (ICEs); a technology that was evolving rapidly at that time [11]. A more mature generation of EVs was born in 1996 when General Motors Corporation leased their EV, named EV-1, to customers in selected states of the U.S.A. Unfortunately, once again, the attempt to introduce EVs to normal customers failed due to limited range [36].

As the demand for more environmental-friendly cars continues to grow, originating from both individual customers, as well as driven by governmental means, the failure of EVs has set the stage for the hybrid electric vehicle (HEV). In an HEV, the ICE is combined with electric propulsion. This provides several possible advantages, at the cost of increased complexity. The main advantages are increased range (as compared to EVs), the potential to operate the ICE at optimal (maximization of fuel economy, minimized emissions or a compromise between both) operating points and the use of regenerative braking. During regenerative braking, the energy used to slow or halt the vehicle is converted into electricity, which can charge the built-in battery, rather than wasting it as heat.

1.2 HEV Configurations

Combining an ICE with electrical propulsion can be done in numerous ways. However, the different types of HEV configurations can be classified into two basic kinds: series and parallel configurations, or a combination of both. The configuration that is optimal is indeed a complicated matter and is currently an active field of research [13, 35]. Below, only the basic fundamentals of each configuration will be described. The *mild hybrid* concept consists of an ICE assisted by a starter/generator fed by a 42-V electrical system [36]. The starter/generator cannot move the vehicle by itself, but it can assist propulsion and recover energy through regenerative braking. Although basically the same technology is used in the electrical system (only at lower power levels), the mild hybrid concept is not considered in this thesis.

1.2.1 Series Configuration

In the series configuration, as shown in Fig. 1.1, there is no mechanical connection between the ICE and the transmission. The power delivered by the ICE is converted to electrical power by the generator. This power can be used for propulsion or for charging the battery. Advantages of this type of configuration include the potential to choose the operating point of the ICE freely (even turn it off in zero-emission zones), and the flexibility of locating the ICE and generator set. The main disadvantages are the increased number of energy conversions (as compared to the parallel configuration described below) and that all devices need to be sized for the maximum sustained power if the HEV is designed to climb a long grade, potentially making the configuration more expensive than the parallel configuration.

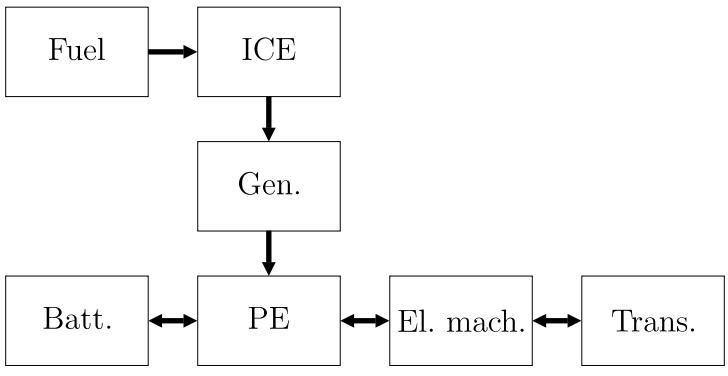

Fig. 1.1 Series configuration. The arrows indicate possible directions of energy flow. For a list of abbreviations, see Appendix E.

1.2.2 Parallel Configuration

In the parallel configuration, the propulsion power may be supplied by the ICE alone, by the electric machine alone or both. In comparison to the series configuration, the electric machine and ICE can be of a smaller scale (provided that the battery is not depleted). Even for long-range operation, only the ICE needs to be rated for peak power while the rating of the electric machine can be significantly lower. Another advantage is the removal of the generator which simplifies the configuration. Variants including an additional generator (also known as the series-parallel configuration), indicated by the dashed box in Fig. 1.2, also exist.

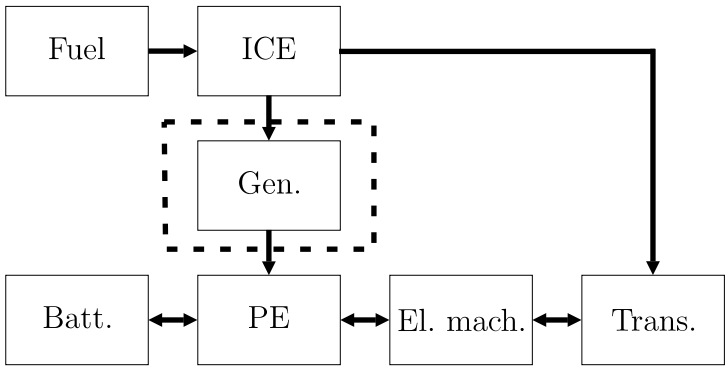

Fig. 1.2 Parallel configuration. The arrows indicate possible directions of energy flow.

1.3 Electric Machines in HEV Applications

In order to achieve a high efficiency of the whole drive, each part has to be designed with respect to all other components so that total losses really are minimized. A key component in any HEV configuration is the electric machine(s). Naturally, an additional limitation in this optimization procedure is cost, which makes the design stage of the electric machine even more complicated. Today, induction machines (IMs) and permanent-magnet machines are the most common types [11], although switched reluctance (due to their low cost and potential to operate in wide constant-power ranges [31, 72]) and reluctance synchronous machines have also been shown to be suitable candidates for EV and HEV applications [52].

1.3.1 Permanent-Magnet Machines

Permanent-magnet machines are, due to their high efficiency, power density and torque-to-inertia ratio, a common choice (perhaps the most common) in HEV con-

cepts. In an HEV application, the electric machine must operate at varying loads and speeds. This requires a careful selection of motor parameters by the machine designer, in order to minimize losses [23]. Permanent-magnet machines are, depending on the supply voltage waveform, divided into brushless dc machines with trapezoidal voltage waveforms and permanent-magnet synchronous machines (PMSMs) with sinusoidal waveforms. Both types are found in HEVs, such as the Honda Insight, in which a brushless dc machine is used [21] or the Toyota Prius, which utilizes a PMSM [82]. There are numerous references that present PMSM designs developed for EV and HEV applications; some examples are [15, 30, 56]. In many of these designs, and in agreement with the literature review in [28], the rotors possess saliency, i.e., the difference between the d- and q-axis inductances is significant, which allows for the utilization of the reluctance torque [23, 30].

1.4 Control of PMSMs in HEV Applications

At the Department of Electric Power Engineering at Chalmers University of Technology, Sweden, a PMSM and a voltage source inverter (VSI) have previously been developed for a series HEV [28, 45]. The PMSM is designed for a continuous output power of 50 kW and the nominal speed is 6000 rpm. A digital signal processor (DSP) is used for control of the VSI. See Appendix B for further details on the experimental setup.

A modern DSP is inexpensive and its computational capacity allows for complicated control algorithms to be executed at each sample step. Therefore, once the PMSM and VSI are developed, there are few reasons not to control the setup in an "optimal" manner. Through control, several factors can be affected. The PMSM and VSI are typically developed for maximum efficiency, although a limit set by cost may add additional constraints. However, an inaccurate control algorithm can reduce the efficiency significantly. The current controller plays a significant role since it governs the electro-mechanical torque on the shaft of the PMSM. Expressing the stator current in the rotor-fixed dq-coordinate system (see Chapter 2), the number of possible combinations of the d- and q-direction current components that produce the same electro-mechanical torque is infinite. The current references should preferably be chosen so that the combined losses of both the PMSM and the VSI are minimized. The requirement on fast dynamic response is of minor significance since the vehicle dynamics are much slower than the electrical dynamics. However, the desired electro-mechanical torque should be reached as quickly as possible, at any

speed, to guarantee that performance will not deteriorate. As will be seen in Chapter 4, achieving sensorless control (see below) with high accuracy also requires fast and accurate current control at all possible operating points.

As the magnetization from the stator must be synchronized with the rotor magnet, knowledge of the rotor position is needed for correct operation. Therefore, a rotor position sensor, typically a digital position encoder or a resolver,[1] is often mounted on the shaft of the PMSM. Naturally, the additional hardware this requires adds complexity to the system. Although the cost of the sensor and the corresponding hardware can be reduced, operation without a rotor position sensor, i.e., *sensorless control*, is attractive since there will be no additional cost for the sensor. Due to the large quantities that a popular vehicle is produced in, removing even a low cost can be attractive and allows the manufacturer to save a significant amount of money.

1.5 Outline of Thesis

This thesis considers "optimal" operation of salient PMSMs by means of control. The term "optimal" means both operation with minimized losses, of both the PMSM and the VSI, and also operation without a rotor position sensor, since this reduces the cost of the drive. As the goal is to develop control algorithms that can be used on any setup of PMSM and VSI, the algorithms must be analyzed with respect to different setups of motor parameters and parameter variations, rather than just demonstrating the performance of the algorithm on a single, well tuned, experimental setup.

Chapter 2 therefore focuses on modeling (for control purposes) and design of controllers of salient PMSMs. Focus is on the impact of harmonics that arise if the magnet fields from the rotor and stator winding are not perfectly sinusoidal. Chapter 3 discusses operation with minimized losses, by means of control. The main part of the thesis consists of Chapter 4, which considers sensorless control of salient PMSMs with an emphasis on EV/HEV applications. It is the author's desire that the thesis also functions as a "cookbook," to be utilized when implementing a vector controlled PMSM (with or without rotor position sensor) in a vehicle application.

[1] The Toyota Prius Mark II uses the "Singlsyn" resolver manufactured by Tamagawa Seiki company [55].

1.5.1 Contributions

The main scientific contributions in this thesis, presented in Chapter 4, are in the field of sensorless control of salient PMSMs, where the speed and position estimator presented in [26] is analyzed further, considering the impact of saliency and operation in the whole speed region. A technique is also proposed to improve the estimator's capability to handle large speed estimation errors. Following the analysis and modifications, simple parameter selection rules are derived, reducing the amount of trial-and-error work required in the design and tuning of the drive.

The case study concerning loss minimization, by means of control, is mainly based on previously presented theory, of which some are referenced in Chapter 3. However, some observations and results are given, which are believed not to be well known.

An analysis of the field-weakening controller presented in [27] (which originates from [41]) is presented in Chapter 2. The analysis is similar to the results presented in [27] (which deals with induction motors) but salient PMSMs are considered. The impact of harmonics (due to harmonics in inductances and magnet flux linkage) on the current controller presented in [25] is also highlighted.

1.5.2 Publications

In chronological order, with references where the papers appear in the thesis, the publications originating from this project are:

1. O. Wallmark. "Modelling of permanent magnet synchronous machines with non-sinusoidal flux linkage," in *Proc. IEEE Nordic Workshop Power and Ind. Electron.*, 2002.
   This paper, mainly of tutorial nature, discusses aspects of modeling, for control purposes, of PMSMs with a non-sinusoidal magnet flux linkage. The results are extended in Chapter 2 of this thesis.

2. O. Wallmark, L. Harnefors, and O. Carlson. "An improved speed and position estimator for salient permanent-magnet synchronous motors," submitted to *IEEE Trans. Ind. Electron.*
   The main results of this thesis are presented in this paper, which presents a method to improve the capability to handle large estimation errors of the speed and position estimator presented in [26]. A simple modification of the original algorithm is made so that operation in the whole speed region is possible. The results are also presented in Chapter 4 of this thesis.

3. O. Wallmark, L. Harnefors, and O. Carlson. “Sensorless control of PMSM drives for hybrid electric vehicles,” accepted to *IEEE PESC’04*.
   In this paper, the impact of saliency of the estimator presented in [26] is considered further. The results are also found in Chapter 4 of this thesis.

4. O. Wallmark, O. Carlson, and L. Harnefors. “Loss minimization of a PMSM drive for a hybrid electric vehicle,” submitted to *EPE PEMC’04*.
   This paper presents a case study of operation with minimized losses, by means of control of a PMSM and corresponding power electronics, developed for an HEV application. The results are also found in Chapter 3 of this thesis.

Chapter 2

Modeling of Permanent-Magnet Synchronous Motors

In this chapter, different aspects of modeling of PMSMs for control purposes are described; see Appendix E for a list of glossary terms. The intention is to demonstrate significant properties that affect the control characteristics of torque controlled PMSMs. The current and field-weakening controllers implemented in the experiments are also discussed together with various implementation issues.

2.1 A PMSM Model Taking Harmonics into Account

In order to present a detailed model of a PMSM, several properties of geometry (lack of symmetry), materials (non-linear material parameters) and operating environment have to be taken into account. Because of this, finite element methods often have to be utilized. However, for control purposes, much simpler models can be relied on due to the use of feedback in the closed-loop control. The controller suppresses the impact of several phenomena and only a few, key properties of the PMSM have to be taken into account when designing the controller. In this section, modeling of PMSMs for control purposes will be discussed.

The fact that three-phase symmetrical sinusoidal quantities are transformed into two dc components through the well known Park transformation, has made modeling of PMSMs in the rotor-fixed dq-reference frame used almost exclusively for control purposes. Capturing the most important phenomena, the current and mechanical dynamics can be described as a simple third-order, bilinear system, in which currents and voltages are constant under steady-state conditions. Additional properties, such as harmonics and core losses, can easily be incorporated into the

model.

2.1.1 The Park Transformation

For symmetrical conditions, the Park transformation transforms three-phase components, f_a, f_b, and f_c, which can be either currents, voltages or fluxes, into two-variable quantities, f_d and f_q [42]. For motor control purposes, the transformation angle, θ, is typically the angle between f_a and the d-axis, as shown in Fig. 2.1. For PMSMs, it is common to align the d-axis with the magnetic north pole of the rotor magnet (or, for sensorless control, an estimation thereof). In case of multipole machines, the electrical rotor angle is used. Collecting the phase and dq-quantities into

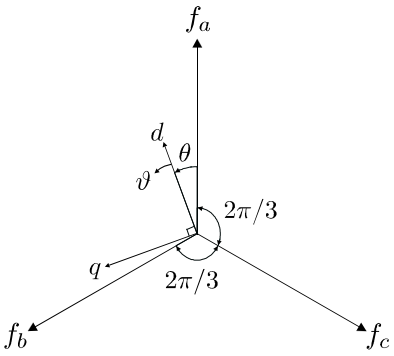

Fig. 2.1 Three-phase quantities and the dq-coordinate system. The transformation angle, θ, is the angle between f_a and the d-axis. The angle ϑ (see below) is fixed to the d-axis.

vectors, the Park transformation is given by $[f_d\ f_q\ f_0]^T = \mathbf{T}_{dq,\mathrm{ph}}[f_a\ f_b\ f_c]^T$, where $\mathbf{T}_{dq,\mathrm{ph}}$ is known as the Park-transformation matrix and f_0 is the zero-sequence component, defined as

$$f_0 = f_a + f_b + f_c. \tag{2.1}$$

Thus, f_0 is nonzero only under non-symmetrical conditions, which typically arise under fault conditions. These types of conditions are not covered in this work, so f_0 will be assumed to be zero throughout the thesis.

The Park-transformation matrix is defined as

$$\mathbf{T}_{dq,\mathrm{ph}} = K \begin{bmatrix} \cos\theta & \cos(\theta - 2\pi/3) & \cos(\theta + 2\pi/3) \\ -\sin\theta & -\sin(\theta - 2\pi/3) & -\sin(\theta + 2\pi/3) \\ 1/2 & 1/2 & 1/2 \end{bmatrix} \tag{2.2}$$

where the scaling constant K is chosen $K = 2/3$, which yields an amplitude-invariant transformation. This implies that for any constant set of f_d and f_q (and

$f_0 = 0$), f_a, f_b, and f_c are symmetrical sinusoids which amplitudes are given by $\sqrt{f_d^2 + f_q^2}$. Choosing the scaling constant differently, power-invariant or rms-invariant scalings are also possible to define. However, amplitude-invariant scaling is perhaps the most common choice for control of PMSMs. It is the opinion of the author that the main advantage of using amplitude-invariant Park transformation is that during experiments, if the d-current is set to zero (which is a common choice when controlling PMSMs), the q-current is directly obtained by simply measuring the peak value (using a current sensor connected to an oscilloscope for example) of any of the phase currents.

2.1.2 Stator Flux Linkage

Depending on the specific rotor structure, the radial flux-density distribution produced by the rotor magnets, will be more or less ideal, i.e., of sinusoidal shape. Fig. 2.2 shows a schematic design of a four-pole rotor of inset magnet type, where the d-axis is aligned to a north pole rotor magnet. For a rotor structure of this type, the radial flux density can be approximated as in Fig. 2.3 (the rotor magnet angle ϑ, which is fixed to the d-axis, is also shown in Fig. 2.4. It can be expanded into a Fourier series as

$$B_r(\vartheta) = \sum_{i=1}^{\infty} B_{2i-1} \cos\left[(2i-1)\vartheta\right] \tag{2.3}$$

where $B_i = \frac{4\hat{B}}{\pi i} \sin(i\tau_m/2)$, $\hat{B} = B_r(0)$ and τ_m is the magnet pitch, expressed in electrical radians.[1]

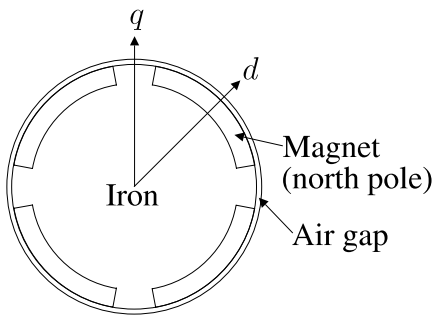

Fig. 2.2 Schematic design of a four pole rotor of inset magnet type.

Fig. 2.4 shows a simple type of three-phase stator winding. As the impact of harmonics will be investigated, this type of winding is suitable for modeling purposes

[1]For the machine used in the experiments, $\tau_m = 0.65\pi$.

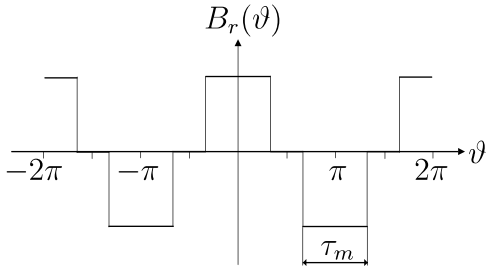

Fig. 2.3 Approximate radial flux-density distribution in the air gap for a rotor of inset magnet type.

instead of a sinusoidally distributed winding, or variants thereof. With this type of stator winding, and the assumption that the flux density distribution is radial only, the expression for the magnet flux linkage in phase a can be expressed as

$$\psi_{m,a}(\theta) = \int_{-(\theta+\frac{\pi}{2})}^{-(\theta-\frac{\pi}{2})} B_r(\vartheta) r_s l_s d\vartheta \tag{2.4}$$

where r_s is the inner radius of the stator and l_s is the stator length [29]. Evaluating the integral using (2.3) yields

$$\psi_{m,a}(\theta) = 2 r_s l_s \sum_{i=1}^{\infty} \frac{(-1)^{i+1} B_{2i-1}}{2i-1} \cos\left((2i-1)\theta\right). \tag{2.5}$$

Eq. (2.5) shows that the flux linkage from the rotor magnets in the stator winding

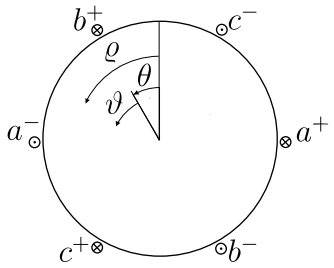

Fig. 2.4 Simplified model of the stator winding.

can be expressed as a sum of odd cosines where the amplitude of each harmonic decreases rapidly. This expression was derived assuming the flux-density distribution to have only the radial component given by (2.3) and using the simplified stator winding shown in Fig. 2.4. Depending on the specific stator winding and magnet configuration, this filtering property can be altered by the machine designer [29]. Thus,

$$\psi_{m,a}(\theta) = \psi_1 \cos\theta + \psi_3 \cos 3\theta + \psi_5 \cos 5\theta + \cdots \tag{2.6}$$

where the amplitude of the fundamental and each harmonic depends on the specific design of the rotor magnet configuration and stator winding.

From Figs. 2.1–2.4, it can be seen that the flux linkage in each phase from the rotor magnets can be expressed in vector form as

$$\begin{bmatrix}\psi_{m,a}(\theta)\\ \psi_{m,b}(\theta)\\ \psi_{m,c}(\theta)\end{bmatrix} = \begin{bmatrix}\psi_{m,a}(\theta)\\ \psi_{m,a}(\theta-2\pi/3)\\ \psi_{m,a}(\theta+2\pi/3)\end{bmatrix} = \boldsymbol{\psi}_{m,\mathrm{ph}}. \tag{2.7}$$

Remark: For completeness, it is useful to calculate the flux linkage assuming an ideal sinusoidally distributed winding. In this case, the number of conductors can be expressed as a function of the angle ϱ, see Fig. 2.4, as $N(\varrho) = (N_s/2)\sin\varrho$, where N_s is the number of (series) turns in the phase. The contribution of flux linkage of the winding at the angle ϱ is then given by [29]

$$d\psi_{m,a} = N(\varrho)d\varrho \int_{-(\varrho+\theta)}^{\varrho-\theta} B_r(\vartheta) r_s l_s d\vartheta. \tag{2.8}$$

Note that this integral can be expressed as the sum of integrals containing the flux linkage of the fundamental and each harmonic of $B_r(\vartheta)$. The total flux linkage is then found as

$$\psi_{m,a}(\theta) = \int_0^{\pi} d\psi_{m,a} = \frac{\pi r_s l_s N_s B_1}{2}\cos\theta. \tag{2.9}$$

As shown, no contribution from the harmonics in $B_r(\vartheta)$ are found in $\psi_{m,a}(\theta)$. Hence, for an ideal sinusoidal stator winding, the flux linkage from the rotor in the stator winding will only contain the fundamental [29].

Fig. 2.5 shows a measurement of the open-circuit voltage v_a at $\omega_r \approx 0.1$ pu for the PMSM used in the experiments. As shown, the open-circuit voltage is not perfectly sinusoidal and contains low-order harmonics (the influence of the stator slotting can also be clearly seen). Naturally, these harmonics will affect the current, causing it to be of a less sinusoidal shape (see Section 2.2).

2.1.3 Inductance Expressions

Typically, the magnetic permeability of the rotor magnet material is approximately the same as air [29]. Hence, the parts of the stator that are aligned to a rotor magnet "see" a wider air gap, that yields a rotor angle dependence of the stator phase self

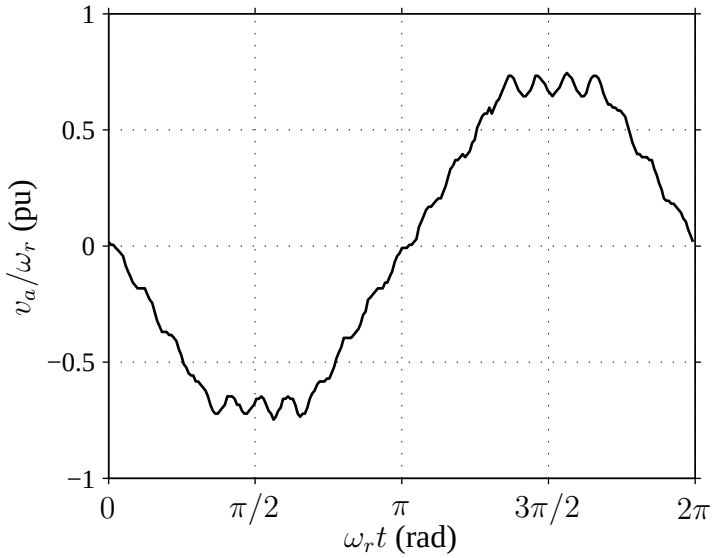

Fig. 2.5 Measured open-circuit voltage v_a/ω_r at $\omega_r \approx 0.1$ pu.

inductances. Fig. 2.6 shows the inductance measured using an inductance meter in phase a of the PMSM used in the experiments. As can be seen, the inductance is at a minimum when the rotor is aligned in the direction of the stator flux in phase a. The continuous line is a least-squares approximation that takes the second and fourth harmonics into account. Thus, the angular dependency of the self inductances can, at least under non-saturated conditions, be approximated as [47]

$$L_{s,a}(\theta) \approx L_{s,0} + L_{s,2}\cos 2\theta + L_{s,4}\cos 4\theta \tag{2.10a}$$

$$L_{s,b}(\theta) = L_{s,a}(\theta - 2\pi/3) \tag{2.10b}$$

$$L_{s,c}(\theta) = L_{s,a}(\theta + 2\pi/3). \tag{2.10c}$$

Similary, the mutual inductances between the phases are [47]

$$L_{m,ab}(\theta) = L_{m,ba}(\theta) \approx L_{m,0} + L_{m,2}\cos(2\theta - 2\pi/3) + L_{m,4}\cos(4\theta + 2\pi/3) \tag{2.10d}$$

$$L_{m,ac}(\theta) = L_{m,ca}(\theta) \approx L_{m,0} + L_{m,2}\cos(2\theta + 2\pi/3) + L_{m,4}\cos(4\theta - 2\pi/3) \tag{2.10e}$$

$$L_{m,bc}(\theta) = L_{m,cb}(\theta) \approx L_{m,0} + L_{m,2}\cos 2\theta + L_{m,4}\cos 4\theta \tag{2.10f}$$

where the expressions for the mutual inductances have also been truncated to contain harmonics only up to the fourth order. These inductance expressions can be

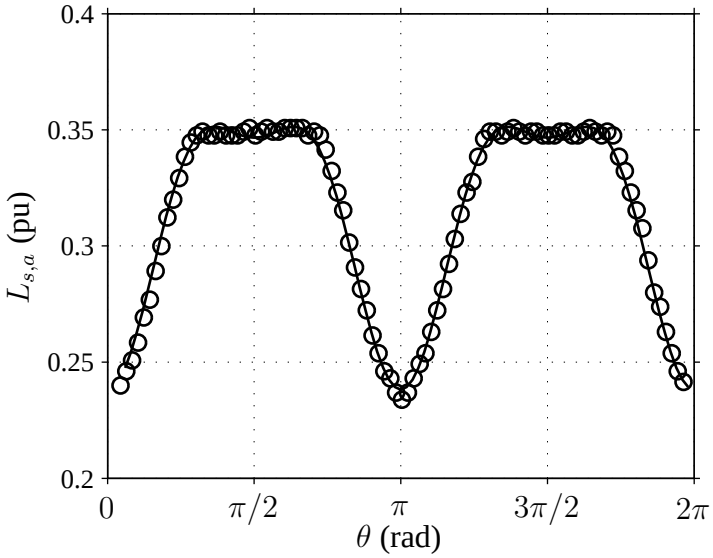

Fig. 2.6 Inductance $L_{s,a}(\theta)$. Circles (○) indicate measured values.

collected into a symmetric inductance matrix, $\mathbf{L}_{\mathrm{ph}}$, as

$$\mathbf{L}_{\mathrm{ph}} = \begin{bmatrix} L_{s,a}(\theta) & L_{m,ab}(\theta) & L_{m,ac}(\theta) \\ L_{m,ba}(\theta) & L_{s,b}(\theta) & L_{m,bc}(\theta) \\ L_{m,ca}(\theta) & L_{m,cb}(\theta) & L_{s,c}(\theta) \end{bmatrix}. \tag{2.11}$$

2.1.4 Current Dynamics

Using (2.7) and (2.11), the voltage equation in each phase can be expressed in matrix form, which yields

$$\mathbf{v}_{\mathrm{ph}} = \frac{d}{dt}\left(\mathbf{L}_{\mathrm{ph}}\mathbf{i}_{\mathrm{ph}} + \boldsymbol{\psi}_{m,\mathrm{ph}}\right) + R_s\mathbf{i}_{\mathrm{ph}} \tag{2.12}$$

where R_s is the phase resistance in each phase. Eq. (2.12) describes the open-loop current dynamics in each phase. However, for control purposes, this equation is far from ideal since the steady-state currents are of sinusoidal shape unless $\omega_r = d\theta/dt = 0$ rad/s. Current control utilizing PI controllers are common in electric drives. As they are inherently incapable of giving a zero steady-state control error for a sinusoidal reference, the Park transformation is applied to (2.12), which results in

$$\mathbf{v}_{dq} = \mathbf{T}_{dq,\mathrm{ph}}\frac{d}{dt}\left(\mathbf{L}_{\mathrm{ph}}\mathbf{T}_{dq,\mathrm{ph}}^{-1}\mathbf{i}_{dq} + \boldsymbol{\psi}_{m,\mathrm{ph}}\right) + R_s\mathbf{i}_{dq}. \tag{2.13}$$

Assuming that no zero-sequence component exists, the d- and q-components of (2.13) can, in matrix form, be reexpressed as[2]

$$\mathbf{v}_{dq} = \mathbf{L}_{dq}\frac{d\mathbf{i}_{dq}}{dt} + \mathbf{Z}_{dq}\mathbf{i}_{dq} + \omega_r\boldsymbol{\psi}_{m,dq} \tag{2.14}$$

where $\mathbf{L}_{dq}$, $\mathbf{Z}_{dq}$, and $\boldsymbol{\psi}_{m,dq}$ are given by

$$\mathbf{L}_{dq} = \begin{bmatrix} L_d + \frac{L_6}{5}\cos 6\theta & -\frac{L_6}{5}\sin 6\theta \\ -\frac{L_6}{5}\sin 6\theta & L_q - \frac{L_6}{5}\cos 6\theta \end{bmatrix} \tag{2.15a}$$

$$\mathbf{Z}_{dq} = \begin{bmatrix} R_s - \omega_r L_6 \sin 6\theta & -\omega_r L_q - \omega_r L_6 \cos 6\theta \\ \omega_r L_d - \omega_r L_6 \cos 6\theta & R_s + \omega_r L_6 \sin 6\theta \end{bmatrix} \tag{2.15b}$$

$$\boldsymbol{\psi}_{m,dq} = \begin{bmatrix} \sum_{i=1}^{\infty} \psi_{d,6i} \sin(6i\theta) \\ \psi_m + \sum_{i=1}^{\infty} \psi_{q,6i} \cos(6i\theta) \end{bmatrix}. \tag{2.15c}$$

Here, the notation

$$L_d = L_{s,0} + L_{s,2}/2 - L_{m,0} + L_{m,2} \tag{2.16a}$$

$$L_q = L_{s,0} - L_{s,2}/2 - L_{m,0} - L_{m,2} \tag{2.16b}$$

$$L_6 = 5\left(\frac{L_{s,4}}{2} + L_{m,4}\right) \tag{2.16c}$$

$$\psi_m = \psi_1 \tag{2.16d}$$

is introduced and the flux-linkage harmonics, expressed in the dq-reference frame, are, using (2.6), given by

$$\psi_{d,6i} = -(6i-1)\psi_{6i-1} - (6i+1)\psi_{6i+1},\ i = 1, 2, \ldots \tag{2.16e}$$

$$\psi_{q,6i} = -(6i-1)\psi_{6i-1} + (6i+1)\psi_{6i+1},\ i = 1, 2, \ldots \tag{2.16f}$$

If all harmonics (flux linkage and inductance) are neglected, (2.14) can be simplified significantly and the d- and q-components can be found as

$$v_d = R_s i_d + L_d\frac{di_d}{dt} - \omega_r L_q i_q \tag{2.17}$$

$$v_q = R_s i_q + L_q\frac{di_q}{dt} + \omega_r L_d i_d + \omega_r \psi_m \tag{2.18}$$

which is the standard model (for control purposes) of the current dynamics for a salient PMSM. Eqs. (2.17) and (2.18) are very attractive for control purposes since

[2] Since zero-sequence components are not considered in the present thesis, they are, in most cases, removed from the notation of current and voltage vectors. For example, the vector $\mathbf{i}_{dq}$ typically only contains two components, $\mathbf{i}_{dq} = [i_d\ i_q]^T$.

no angular-dependent sinusoids are present. The harmonics can be considered as disturbances, causing additional ripple in the controlled d- and q-currents.

Using (2.14) and (2.15), it is apparent that the flux-linkage harmonics will produce voltage harmonics that increase with speed and will not be dependent on the magnitude of the current. The inductance harmonics, on the other hand, will cause voltage harmonics which magnitudes will increase with increased current. For example, it can be expected that in a current-controlled PMSM with $i_d^{\text{ref}} = 0$, harmonics will still arise in i_d, depending on the magnitude of i_q, due the coupling term $-\omega_r L_6 \cos 6\theta$ in the first row and second column of $\mathbf{Z}_{dq}$.

The flux-linkage harmonics, expressed in dq-coordinates, can be identified by simply measuring the phase-to-neutral voltages[3] while rotating the motor at a constant speed and then performing a dq-transformation in order to obtain v_d and v_q. The flux-linkage harmonics, $\psi_{d,6i}$ and $\psi_{q,6i}$, are then obtained by identifying the harmonics of v_d/ω_r and v_q/ω_r, respectively. For a full sensorless drive, no rotor position sensor is mounted and, in such a case, (2.16e) and (2.16f) can be used to obtain the flux-linkage harmonics expressed in dq-coordinates.

Since the flux linkage due to the permanent magnets is dependent on the operating temperature [29], measuring the flux-linkage harmonics in this way will only yield approximate values. However, this is sufficient in order to determine their impact on torque and current ripple. Typically, only the first two or three harmonics (6, 12, and 18 in dq-coordinates) are of interest.

2.1.5 Mechanical Dynamics

Assuming a stiff shaft, the mechanical dynamics are governed by the simple relation

$$J\frac{d\omega_m}{dt} = T_e - T_L - T_{\text{fric}} \tag{2.19}$$

where J is the moment of inertia as seen from the rotor side, ω_m the mechanical rotor speed, T_e the electro-mechanical torque, T_L the load torque and T_{fric} the friction torque arising in bearings, gearbox, etc.

In a vehicle application where the PMSM is used for propulsion, the inertia can be considered very large, efficiently damping any torque ripples that may be produced by the PMSM, although the ripple will still add to the mechanical wear in the transmission. However, in order to complete the derivation of the PMSM model

[3] If the neutral point is not available, the two line-to-line voltages $v_a - v_b$ and $v_c - v_a$ can be measured and the phase-to-neutral voltage is then obtained using $(v_a - v_b) - (v_c - v_a) = v_a - v_b - v_c + v_a = 3v_a$.

and gain further understanding, it can still be useful to calculate an expression for the electro-mechanical torque, taking both flux linkage- and inductance harmonics into account.

In three-phase quantities and assuming linear magnetic conditions, the magnetic coenergy, W, is given by [42]

$$W = \frac{1}{2}\mathbf{i}_{\mathrm{ph}}^T \mathbf{L}_{\mathrm{ph}} \mathbf{i}_{\mathrm{ph}} + \mathbf{i}_{\mathrm{ph}}^T \boldsymbol{\psi}_{m,\mathrm{ph}}. \tag{2.20}$$

Hence, the torque expression is given by [29, 42]

$$T_e(\theta) = \frac{\partial W}{\partial \theta_m} = n_p \frac{\partial W}{\partial \theta} = n_p \left(\frac{1}{2}\mathbf{i}_{\mathrm{ph}}^T \frac{\partial \mathbf{L}_{\mathrm{ph}}}{\partial \theta} \mathbf{i}_{\mathrm{ph}} + \mathbf{i}_{\mathrm{ph}}^T \frac{\partial \boldsymbol{\psi}_{m,\mathrm{ph}}}{\partial \theta} \right). \tag{2.21}$$

Transforming (2.21) into the dq-coordinate system yields

$$T_e(\theta) = n_p \left(\frac{1}{2} \left(\mathbf{T}_{dq,\mathrm{ph}}^{-1} \mathbf{i}_{dq} \right)^T \frac{\partial \mathbf{L}_{\mathrm{ph}}}{\partial \theta} \mathbf{T}_{dq,\mathrm{ph}}^{-1} \mathbf{i}_{dq} + \left(\mathbf{T}_{dq,\mathrm{ph}}^{-1} \mathbf{i}_{dq} \right)^T \frac{\partial \boldsymbol{\psi}_{m,\mathrm{ph}}}{\partial \theta} \right). \tag{2.22}$$

Introducing $\Delta L = L_q - L_d$ and truncating (2.22) to containing inductance harmonics up to the sixth order and flux-linkage harmonics up to order 12, (2.22) can be expressed as

$$\begin{aligned} T_e(\theta) = \frac{3n_p}{2} \Big[& \psi_m i_q - \Delta L i_d i_q - \frac{2}{5} L_6 \left((i_q^2 - i_d^2) \sin 6\theta + 2 i_d i_q \cos 6\theta \right) \\ & + i_d \left(\psi_{d,6} \sin 6\theta + \psi_{d,12} \sin 12\theta \right) + i_q \left(\psi_{q,6} \cos 6\theta + \psi_{q,12} \cos 12\theta \right) \Big]. \end{aligned} \tag{2.23}$$

The first term on the right-hand side of (2.23) is the main torque-producing component. The second term is known as the *reluctance torque* and is nonzero only if the machine possesses saliency ($\Delta L \neq 0$). Thus, for a salient machine, this torque can be utilized to obtain a larger torque for a given q-current. The other terms arise due to the harmonics in inductance and flux linkage and are dependent on the rotor position, θ. Thus, they will produce torque ripple even at constant d- and q-currents.

Eq. (2.23) demonstrates that removing torque ripple through control action is challenging for two reasons. First, some kind of estimation algorithm is needed to estimate the amplitude of the harmonics (in the general case, both in inductance and flux linkage) correctly since they will vary with shifting operation conditions (temperature and current variations). Second, an accurate current controller is needed in order to follow the desired current references that will be far from constant. This is especially challenging at high speeds.

Novelty of the PMSM model presented here, (2.22) and (2.14), is not claimed; it has been used in several applications where the object is torque-ripple minimization. Examples are [12, 16, 69, 79] where only [16] takes into account the effect

of inductance harmonics. In this thesis, the model will be used for predicting the current ripple that may arise if standard PI controllers are used for current control. The harmonics can also have a negative impact on the performance of speed and estimation algorithms (see Chapter 4).

Another source of torque ripple is known as *cogging torque*, which generated by the interaction of the rotor magnetic flux and the angular variation in the magnetic reluctance of the stator [33]. This torque component produces no stator excitation. Although algorithms have been presented that focus on minimizing the total torque ripple (including the cogging torque) [33], reduction of this ripple component is typically achieved using various design techniques.

2.1.6 Parameter Variations

The model parameters of the PMSM, particulary the resistance and inductance parameters, vary significantly with operating conditions. In [28], the phase resistance of the experimental PMSM, at room temperature, with the rotor unmounted, has been measured as a function of applied frequency. The increase in resistance, due to the skin effect, from zero to $\omega = 2$ pu, is approximately 170%.

A temperature rise also causes the resistance to increase. The temperature dependence of the stator resistance can typically be modeled as [43]

$$R_s = \frac{235 + T}{235 + T_0} R_{s,0} \tag{2.24}$$

where T is the winding temperature, and $R_{s,0}$ is the stator resistance at room temperature, $T_0 = 20^\circ$ C. During the design of the experimental PMSM, an upper limit on the stator-winding temperature has been set at 130° C [28, 45]. According to (2.24), the increase in resistance at the upper temperature limit, compared to room temperature, is then approximately 40%.

Saturation of the iron causes changes in the inductances L_d and L_q. This is especially pronounced in L_q, since the effective air gap of the q-axis is much smaller than for the d-axis, which is aligned to the rotor magnet; the effect of the saturation of L_d can often be neglected. This causes a decrease in L_q as a function of i_q due to saturation in the iron [62]. As will be discussed in Chapter 4, rotor-position estimation is particulary sensitive to uncertainties in L_q. Also, in order to maximize the torque-to-current ratio, the effect of the saturation of L_q must be taken into account. For the PMSM used in the experiments,[4] L_q has been measured using the

[4] See Appendix B for further details on parameters and rating.

techniques given in [6]. From these measurements, the variation of L_q as a function of i_q can, in the per-unit system, be approximated as

$$L_q(i_q) = \begin{cases} 0.86, & |i_q| < 0.37 \\ 0.86 - 0.35\,(|i_q| - 0.37) & 0.37 \leq |i_q| \leq 1. \end{cases} \tag{2.25}$$

2.1.7 Core Losses

Although resistive losses are included in the model described above, core losses are not. Modeling of core losses is complex since they arise owing to different phenomena, namely, eddy currents and hysteresis in the laminations [29]. These losses can be analyzed using finite element methods, but for control purposes it is common to identify the parameter R_c in parallel with v_d and v_q, as shown in Fig. 2.7, typically assuming only a nonlinear dependency of the frequency.

Neglecting the flux-linkage harmonics, the voltage equations can now be expressed as

$$v_d = R_s i_{d,o} + \frac{R_s + R_c}{R_c} L_d \frac{di_{d,o}}{dt} - \omega_r L_q \frac{R_s + R_c}{R_c} i_{q,o} \tag{2.26}$$

$$v_q = R_s i_{q,o} + \frac{R_s + R_c}{R_c} L_q \frac{di_{q,o}}{dt} + \omega_r L_d \frac{R_s + R_c}{R_c} i_{d,o} + \frac{R_s + R_c}{R_c} \omega_r \psi_m \tag{2.27}$$

$$i_d = \frac{v_d + R_c i_{d,o}}{R_s + R_c}, \qquad i_q = \frac{v_q + R_c i_{q,o}}{R_s + R_c}. \tag{2.28}$$

The impact of core (and resistive) losses and how it can be reduced by means of control is further investigated in Chapter 3.

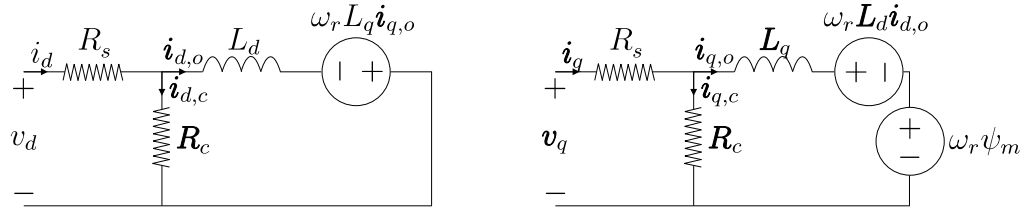

(a) d-axis. (b) q-axis.

Fig. 2.7 Equivalent circuit taking core losses into account.

2.2 Current Controller Design

A simple and efficient way to achieve fast and accurate current control in inverter-fed PMSMs is to utilize synchronous-frame PI controllers [38]. The mechanical

dynamics can be neglected as they are typically much slower than the current dynamics. Neglecting the impact of harmonics, the open-loop current dynamics, given by (2.17) and (2.18), can in operator form, i.e., $p \to d/dt$, be expressed as

$$\mathbf{i}_{dq}(p) = \mathbf{G}(p)(\mathbf{v}_{dq}(p) - \mathbf{E}). \tag{2.29}$$

Here, $\mathbf{G}(p)$ is the open-loop transfer function,

$$\mathbf{G}(p) = \begin{bmatrix} R_s + pL_d & -\omega_r L_q \\ \omega_r L_d & R_s + pL_q \end{bmatrix}^{-1} \tag{2.30}$$

and $\mathbf{E} = [0 \omega_r \psi_m]^T$ is the back EMF, that acts as a load disturbance. A block diagram of (2.29) is shown in Fig. 2.8. The current controller discussed here is a variant of

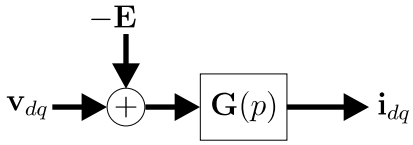

Fig. 2.8 Block diagram of the open-loop current dynamics. The back EMF acts as a load disturbance, that reduces the available "current-producing" voltage.

the controller proposed in [25], derived using the concept of internal model control (IMC) [60], and further modified for improved load-disturbance rejection capability in [27]. For salient PMSMs, it can be expressed as

$$v_d^{\text{ref}} = k_{p,d}(i_d^{\text{ref}} - i_d) + k_{i,d} \int (i_d^{\text{ref}} - i_d)dt - \omega_r \hat{L}_q i_q - R_{a,d} i_d \tag{2.31}$$

$$v_q^{\text{ref}} = k_{p,q}(i_q^{\text{ref}} - i_q) + k_{i,q} \int (i_q^{\text{ref}} - i_q)dt + \omega_r \hat{L}_d i_d - R_{a,q} i_q. \tag{2.32}$$

The first two terms on the right-hand sides of (2.31) and (2.32) represent standard PI controllers. As $\mathbf{G}(p)$ is non-diagonal, the current dynamics are coupled and the third terms are added for decoupling purposes. The last terms are called *active damping* [27] (named *active resistance* in [9]) and are added in order to improve the capability of load disturbance rejection (see below). In state-space form, the current control dynamics can be expressed as

$$\frac{di_d}{dt} = \frac{1}{L_d}\left(v_d - R_s i_d + \omega_r L_q i_q\right) \tag{2.33}$$

$$\frac{di_q}{dt} = \frac{1}{L_q}\left(v_q - R_s i_q - \omega_r L_d i_d - \omega_r \psi_m\right) \tag{2.34}$$

$$\frac{dI_d}{dt} = i_d^{\text{ref}} - i_d \tag{2.35}$$

$$\frac{dI_q}{dt} = i_q^{\text{ref}} - i_q \tag{2.36}$$

where (2.33) and (2.34) are the current dynamics and (2.35) and (2.36) represent the additional state variables due to the integrators. The output of the current controller forms two voltage reference commands. These are inputs to the pulse-width modulator, i.e., the actual voltages applied to the PMSM are given by $v_d = \mathrm{PWM}(v_d^{\mathrm{ref}})$ and $v_q = \mathrm{PWM}(v_q^{\mathrm{ref}})$ (see Appendix B for a description of the laboratory setup).

A block diagram of the closed-loop system is shown in Fig. 2.9, where the controller consists of the blocks inside the dashed region. The PI part of the controller is represented by $\mathbf{F}(p)$ and the decoupling and active damping, implemented as an inner feedback loop, are represented by the matrix $\mathbf{W}$. They can be expressed as

$$\mathbf{F}(p) = \begin{bmatrix} k_{p,d} + k_{i,d}/p & 0 \\ 0 & k_{p,q} + k_{i,q}/p \end{bmatrix}, \quad \mathbf{W} = \begin{bmatrix} -R_{a,d} & -\omega_r \hat{L}_q \\ \omega_r \hat{L}_d & -R_{a,q} \end{bmatrix}. \tag{2.37}$$

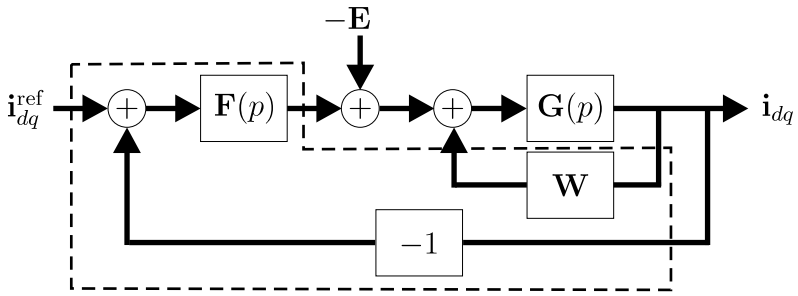

Fig. 2.9 Block diagram of the closed-loop current dynamics. The current controller given by (2.31) and (2.32) consists of the blocks inside the dashed region.

Design rules for the parameters of the PI controllers are proposed in [27]. The parameters should be chosen as

$$k_{p,d} = \alpha_c \hat{L}_d, \quad k_{i,d} = \alpha_c(\hat{R}_s + R_{a,d}) \tag{2.38}$$

$$k_{p,q} = \alpha_c \hat{L}_q, \quad k_{i,q} = \alpha_c(\hat{R}_s + R_{a,q}) \tag{2.39}$$

where α_c is the desired bandwidth of the closed-loop system and "hats" indicate model parameters. The block diagram in Fig. 2.9 can be simplified using standard block transformations. In matrix form, this simplifies the relation between the output and reference current to

$$\mathbf{i}_{dq} = -\underbrace{\left[\mathbf{I} + \mathbf{G}'(p)\mathbf{F}(p)\right]^{-1}\mathbf{G}'(p)}_{\mathbf{S}(p)}\mathbf{E} + \underbrace{\left[\mathbf{I} + \mathbf{G}'(p)\mathbf{F}(p)\right]^{-1}\mathbf{G}'(p)\mathbf{F}(p)}_{\mathbf{G}_{\mathrm{cl}}(p)}\mathbf{i}^{\mathrm{ref}} \tag{2.40}$$

where $\mathbf{G}'(p) = \left[\mathbf{I} - \mathbf{G}(p)\mathbf{W}\right]^{-1}\mathbf{G}(p)$ is introduced for simplicity. $\mathbf{S}(p)$ represents the *sensitivity function*, relating the output current to the load disturbance. With the

recommended selection of the controller parameters and assuming no parameter errors, the closed-loop dynamics, $\mathbf{G}_{\mathrm{cl}}(p)$, and the sensitivity function become

$$\mathbf{G}_{\mathrm{cl}}(p) = \begin{bmatrix} \dfrac{\alpha_c}{p+\alpha_c} & 0 \\ 0 & \dfrac{\alpha_c}{p+\alpha_c} \end{bmatrix} \tag{2.41}$$

$$\mathbf{S}(p) = \begin{bmatrix} \dfrac{p}{(p+\alpha_c)(pL_d + R_s + R_{a,d})} & 0 \\ 0 & \dfrac{p}{(p+\alpha_c)(pL_q + R_s + R_{a,q})} \end{bmatrix}. \tag{2.42}$$

As can be seen in (2.41), the closed-loop dynamics consist of two, decoupled, first-order systems. As is well known, the rise time, t_{r}, of a first-order system is related to the bandwidth, α, as $t_{\mathrm{r}} = \ln 9/\alpha$. Hence, the controller is parameterized in motor parameters and the desired bandwidth. This is attractive since it simplifies the implementation considerably as the tuning procedure of the controller is removed.

The sensitivity function, $\mathbf{S}(p)$, has a zero at the origin. Hence, stepwise (and quasi-constant) disturbances will be fully rejected when a steady-state condition is reached. As the load disturbance, $\mathbf{E}$, ideally acts only in the q-direction, the properties of $\mathbf{S}_{(2,2)}(p)$ are particulary important. Without the active damping, i.e., $R_{a,q}=0$, the two poles are located at $p = -\alpha_c$ and $p = -R_s/L_q$, respectively. Typically, $R_s/L_q \ll \alpha_c$ so the load-rejection dynamics are considerably slower than the closed-loop current dynamics. In order to improve the load rejection capability, the active damping should be chosen as [27]

$$R_{a,d} = \alpha_c \hat{L}_d - \hat{R}_s, \quad R_{a,q} = \alpha_c \hat{L}_q - \hat{R}_s. \tag{2.43}$$

With this choice and assuming no parameter errors, $\mathbf{S}(p)$ is simplified to

$$\mathbf{S}(p) = \mathrm{diag}\left(\frac{p}{L_d(p+\alpha_c)^2}, \frac{p}{L_q(p+\alpha_c)^2} \right). \tag{2.44}$$

Hence, the load-rejection dynamics become as fast as the closed-loop dynamics. A Bode diagram of the gains $|\mathbf{S}_{(1,1)}(j\omega)|$, $|\mathbf{S}_{(2,2)}(j\omega)|$ and $|\mathbf{G}_{\mathrm{cl}(1,1)}(j\omega)| = |\mathbf{G}_{\mathrm{cl}(2,2)}(j\omega)|$ is shown in Fig. 2.10 for $\alpha_c = 1$ pu. This is a typical value used in the simulations and experiments (it corresponds to a desired current rise time of 1.7 ms).

Impact of Parameter Variations

As mentioned in Section 2.1.6, parameter variations are most pronounced in R_s (due to temperature and frequency variations) and L_q (due to saturation). Both of these phenomena can be taken into account. However, this makes the current controller

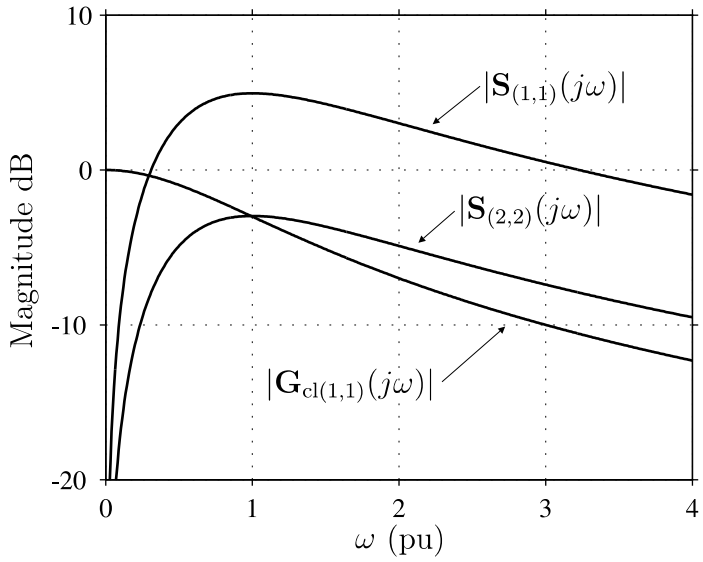

Fig. 2.10 Bode diagram of the closed-loop dynamics and sensitivity functions for $\alpha_c = 1$ pu.

considerably more complex as the six controller parameters ($k_{p,d}$, $k_{p,q}$, $k_{i,d}$, k_{i_q}, $R_{a,d}$ and $R_{a,q}$) then must be updated at each sample step.

The impact of parameter variations can be studied by computing $\mathbf{G}_{\mathrm{cl}}(p)$ assuming $\tilde{L}_q \neq 0$ and $\tilde{R}_s \neq 0$. The variation in L_d is neglected as the variation of this parameter, as mentioned previously, is typically small. Assuming $|\tilde{R}_s| \ll 2\alpha_c L_d$ and $|\tilde{R}_s| \ll 2\alpha_c(L_q - \tilde{L}_q)$ results in

$$\mathbf{G}_{\mathrm{cl}}(p) \approx \begin{bmatrix} \dfrac{\alpha_c}{p+\alpha_c} & \dfrac{\alpha_c p(L_q - \tilde{L}_q)\tilde{L}_q\omega_r}{L_d(p+\alpha_c)(p^2 L_q + 2p\alpha_c(L_q - \tilde{L}_q) + \alpha_c^2(L_q - \tilde{L}_q))} \\ 0 & \dfrac{\alpha_c(L_q - \tilde{L}_q)(p+\alpha_c)}{p^2 L_q + 2p\alpha_c(L_q - \tilde{L}_q) + \alpha_c^2(L_q - \tilde{L}_q)} \end{bmatrix}. \tag{2.45}$$

Hence, no strong dependence on $\tilde{R}_s$ can be expected. However, $\mathbf{G}_{\mathrm{cl}}(p)$ is upper triangular, indicating that small disturbances in i_d can arise along with large steps in i_q. Performing a Taylor series expansion around $\tilde{L}_q = 0$ for each element, $\mathbf{G}_{\mathrm{cl}}(p)$ can be further simplified to

$$\mathbf{G}_{\mathrm{cl}}(p) \approx \frac{\alpha_c}{p+\alpha_c} \begin{bmatrix} 1 & \dfrac{\tilde{L}_q\omega_r p}{L_d(p+\alpha_c)^2} \\ 0 & 1 - \dfrac{\tilde{L}_q p^2}{L_q(p+\alpha_c)^2}. \end{bmatrix} \tag{2.46}$$

Whether or not the effect of saturation of L_q should be taken into account when implementing the current controller depends on the specifications of both motor and

desired performance of the closed-loop current control. The effect of saturation has not been taken into account in any of the current controllers used in the simulations or experimental results presented in this thesis.

Anti-Windup and Overmodulation

Due to limited dc-link voltage, the output of the current controller, i.e., the voltage reference commands to the inverter, must be limited. However, this causes the integral part of the PI controller to accumulate the control error. This results typically in large overshoots because the integral part of the controller will still be high even when the control error becomes small. The phenomenon is known as integrator windup. Several different methods to avoid windup have been proposed in the literature and examples developed for electrical drives are found in [10, 27, 77].

The *back-calculation* method [27] (also known as *realizable references* [10]) is given by

$$u = k_p e + k_i I \tag{2.47}$$

$$\overline{u} = [u]_{\min}^{\max} \tag{2.48}$$

$$\frac{dI}{dt} = e + \frac{1}{k_p}\left(\overline{u} - u\right). \tag{2.49}$$

Here, e is the control error and I is the integral state variable. As can be seen, the integrator part of the controller is updated not with the control error, but with a modified error that would have given $u = \overline{u}$, effectively avoiding integrator windup. Note that when $u = \overline{u}$, the integrator is updated with the control error e, i.e., when not in saturation, the controller acts as a standard PI controller.

The output voltage vector of a PWM inverter must be within the well known *voltage hexagon*, drawn using the stationary $\alpha\beta$-coordinate system [42] and shown in Fig. 2.11. Linear modulation is possible up to the radius of the maximum circle that can be fitted within the hexagon. In order to enhance the transient response of the current loop, operation outside this circle can be utilized. Some overmodulation strategy must then be used. A review of different overmodulation strategies for three-phase PWM inverters can be found in [66].

2.2.1 Experimental Evaluation

In order to demonstrate the impact of harmonics of the performance of the current controller discussed above, a simulation and results from an experiment of a step response is presented here. The parameters of the PMSM correspond to the PMSM

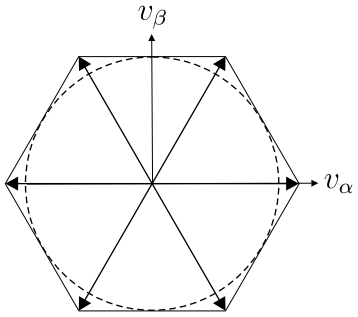

Fig. 2.11 Voltage hexagon. The six realizable voltage vectors (excluding the two zero vectors) are shown. Linear modulation is possible within the circle.

used in the experiments and can be found in Appendix B. As perfect knowledge of the motor parameters is not to be expected, the parameter errors $\tilde{L}_q = -0.2L_q$, $\tilde{L}_d = 0.2L_d$, $\tilde{R}_s = 0.5R_s$ are introduced. Note that $\tilde{L}_q < 0$ to take into account the effect of saturation and $\tilde{R}_s > 0$, assuming that the true stator resistance is higher than its estimated (measured) value.

The impact of harmonics in both flux linkage and inductance are taken into account. The flux-linkage harmonics are, as mentioned previously, simply identified using measurements of the open-circuit voltage. The inductance harmonic, L_6, is assumed to be $L_6 = 0.4L_d$. As mentioned in Section 2.1.4, it can be expected that current harmonics will arise in i_d along with large i_q due to the coupling of harmonics caused by L_6.

The bandwidth of the current controller is set to $\alpha_c = 1.17$ pu, which corresponds to a desired rise time of 1.5 ms. The rotor speed is assumed to be constant, $\omega_r = 0.25$ pu. The dominant flux-linkage harmonic is $\psi_{q,6}$ and its impact can be investigated by computing the gain of the sensitivity function at $\omega = 6\omega_r$, which is $|\mathbf{S}_{(2,2)}(j\omega)|_{\omega=6\omega_r} \approx 0.61$. Thus, a small current ripple in i_q with an amplitude of $0.61 \cdot \omega_r \psi_{q,6} \approx 5 \cdot 10^{-3}$ pu due to the flux-linkage harmonic $\psi_{q,6}$ can be expected. At $t = 0.1$ s the current references are set to $i_q^{\text{ref}} = 0.8$ pu and $i_d^{\text{ref}} = -0.25$ pu, where i_d^{ref} is set according to the max torque-per-ampere trajectory (see Chapter 3).

Simulation and experimental results are shown in Fig. 2.12. For $t < 0.1$ s, the simulation shows a current ripple in i_d and i_q (due to the flux-linkage harmonics) that is less than 610^{-3} pu (not visible in the figure). The corresponding measurement result shows a current ripple that is less than $1 \cdot 10^{-3}$ pu. At $t = 0.1$ s, a current step is introduced and the measured rise time of i_d and i_q, both in the simulation and the results obtained from the experiment, is approximately 1.5 ms, as predicted by theory. The coupling between i_d and i_q, due to the inductance harmonics, is also clearly visible. Due to the large amplitude of i_q, ripple arises in i_d when $t \geq 0.1$ s.

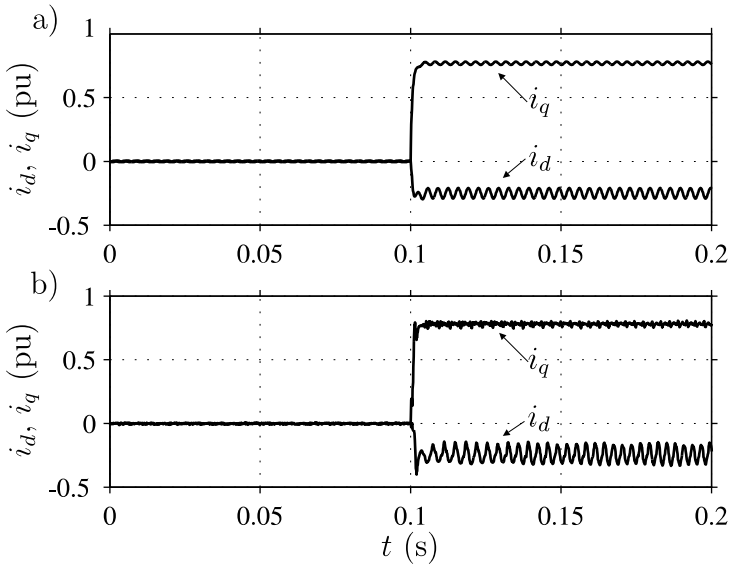

Fig. 2.12 Current step at $t = 0.1$ s. The desired closed-loop bandwidth $\alpha_c = 1.17$ pu and rotor speed $\omega_r = 0.25$ pu. a) Simulation. b) Experimental result.

2.3 Operation in the Field-Weakening Region

For operation above base speed, the back EMF, due to the permanent magnets on the rotor, can exceed the available inverter voltage. For induction machines, the flux-producing component is therefore reduced to lower the back EMF and enable operation above base speed, at the cost of reduced output torque. For PMSM drives, the impact of the back EMF can be reduced by adding a demagnetizing current component, i.e., $i_d < 0$. This allows for operation above base speed, although the obtainable torque, also in this case, is reduced due to the demagnetizing current component [32, 63].

The properties of operation above base speed, i.e., *field-weakening operation*, is commonly described in terms of limitations in the current dq-plane. The current is limited by

$$\sqrt{i_d^2 + i_q^2} \leq I_{\max} \tag{2.50}$$

where $I_{\max}$ is the limit set by either the inverter rating or thermal constraints of the PMSM. Similarly, the available inverter voltage is limited by

$$\sqrt{v_d^2 + v_q^2} \leq V_{\max} \tag{2.51}$$

where $V_{\max}$ is the maximum available inverter voltage. Keeping the inverter voltage vector inside the largest circle possible within the voltage hexagon (see Fig. 2.11),

$V_{\max}$ is related to the available dc-link voltage as $V_{\max} = V_{\mathrm{dc}}/\sqrt{3}$, where V_{dc} is the dc-link voltage [66]. In vehicle applications, where the dc-link voltage is expected to change, this voltage is typically monitored.

The way (2.51) sets a limit on the available currents is easily found by substituting the expressions for v_d and v_q, by using (2.17) and (2.18), in (2.51). Neglecting the current derivatives, the following condition is obtained

$$V_{\max}^2 = (R_s i_d - \omega_r L_q i_q)^2 + (R_s i_q + \omega_r L_d i_d + \omega_r \psi_m)^2 . \tag{2.52}$$

As the resistive voltage drop is relatively small, it can be neglected and (2.52) can be simplified to [32]

$$\left(i_d + \frac{\psi_m}{L_d}\right)^2 + \left(\frac{L_q}{L_d} i_q\right)^2 = \left(\frac{V_{\max}}{\omega_r L_d}\right)^2 \tag{2.53}$$

which describes an ellipse (or a circle in the case of a non-salient PMSM) in the dq-plane, with its center at $i_d = -\psi_m/L_d$ and ellipticity L_q/L_d. Thus, the current is not only limited within the circle $\sqrt{i_d^2 + i_q^2} \leq I_{\max}$, but also within this *voltage-limit ellipse*. As the speed increases, the voltage-limit ellipse shrinks towards its center. The voltage-limit ellipse is shown in Fig. 2.13 at three different rotor speeds: $\omega_r = 1$, 1.2 and 1.5 pu. As also shown in Fig. 2.13, two additional phenomena affect the shape of the voltage-limit ellipse. The impact of the stator resistance causes it to slightly rotate anti-clockwise, and the saturation of L_q causes it to increase in the vertical direction [87]. Due to additional voltage drops because of harmonics, inductive voltage drops due to current derivatives, voltage drops in the inverter, etc., the outermost region embraced by the voltage-limit ellipse is not obtainable in practice.

2.3.1 Review of Field-Weakening Strategies

The vector-control schemes for operation in the field-weakening region can be divided into two categories. In the first category, the solutions are based on different types of flow charts, examples are [49, 62, 83]. Here, different current reference trajectories, expressed using motor parameters or derived from experiments, are used depending on if the rotor speed is under or above base speed. Above base speed, i_d is typically limited by

$$i_d \leq -\frac{\psi_m}{L_d} + \frac{1}{L_d}\sqrt{\frac{V_{\max}^2}{\omega_r^2} - L_q^2 i_q^2} \tag{2.54}$$

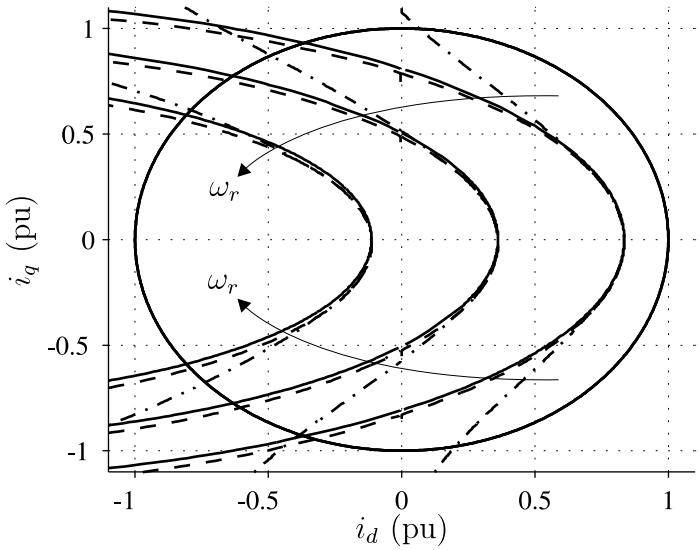

Fig. 2.13 Available operation region, expressed in the currents dq-plane, for the three rotor speeds $\omega_r = 1$, 1.2 and 1.5 pu. Solid lines indicate the voltage-limit ellipse equation given by (2.53). Dashed lines include the resistive voltage drop and dashed-dotted lines also take into account the impact of the saturation of L_q. The current-limit circle is also shown.

which is found by solving for i_d in (2.53).

Solutions which utilize (2.54), or variants thereof, must take several additional limitations into account. The strong dependence on motor parameters is a drawback, since both $V_{\max}$, L_q, and, for some machines, also L_d, may change significantly at different operating points. These effects have to be taken into account in order to assure that the voltage really is limited. Another drawback is the utilization of the computationally costly square root; important in drives where the DSP, typically owing to cost, is very simple. Further, since the impact of resistive voltage drops are neglected in (2.54), they also have to be taken into account with some method [76]. The selection when to switch over from the normal control strategy to the field-weakening control strategy is also not trivial. The reason for this is that the base speed, which typically defines when to switch between normal and field-weakening strategies, is dependent on the available dc-link voltage. If the dc-link voltage is changed, the base speed must be recomputed, which further complicates the control strategy.

Although all these limitations can be taken into account, it is the opinion of the author that field-weakening strategies which utilize (2.54), or variants thereof, due to their complexity, are less suited for applications where the dc-link voltage can be expected to change depending on the quality of the dc source. In practice, this

includes most applications.

The second category of vector-control schemes that allow for operation in the field-weakening region is based on closed-loop voltage control, which generates current references that keep the voltage magnitude within the limit set by the inverter. This technique can be applied to drives that use both permanent-magnet as well as induction motors and will be considered in the rest of this section.

An early reference that utilizes this technique for PMSM drives is [41], which proposes an additional PI controller to control the value of i_d^{ref} in order to reduce the voltage magnitude.[5] The input of this PI controller is $V_{\max}-\sqrt{(v_d^{\mathrm{ref}})^2+(v_q^{\mathrm{ref}})^2}$, where v_d^{ref} and v_q^{ref} are the output voltage references from the current controller. A simplification is given in [53], where the algorithm is modified by letting the input of the PI controller be $V_{\max}^2-(v_d^{\mathrm{ref}})^2-(v_q^{\mathrm{ref}})^2$. The algorithm is simplified by the removal of the square root. The method is further developed in [27], although this reference considers induction motors. Here, the PI controller is replaced with pure integration and a design rule for the selection of the integrator gain is derived. The latter is important in order to achieve proper operation when torque or speed changes rapidly. This is also highlighted in [7] and [54], where the former also presents a selection rule for the integrator gain.

2.3.2 Closed-Loop Field-Weakening Control

The field-weakening controller which is used in the experiments is essentially a variant of the controller presented in [41], with the modifications given in [27]. Pure integration is utilized on i_d^{ref} in order to keep the voltage within the limit set by the inverter, i.e.,

$$\frac{di_d^{\mathrm{ref}}}{dt}=\gamma\left((V'_{\max})^2-(v_d^{\mathrm{ref}})^2-(v_q^{\mathrm{ref}})^2\right). \tag{2.55}$$

Here, γ is a positive gain that affects the dynamics of the field-weakening controller. Of course, the selection of γ will also affect the overall system dynamics of the drive. The voltage $V'_{\max}$ is the upper voltage limit allowed. As mentioned, due to additional voltage drops because of harmonics, inductive voltage drops due to current derivatives, voltage drops in the inverter, etc., $V'_{\max}$ must be set lower than the maximum available inverter voltage, $V_{\max}$.

The current in the d-direction must not be smaller than $-I_{\max}$ in order to avoid permanent demagnetization of the rotor magnets. Furthermore, when $(V'_{\max})^2>$

[5] In [87], a similar algorithm is proposed where not i_d^{ref} is controlled, but rather the angle of the current vector to the d-axis.

$(v_d^{\mathrm{ref}})^2+(v_q^{\mathrm{ref}})^2$, (2.55) will force i_d^{ref} to increase, so i_d^{ref} must therefore also be limited by the max-torque-per-ampere curve, $i_{d,\max(T/i)}$ (see Chapter 3). Hence, i_d^{ref} is limited by

$$-I_{\max} \leq i_d^{\mathrm{ref}} \leq i_{d,\max(T/i)} \tag{2.56}$$

Inside the current-limit circle, no limit is put on i_q^{ref} and this mode of operation is in this thesis designated *Mode A*. When operating in *Mode A*, the algorithm will then reduce i_d^{ref} so that, in the steady state, $(V'_{\max})^2=(v_d^{\mathrm{ref}})^2+(v_q^{\mathrm{ref}})^2$.

If i_d^{ref} is reduced so much that the current-limit circle is reached, *Mode B*, the static constraint

$$i_q^{\mathrm{ref}} = \sqrt{I_{\max}^2 - (i_d^{\mathrm{ref}})^2} \tag{2.57}$$

is put on i_q^{ref}. This will force the current vector to remain within the current-limit circle. The two modes of operation are shown in Fig. 2.14.

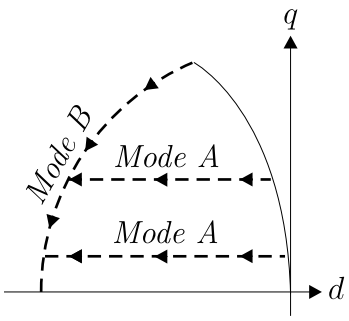

Fig. 2.14 Different modes of operation for the field-weakening controller. Operation in *Mode B* and two examples of *Mode A* operation are shown. For increasing speed (back EMF), the controller will move the current references in the direction indicated by the arrows.

2.3.3 Gain Selection for the Field-Weakening Controller

As mentioned above, the selection of the integration gain, γ, will not only affect the dynamics of the field-weakening controller, but will also have impact on the current dynamics. The reason for this is due to the fact that the output of the field-weakening controller consists of current references, which are inputs to the current controller. Therefore, current- and field-weakening dynamics are coupled, and this factor should be taken into account when selecting γ. This was done in [27], which studied the closed-loop dynamics of the current- and field-weakening controller, although the reference considered induction motors.

Essentially following [27], but considering salient PMSMs, a design rule for the selection of γ will be presented here. The characteristic polynomial is found by collecting i_d, i_q, I_d, I_q, and i_d^{ref} into a state vector. The dynamics are given by the linear expressions (2.33)–(2.36) and the nonlinear (2.55). Note that the mechanical dynamics are neglected, i.e., ω_r is considered as a slowly varying parameter. This assumption is valid if the dynamics of both the current- and field-weakening controller are much faster than the mechanical dynamics. With the selection of γ presented below, this assumption will always be valid. Now, assuming no parameter errors and neglecting the resistive voltage drops, $v_d = v_d^{\text{ref}}$, $v_q = v_q^{\text{ref}}$, where v_d^{ref} and v_q^{ref} are the output voltage references from the current controller, given by (2.31) and (2.32), are substituted in (2.33)–(2.36). Eqs. (2.33)–(2.36) and (2.55) now form a nonlinear state-space system, $\dot{\mathbf{x}} = \mathbf{f}(\mathbf{x}, \mathbf{u})$, which can be linearized around some operating point as $\dot{\mathbf{x}} = \mathbf{A}\mathbf{x}+\text{input}$. The linearized dynamics are governed by the characteristic polynomial, $c(p)$, which is given by $c(p) = \det(p\mathbf{I} - \mathbf{A})$.

Mode A, Small Torques

For *Mode A*, the characteristic polynomial, for some current i_q^{ref}, is found as

$$\begin{aligned} c(p) = (p+\alpha_c)^3 [p^2 + 2\alpha_c\gamma|\omega_r|L_d\sqrt{(V'_{\max})^2 - (\omega_r L_q i_q^{\text{ref}})^2} \\ + \alpha_c p(1 - 2\gamma\omega_r L_d L_q i_q^{\text{ref}})]. \end{aligned} \tag{2.58}$$

For small torques, i_q^{ref} can be neglected, which yields

$$c(p) = (p+\alpha_c)^3 \left(p^2 + \alpha_c \left(p + 2\gamma|\omega_r|L_d V'_{\max}\right)\right). \tag{2.59}$$

With the selection of γ as

$$\gamma = \frac{\alpha_{\text{fw}}}{2\omega_{\text{fw}}\hat{L}_d V'_{\max}}, \quad \omega_{\text{fw}} = \begin{cases} \omega_{\text{base}}, & |\omega_r| \leq \omega_{\text{base}} \\ |\omega_r| & |\omega_r| > \omega_{\text{base}} \end{cases} \tag{2.60}$$

and assuming $\alpha_{\text{fw}} \ll \alpha_c$ and $\omega_{\text{fw}} = |\omega_r|$, (2.59) can be simplified to

$$c(p) = (p+\alpha_c)^4 (p+\alpha_{\text{fw}}). \tag{2.61}$$

Hence, with the selection of γ given by (2.60), the dynamics of the field-weakening controller, operating in *Mode A* and assuming small torques, is governed by the pole located at $p = -\alpha_{\text{fw}}$.

Mode A, Large Torques

For large torques, the impact of i_q^{ref} cannot be neglected in (2.58). The square-root expression in (2.58) can then be approximated as $\sqrt{(V'_{\max})^2 - (\omega_r L_q i_q^{\text{ref}})^2} \approx x V'_{\max}$, where $0 < x \leq 1$. The characteristic polynomial is then simplified to

$$\begin{aligned} c(p) &= (p+\alpha_c)^3 \left(p^2 + \alpha_c \alpha_{\text{fw}} x + \alpha_c p \left(1 - \frac{\alpha_{\text{fw}} L_q \text{sign}(\omega_r)}{V'_{\max}} i_q^{\text{ref}} \right) \right) \\ &\approx (p+\alpha_c)^4 (p+\alpha_{\text{fw}} x) \end{aligned} \tag{2.62}$$

where the approximation is valid assuming $|(\alpha_{\text{fw}} L_q \text{sign}(\omega_r) i_q^{\text{ref}})/(V'_{\max})| \ll 1$, $\omega_{\text{fw}} = |\omega_r|$, and $\alpha_{\text{fw}} \ll \alpha_c$. Considering a worst-case scenario, where, $V'_{\max} = 0.9 V_{\max}$, $\omega_r = \omega_{\text{base}}$ and $i_q^{\text{ref}} = I_{\max}$, this gives $x \approx 0.7$ (assuming the motor parameters given in Appendix B). Thus, the field-weakening dynamics will be somewhat, although not significantly, slower compared to *Mode A* operation with small torque.

Mode B

Operation in *Mode B* adds the additional static constraint, due to the current-limit circle, on i_q^{ref}, given by (2.57). As in [27], (2.57) is first linearized around some operating point $\{i_{d,0}, i_{q,0}\}$:

$$i_q^{\text{ref}} = i_{q,0} + \xi \left(i_d^{\text{ref}} - i_{d,0} \right) \tag{2.63}$$

where $\xi = -i_{d,0}/i_{q,0}$. Replacing i_q^{ref} with this expression, the characteristic polynomial is found as

$$\begin{aligned} c(p) = (p+\alpha_c)^3 \Big\{ p^2 + \alpha_c \big[& p(1 + 2\gamma L_q \omega_r \psi_m \xi) \\ & + 2\gamma |\omega_r| \sqrt{L_d^2 (V'_{\max})^2 + \xi^2 L_q^2 [(V'_{\max})^2 - (\omega_r \psi_m)^2]} \big] \Big\}. \end{aligned} \tag{2.64}$$

Now, the assumptions $V'_{\max} \approx \omega_r \psi_m$ and $|2\gamma L_q \omega_r \psi_m \xi| \ll 1$, are made. These assumptions are valid if the operation points when $i_q^{\text{ref}} \approx 0$ are neglected. This is reasonable since operating in *Mode B* with $i_q^{\text{ref}} \approx 0$ corresponds to a theoretical maximum speed when no further field weakening can be applied to reduce the impact of the back EMF. With these approximations, also in this mode, choosing γ as (2.60), $c(p)$ is found as

$$c(p) = (p+\alpha_c)^4 (p+\alpha_{\text{fw}}). \tag{2.65}$$

Selection of α_{fw}

As shown above, the dynamics of the field-weakening controller are governed by a single pole at $p=-\alpha_{\text{fw}}$ in both modes of operation. In order to avoid voltage saturation during accelerations, the dynamics of the field-weakening controller should be faster than the mechanical dynamics. For applications where closed-loop speed control is used, choosing $\alpha_{\text{fw}} = 10\alpha_s$, where α_s is the bandwidth of the speed control loop, is a reasonable design rule, provided that $\alpha_{\text{fw}} \ll \alpha_c$ still holds.

However, for vehicle applications, where the drive is typically torque controlled, this is not applicable. Instead, a reasonable recommendation is to choose the field-weakening dynamics at least a decade faster than the mechanical time constant, i.e., $\alpha_{\text{fw}} \geq 10\hat{b}/\hat{J}$, where b is the viscous damping constant.

2.3.4 Simulation and Experimental Evaluation

Simulation

The field-weakening controller presented above is verified through a simulation shown in Fig. 2.15, in which closed-loop speed control (designed following the rules presented in [27]) is utilized. The current controller, motor parameters, and parameter errors are the same as for the simulation in Section 2.2.1. The bandwidth of the speed control loop, α_s, is chosen $\alpha_s = \alpha_c/100$ and accordingly, $\alpha_{\text{fw}} = 10\alpha_s = \alpha_c/10$. The moment of inertia of the shaft is assumed to $J = 200$ pu, which can be considered small and allows for rapid accelerations.

Initially, the PMSM is loaded with a load torque of $T_L = 0.75$ pu, which is removed at $t = 0.6$ s. At $t = 0.1$ s, the speed reference is set to $\omega_r^{\text{ref}} = 2$ pu, which activates the field-weakening controller approximately at $t = 0.15$ s. Clearly, appropriate field weakening is achieved as the amplitude of the voltage vector $\sqrt{v_d^2 + v_q^2}$ never reaches 1 pu (V'_{max} is set to 0.9 pu). As can be expected, current ripple arises both in current and voltages due to the harmonics in both flux linkage and inductance.

Experimental Results

Fig. 2.16 shows an experimental result where the PMSM operates at $\omega_r = 1$ pu and the measured electro-mechanical torque is 0.9 pu, (corresponding to approx. 70 Nm). The closed-loop bandwidth of the current controller is set at $\alpha_c = 1$ pu, $\alpha_{\text{fw}} = \alpha_c/200$ and $V'_{\text{max}} = 0.85$ pu. Due to the field-weakening controller, i_d^{ref} is reduced from $i_d^{\text{ref}} = -0.27$ pu down to $i_d^{\text{ref}} = -0.45$ pu to reduce the impact of

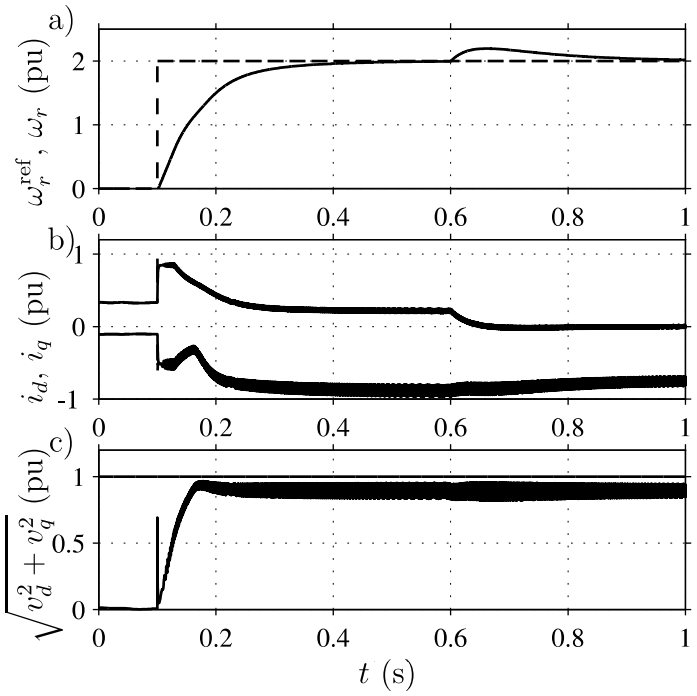

Fig. 2.15 Simulation of a closed-loop speed controlled PMSM including field-weakening control. At $t = 0.1$ s, the speed step $\omega_r^{\text{ref}} = 2$ pu is applied.

the back EMF. As can be seen, the current and field-weakening controllers work properly and the harmonic content in i_a is low (compare with Figs. 23 and 24, p. 150 in [45]).

Fig. 2.17 shows an experimental result that demonstrates dynamics of the field-weakening controller. The rotor speed, shown in Fig. 2.17a), is initially set (controlled by the loading dc machine) at $\omega_r \approx 0.5$ pu. The PMSM is current controlled with $i_q^{\text{ref}} = 0.36$ pu and i_d^{ref} is set corresponding to the max torque-per-ampere trajectory. At $t \approx 1$ s, the rotor speed is ramped up to $\omega_r \approx 0.7$ pu. To allow for field-weakening operation below base speed, V'_{max} is reduced to $V'_{\text{max}} = 0.3$ pu. As the dynamics of the field-weakening controller are evaluated, this is done in order to avoid reaching very high speeds during the experiment. As can be seen, the field-weakening controller is activated and i_d is reduced down to $i_d \approx -0.7$ pu in order to avoid voltage saturation.

The experimental results in Fig. 2.17 have been obtained using the speed and position estimator discussed in Chapter 4. Hence, the rotor speed and position used in the control algorithms are not measured, but rather estimated. The gain of the estimator (see Chapter 4) is chosen as $\rho = \alpha_c/20$. Fig. 2.17c) shows the angular estimation error, $\tilde{\theta} = \theta - \hat{\theta}$, where $\hat{\theta}$ is the estimated rotor position. As can be seen,

the angular estimation error is minor, less than 5°. Although not shown, the speed estimation error, $\tilde{\omega}_r = \omega_r - \hat{\omega}_r$ is very small, $|\tilde{\omega}_r| \leq 0.005$ pu. Similar results have been obtained whether the speed and position estimator is used or not.

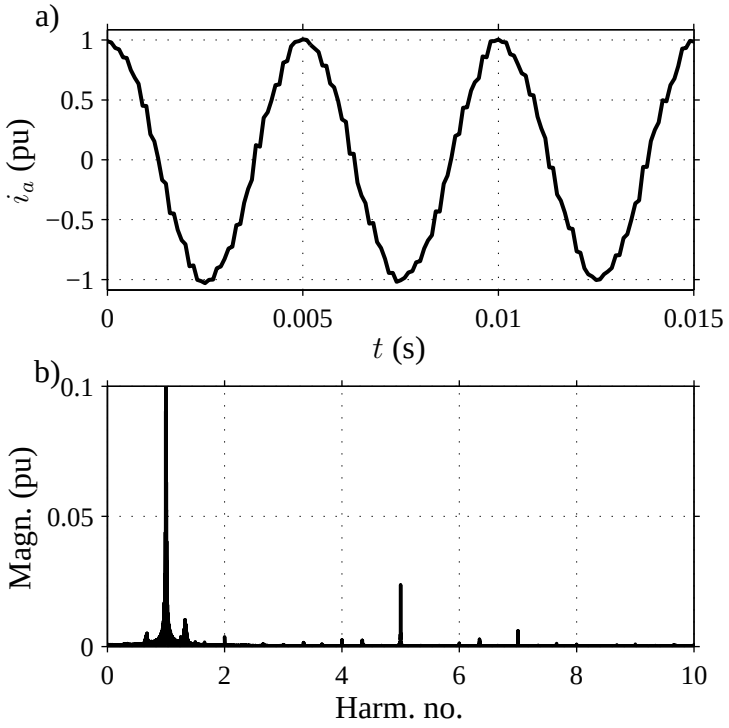

Fig. 2.16 Steady-state operation at $\omega_r = 1$ pu, $T_e \approx 0.9$ pu. a) i_a, b) Harmonic content of i_a. Note that the amplitude of the fundamental of i_a is approx. 0.97 pu.

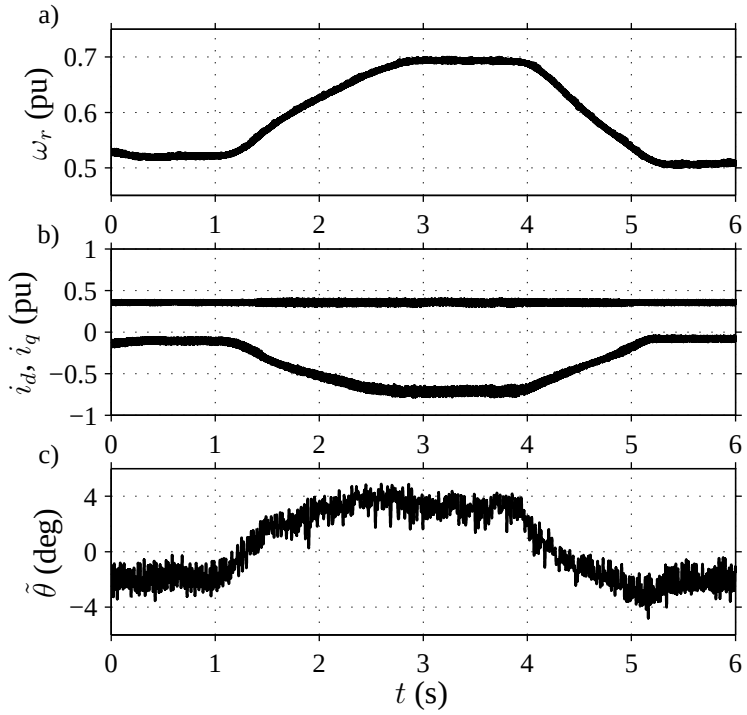

Fig. 2.17 Experimental results that demonstrates the dynamics of the field-weakening controller. The speed and position estimator discussed in Chapter 4 has been utilized. a) ω_r, b) i_d and i_q, c) position estimation error.

2.4 Summary of Chapter

This chapter has dealt with modeling and control of vector-controlled PMSMs which are equipped with a rotor position sensor. A transient model that takes harmonics into account was reviewed, and its impact on current harmonics was verified, both with simulations and through experimental results. Furthermore, control algorithms for operation in the field-weakening region were reviewed. The field-weakening controller, presented in [41] and further developed in [27], was chosen for implementation. The selection rule of the integral gain of the field-weakening controller presented in [27] (considering induction motors) was verified with a similar analysis but considering salient PMSMs.

Chapter 3

Loss-Minimization Control of PMSM Drives

This chapter considers minimization, by means of control, of losses in PMSM drives (motor+inverter). Resistive, core and inverter losses are considered. First, the theory of achieving operation with minimized losses is reviewed. A case study is then presented to investigate the impact of loss minimization, by means of control, for the experimental PMSM developed in [28, 45].

3.1 Introduction and Outline of Chapter

In an HEV application, the PMSM must operate at varying loads and speeds, which requires careful selection of motor parameters for the machine designer, in order to minimize losses [23]. However, electrical losses in the PMSM can also be affected by control action. The problem resolves into selecting i_d and i_q for each operating point (torque and speed) so that losses are minimized [17, 37, 51, 64, 85, 86]. As losses are minimized in the PMSM, this will also minimize the current from the dc source (if inverter losses are neglected). In this thesis, the term *loss-minimization control* is used for algorithms that control the PMSM (or PMSM+inverter) so that losses are minimized. Efficiency improvement by keeping the power factor equal to unity is presented in [48], but, although the real-to-apparent power is maximized, the power losses are not minimized.

In an HEV application, operation with minimized losses is important, since high efficiency is vital to reduce the fuel consumption of the vehicle. This is very attractive since it also results in improved fuel economy and increased operating range; two very important factors for a potential vehicle customer. Ideally, since no extra

hardware is added, energy is saved with no additional drawbacks. The main purpose of this chapter is to investigate how losses can be reduced through control action and see what impact it can have on a PMSM drive system (used for propulsion) in an HEV application.

The methods for achieving loss-minimization control in PMSM drives can be divided into two categories. In the first category, the input power to the drive is measured and some type of search controller is implemented where i_d is changed in order to reach minimum input power [17, 85, 86]. The advantage of these techniques is the independence of motor parameters, but finding the operating point with minimized losses by using a search controller is difficult in a vehicle application, since the shape of the loss minimum at a given operating point (torque and speed) and as a function of i_d is flat [51]. This forces the search controller to search using small steps, and therefore the dynamics will be slow [5]. Typically, a speed controller is also added to guarantee that the operating point (torque and speed) does not change during the operation of the search controller. This makes the use of these techniques somewhat limited in vehicle applications, where the drives are typically torque controlled and the operating point changes continuously.

The second category identifies the motor parameters through some measurement procedure and the loss minimization condition, i.e., the i_d that minimizes losses at a given speed and i_q, is computed and implemented in the controller program [37, 51, 64]. Typically, the loss minimization conditions obtained are verified, and adjusted, so that losses really are minimized. Since this approach is suitable for torque-controlled drives and since motor parameters can be assumed to be well known in a vehicle application, this approach is adopted in this chapter.

This chapter is organized as follows. First, the theory of achieving operation with minimized losses is presented. In order to investigate the impact of using loss-minimization control on the PMSM drive developed in [28, 45], a case study based on simulations, where also inverter losses are considered, is then presented.

3.2 Loss Expressions

The losses in the PMSM can be separated into two parts, mechanical and electrical. Mechanical losses arise due to air friction and friction in bearings. These losses are, by nature, strongly dependent on rotor speed and cannot be affected through control action. Hence, the input power, P_{in}, can be separated into

$$P_{\text{in}} = P_{T_e} + P_{\text{loss,PMSM}} + P_{\text{fric}} \tag{3.1}$$

where P_{T_e} is the part of the input power producing torque, $P_{\text{loss,PMSM}}$ are the electrical losses and P_{fric} are the friction losses. The electrical losses consist of resistive losses, P_{res}, and core losses, P_{co}. Hence,

$$P_{\text{loss,PMSM}} = P_{\text{res}} + P_{\text{co}}. \tag{3.2}$$

The resistive losses arise due to the resistance in the stator winding (losses in the rotor are neglected due to the permanent excitation of the rotor magnets). They are dependent on both temperature and frequency. In the dq-reference frame, the resistive losses can be expressed as

$$P_{\text{res}} = \frac{3}{2} R_s \left(i_d^2 + i_q^2 \right) \tag{3.3}$$

where amplitude-invariant dq-transformation is assumed.

As mentioned in Section 2.1.7, core losses are typically predicted using finite element methods in the design stage of the PMSM. For control purposes, complicated loss models are not practical and, if taken into account, the core loss resistance, R_c, as shown in Fig. 2.7, is typically added. Since R_c represents different phenomena, its value will change with shifting operating points; often it is modeled only as a nonlinear function of the rotor speed (frequency), ω_r. Of course, since no current dependence of R_c is assumed with this simple representation of core losses, the representation is not valid for operating conditions with large loads (currents).

From (2.26)–(2.28) and Fig. 2.7, the core losses can be expressed as

$$\begin{aligned} P_{\text{co}} = \frac{3}{2} R_c \left(i_{d,c}^2 + i_{q,c}^2 \right) = \frac{3 R_c \omega_r^2}{2(R_c^2 + \omega_r^2 L_d L_q)^2} \left[(R_c L_d i_d + \psi_m R_c + \omega_r L_d L_q i_q)^2 \right. \\ \left. + L_q^2 (R_c i_q - \omega_r (L_d i_d + \psi_m))^2 \right]. \end{aligned} \tag{3.4}$$

As the core loss resistances are added, this will also affect the expression for the electrical torque. The part of the input power that produces electrical torque is given by (see also Fig. 2.7)

$$P_{T_e} = \frac{3}{2} \left[-\omega_r L_q i_{q,0} i_{d,0} + (\omega_r L_d i_{d,0} + \omega_r \psi_m) i_{q,0} \right]. \tag{3.5}$$

Hence, the torque expression is given by $T_e = n_p P_{T_e} / \omega_r$ which, expressed using i_d and i_q, can be written as

$$\begin{aligned} T_e = \frac{1}{2(R_c^2 + \omega_r^2 L_d L_q)^2} \left(3 n_p R_c [R_c i_q - \omega_r (L_d i_d + \psi_m)][(\psi_m - \Delta L i_d) R_c^2 \right. \\ \left. - \omega_r L_q \Delta L R_c i_q + \omega_r^2 L_q^2 \psi_m] \right). \end{aligned} \tag{3.6}$$

Of course, if core losses are neglected ($R_c \to \infty$), the standard torque expression (harmonics are neglected) is obtained, i.e.,

$$\lim_{R_c \to \infty} T_e = \frac{3n_p}{2} \left(\psi_m i_q - \Delta L i_d i_q \right). \tag{3.7}$$

3.2.1 Loss Minimization Conditions

Since friction losses are dependent only on rotor speed, they cannot be affected by control action. However, an analytical loss minimization condition can be derived by finding the d-current that minimizes the electrical losses assuming constant torque and speed. Hence, the loss minimization condition is obtained by solving for i_d in:

$$\frac{\partial P_{\text{loss,PMSM}}}{\partial i_d} = 0 \tag{3.8}$$

$$\frac{\partial T_e}{\partial i_d} = 0. \tag{3.9}$$

where (3.8) is solved for constant ω_r. Eq. (3.9) is used for obtaining an expression for $\partial i_q / \partial i_d$ and is also solved assuming constant ω_r.

In [51], (3.8) and (3.9) are solved analytically using another model of the core losses. In [64], core losses are modeled with the core loss resistance, but (3.8) and (3.9) are differentiated with respect to $i_{d,0}$. The current $i_{q,0}$ is then found by solving for $i_{q,0}$ in the torque expression (expressed using $i_{d,0}$ and $i_{q,0}$). Finally, the currents i_d and i_q are obtained from $i_{d,0}$ and $i_{q,0}$. A similar method is used in [37], although numerical methods are used to find the solutions.

For completeness, an analytical solution to (3.8) and (3.9) is presented in Appendix C and it is given by (C.3). Unfortunately, this solution, $i_d(i_q)$, is complicated and hardly suitable for implementation on a DSP. However, some remarks can be made. First, it can be noted that $i_d(i_q)$ is strongly dependent both on rotor speed and motor parameters [85], including the stator resistance. Since both stator resistance and the magnetic flux will vary with temperature, it is important that if $i_d(i_q)$ is determined experimentally, care must be taken so that a thermal steady-state condition is reached before measurements are made. Dependence on rotor speed is expected, since the core losses increase with increasing frequency, which must be reflected in the solution.

Secondly, if core losses are neglected ($R_c \to \infty$) or zero rotor speed is assumed ($\omega_r \to 0$), the well known max torque-per-ampere solution is found, i.e.,

$$\lim_{R_c \to \infty} i_d(i_q) = \lim_{\omega_r \to 0} i_d(i_q) = \frac{\psi_m}{2\Delta L} - \sqrt{\left(\frac{\psi_m}{2\Delta L} \right)^2 + i_q^2}. \tag{3.10}$$

Fig. 3.1 shows a plot of (C.3), where fixed motor parameters have been assumed, saturation of L_q is neglected, and the rotor speed is varied as $\omega_r = \{0,\ 0.5,\ 1\}$ pu. The core loss resistance, R_c, is assumed to be constant: $R_c = 30$ pu. In order to demonstrate the validity of (C.3), the squares (□) are results obtained using numerical methods. It can be seen that, when the rotor speed is increased, more negative i_d should be added, as compared to the results given by (3.10).

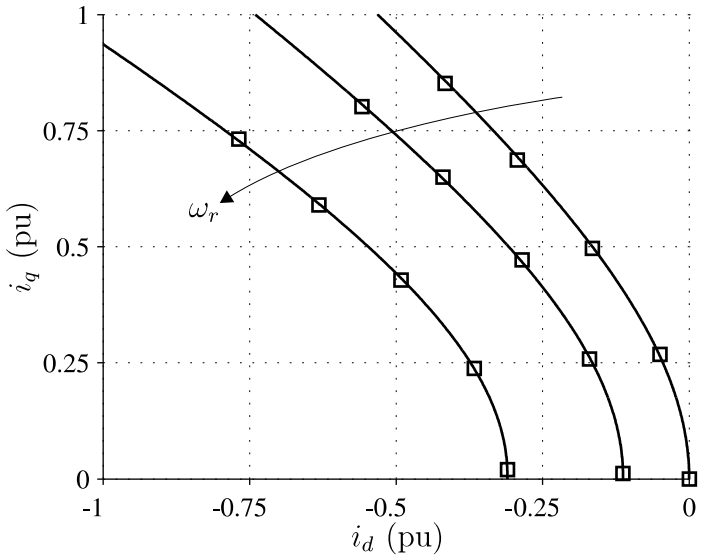

Fig. 3.1 Solution curves for $i_d(i_q)$ for $\omega_r = \{0,\ 0.5,\ 1\}$ pu. The arrow indicate increasing ω_r. The squares (□) are results found using a numerical method. The solution $i_d(i_q)$ for $\omega_r = 0$ pu is identical to the solution given by (3.10).

In [51], the core losses are not modeled with a resistance R_c, but rather as a nonlinear function of current and rotor speed but, as expected, similar results are obtained (compare to [51], Fig. 5).

3.3 Case Study

The PMSM and inverter used in the experiments is developed for propulsion in an HEV application. In order to investigate to what extent losses can be reduced by control action in this application, a case study, based on simulations, is presented in this section.

3.3.1 Identification of R_c

Except for R_c, all parameters of the PMSM are known and they are found in Appendix B. In order to take core losses into account when minimizing losses by con-

trol means, the core loss resistance, R_c must be known with sufficient accuracy. Methods for identifying R_c are given in [6, 84, 88]. Unfortunately, the method presented in [6] requires that core losses are a significant part of input power. This cannot be fulfilled for the PMSM used in the experiments since the dc machine acting as load, connected through a reduction gearbox, makes the mechanical losses too large to neglect. The dc machine cannot be easily disconnected due to the fact that a careful and expensive lining-up procedure is needed due to the high speed of the PMSM. The method presented in [84] requires knowledge of the stator resistance and is developed for non-salient PMSMs. The method given in [88] also requires knowledge of stator resistance and core and friction losses must be separated. The PMSM used in the experiments is water cooled, which offers the possibility to measure no-load core losses by measuring the temperature difference between the inlet and outlet water. Provided that rotor and friction losses are small (or taken into account) and leakage losses are estimated with sufficient accuracy, the no-load core losses can be identified for different rotor speeds [2]. As the no-load core losses are measured, values of the core loss resistance, as a function of rotor speed, $R_c(\omega_r)$, can then be computed.

As the calorimetric method can provide accurate measurements of core losses, it is very time consuming and has not been utilized in this thesis. To obtain a rough estimate of $R_c(\omega_r)$ to be used in the case study, Fig. 3.2 shows $R_c(\omega_r)$, adapted from previous measurement results where core losses have been estimated by subtracting modeled friction losses (assuming a smooth rotor surface) from the mechanical input power (obtained by measuring torque and rotor speed). Therefore, R_c will represent the total core losses, including those arising due to flux harmonics. Because of this, the value of R_c that represents core losses due to the fundamental should be somewhat larger (yielding smaller losses). Included is also the measured stator resistance as a function of frequency at room temperature with the rotor unmounted (adapted from [28]).

Remark: Since the core loss resistance is identified only for no-load conditions, the value of R_c may change with increased load. Hence, only small loads will be considered in the simulations. A complete utilization of loss minimization would require measurements at several different rotor speeds and output torques.

3.3.2 Impact of Electrical Losses in the PMSM

For the PMSM used in the experiments, L_d, L_q, and ψ_m have been measured using the methods presented in [6]. The stator resistance, R_s, is increased by 30 percent,

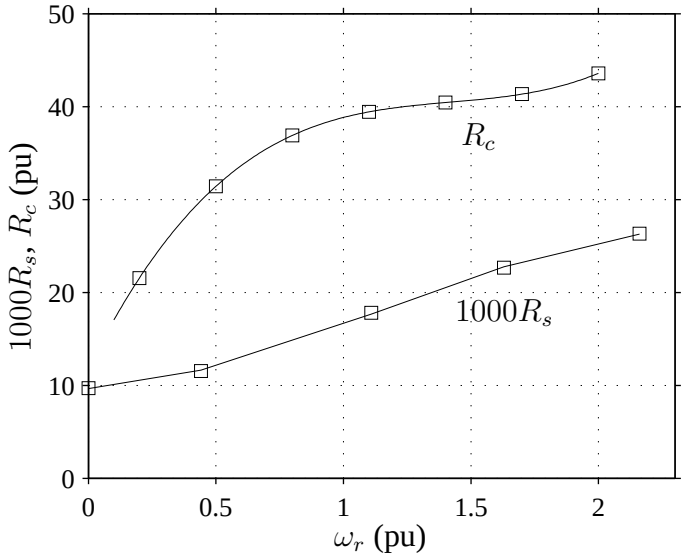

Figure 3.2: Measured stator resistance, $R_s(\omega_r)$, at room temperature with the rotor unmounted and estimated core loss resistance, $R_c(\omega_r)$.

since the measured values are given at room temperature. Thus, at least for small loads, all parameters of the PMSM are known and comparisons between different control strategies, with respect to electrical losses in the PMSM, can be performed. Fig. 3.3 shows simulated electrical losses for three control strategies: zero d-current, max torque-per-ampere current ($i_d(i_q)$ given by 3.10) and loss-minimization control ($i_d(i_q)$ given by C.3). The simulation is made for three different speeds: $\omega_r = 0.5$, 0.75, and 1 pu.

It is clear from Fig. 3.3 that loss-minimization control is efficient only at speeds near (and above) base speed. This is expected because of the dependence of core losses on rotor speed. Only low output torques are considered (due to the uncertainty in R_c for large currents). Operation with minimized electrical losses is possible also above base speed if only low torques are considered, since the resistive voltage losses are small and additional restrictions on i_d, due to the lack of available voltage, are not needed.

3.3.3 Drive Cycle Simulation

Using loss charts for the PMSM, vehicle dynamics, transmission and inverter, a drive cycle simulation model has previously been developed [28, 45]. The effect of different control methods is not reflected in the loss charts, but the drive cycle simulations can still be useful to determine if the PMSM operates significant times

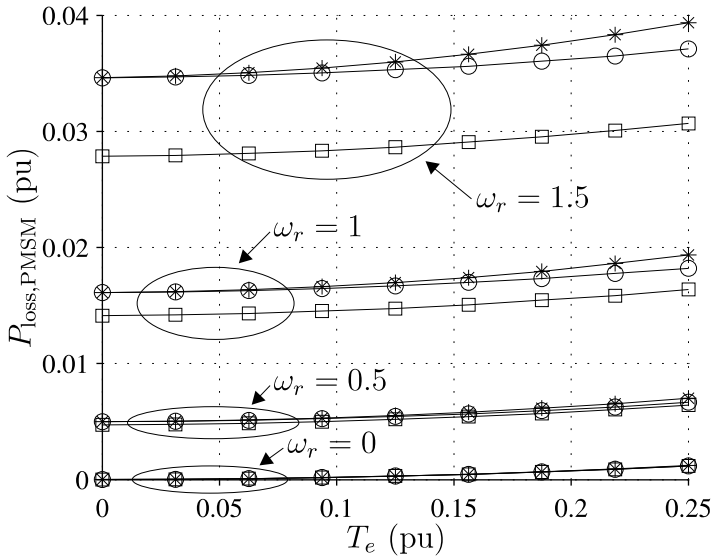

Figure 3.3: Simulated losses at three different rotor speeds ($\omega_r = 0, 0.5, 1$, and 1.5 pu) for zero d-current, indicated by asterisks ($*$), max torque-per-ampere ($\circ$) and loss minimization control ($\square$).

in regions where loss-minimization control may be of benefit. The U.S. FTP-72, shown in Fig. 3.4a), is chosen as a relevant driving cycle since it simulates an urban route with frequent stops [20]. Fig. 3.4b) presents one-second samples of operating points for the PMSM (torque and speed) when operating in the U.S. FTP-72 driving cycle. Clearly, there is a region containing operating points with high speeds and small torques (indicated with a circle). Within this region, operation with minimized motor losses is attractive, when considering motor losses only, as compared to both operation with zero d-current and max torque-per-ampere control. Naturally, this possibility to reduce losses will be more pronounced for drive cycles containing more operating points at high speeds, i.e., highway driving.

3.3.4 Impact of Inverter Losses

As the electrical drive system consists of both PMSM and inverter, the impact of inverter losses should also be considered. A model of inverter losses, suitable for comparisons, can be found in [1]. The voltage drop and resistance of the diode and transistor are approximately equal respectively for the inverter used (see Appendix B for data of the inverter). Therefore, the loss model in [1] can be further simplified and the conduction losses in each inverter leg can be approximated as [68]:

$$P_{\text{cond}} = \frac{2\sqrt{2}VI_{\text{rms}}}{\pi} + rI_{\text{rms}}^2 \tag{3.11}$$

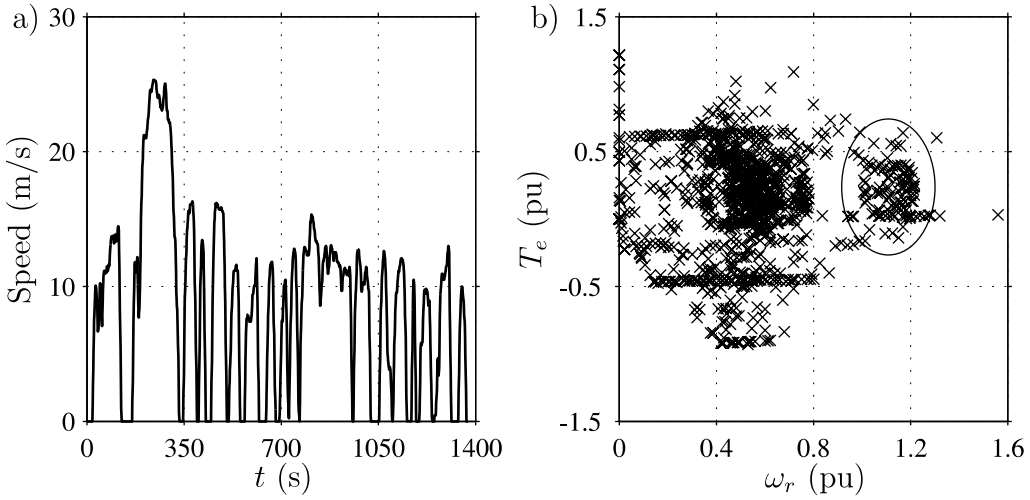

Fig. 3.4 a) The U.S. FTP-72 driving cycle. b) Corresponding operating points (one second samples) for the PMSM.

where $V = V_{CEO} \approx V_{TO}$ is the transistor (and diode) on stage voltage, $r = r_{CE} \approx r_T$ is the transistor (and diode) lead resistance and $I_{\rm rms}$ is the root mean square (RMS) value of the (sinusoidal) current to the PMSM. Assuming that the switching losses in the transistor are proportional to the current [1], the switching losses in each inverter leg can be approximated as

$$P_{\rm s,T} = (E_{\rm on} + E_{\rm off}) \frac{2\sqrt{2} I_{\rm rms} f_{\rm sw}}{\pi I_{c,\rm nom}} \tag{3.12}$$

$$P_{\rm s,D} = E_{rr} f_{\rm sw} \tag{3.13}$$

where $E_{\rm on}$ and $E_{\rm off}$ are the turn-on and turn-off energy losses for the transistor, $f_{\rm sw}$ is the switching frequency, $I_{c,\rm nom}$ is the nominal current through the transistor, and E_{rr} is the reverse recovery energy of the diode. The total losses of the three inverter legs can now be approximated as

$$P_{\rm loss,inv} = 3\left(P_{\rm cond} + P_{\rm s,T} + P_{\rm s,D}\right). \tag{3.14}$$

The transistors used in the inverter are insulated gate bipolar transistors (IGBTs). From the specifications of the IGBTs [57], approximations of the parameters introduced above can be identified. They are also summarized in Appendix B.

Taking inverter losses into account when computing the set of i_d and i_q that, for a given torque and speed, minimizes losses is preferably accomplished using numerical methods. Fig. 3.5 shows a simulation result for $0 \leq T_e \leq 0.25$ pu and $\omega_r = 0.5$, 0.75, and 1 pu. The zero d-current control method is indicated with asterisks ($*$), max torque-per-ampere with circles ($\circ$), minimization of motor losses

with squares (□), and minimization of motor+inverter losses indicated with diamonds (◇). The zero d-current, max torque-per-ampere, and minimization of motor losses corresponds to the results given in Fig. 3.3 (where only motor losses are presented). The result shows that, due to the extra inverter losses, the advantage of adding negative i_d in order to minimize motor losses, is reduced significantly. The corresponding losses (motor+inverter) are shown in Fig. 3.6. Even for high speeds, the difference in losses between minimization of motor+inverter losses and max torque-per-ampere control is very small. For larger torques, the difference becomes larger, but since the core loss resistance is computed for a no-load condition, no certain conclusion can be made for operating points with larger torques.

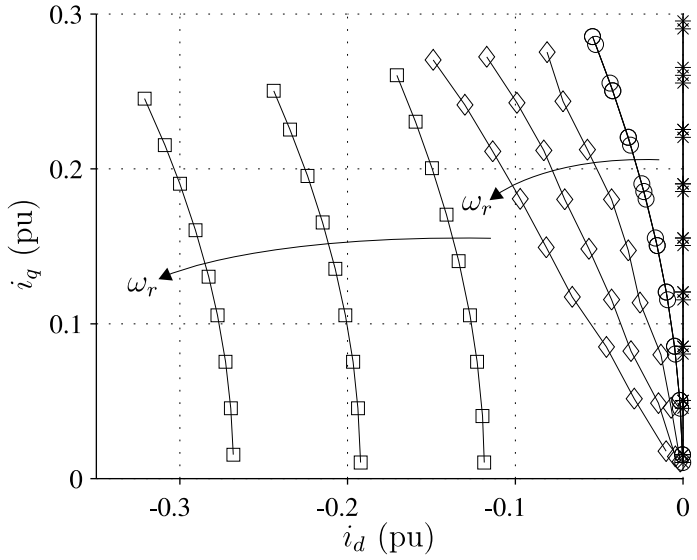

Figure 3.5: Corresponding currents for the results given in Fig. 3.6. Zero d-current indicated with asterisks (∗), max torque-per-ampere (○), minimization of motor losses (□), and minimization of total losses, including inverter (◇).

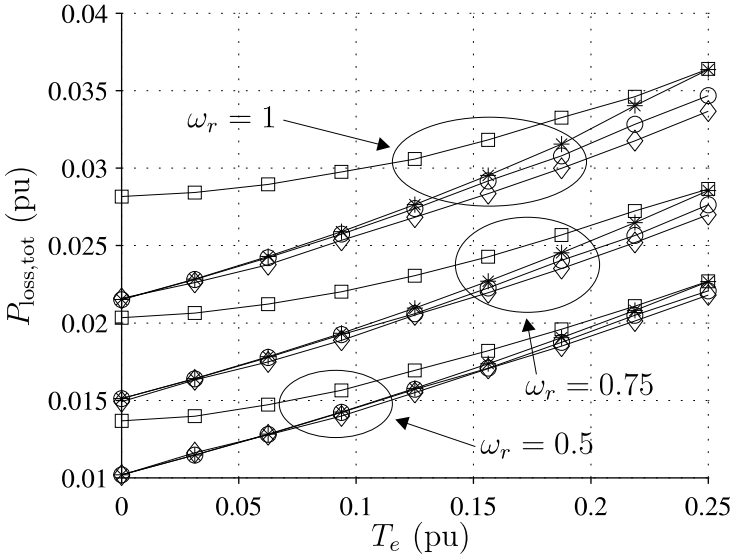

Figure 3.6: Simulated losses, taking inverter losses into account, for three rotor speeds ($\omega_r = 0.5$, 0.75 and 1 pu) for zero d-current ($*$), max torque-per-ampere ($\circ$), minimization of motor losses ($\square$), and minimization of total losses, including inverter ($\diamond$).

3.4 Summary of Chapter

This chapter has reviewed methods for achieving operation with minimized losses, by means of control. The technique is general and can be applied to any electrical drive system using a PMSM and inverter. The impact of reduced losses on the experimental PMSM and inverter was investigated, through simulations, by a case study. The result of the case study showed that although the PMSM operates a significant part in regions where the reduction of losses in the PMSM, by means of control, is beneficial, the additional inverter losses reduce the amount of energy gain considerably. This further enlightens that when designing electrical drive systems for EVs and HEVs, the impact of losses in both power electronics and electrical motors should not be considered separately.

Chapter 4

Speed and Position Estimation

In this chapter, rotor position and speed estimation, i.e., sensorless control, of salient PMSMs is discussed. A brief overview of different methods found in the literature is presented. The phase-locked loop (PLL) type algorithm proposed by Harnefors and Nee [26] is analyzed extensively and improvements are proposed, thus making the estimator suitable for vehicle applications. The results of the analysis are supported by simulations and experimental results.

4.1 Overview

As is well known, there are, in principle, two different methods of obtaining estimates of speed and rotor position in a vector controlled PMSM.

In the first category, information is obtained from the back EMF. The number of contributions here is vast, recent examples, presenting different types of estimator designs, are [4, 8, 14, 24, 61, 67]. These estimators show good performance in the medium and high speed regions. Since the back EMF vanishes at low speeds, low and zero speed operation is challenging, although recent research has moved towards a solution to this problem [24, 59, 73, 89].

In the second category, a high-frequency carrier signal is added, and information is obtained provided that the machine possesses rotor anisotropy, i.e., saliency. The algorithms proposed are typically variants of the high-frequency signal injection presented in [19] or the INFORM method [75]. Recent examples are found in [18, 22, 70]. Although this technique allows for zero- and low-speed operation, obvious drawbacks of the technique are that it, at least to some extent, leads to acoustic noise, torque ripple and increased losses. If the PMSM possesses saliency, a combination of the two categories are typically used where high-frequency signal

injection methods are relied on at low speeds and a transition to back-EMF estimation methods is performed at higher speeds.

In a vehicle application, the PMSM must operate at all speeds (including zero speed). Only very small steady-state estimation errors are allowed due to reasons of energy efficiency. Operation deep into the field-weakening region can be expected and stable (safe) operation at all possible operating points must be guaranteed. Naturally, these demands can be fulfilled by accurately tune a specific estimator, connected to a specific drive. However, to support results obtained from measurements, analysis of the algorithms should be carried out to better understand their properties at different modes of operation. Preferably, to simplify an implementation, design rules for all parameters introduced should also be presented.

This chapter considers the implementation of a speed and position estimator for a salient PMSM in a vehicle application. An estimator of phase-locked-loop (PLL) type, previously developed by Harnefors and Nee [26], is modified to take into account effects, such as saliency, large d-currents and operation in the whole speed region. A technique to improve the estimator's capability to handle large speed estimation errors is also presented. Design rules for the selection of all parameters, that removes the initial tuning procedure, are proposed. The estimator is then evaluated, with good results, by simulations and experimental results. Although a specific speed and position estimator is considered, the principle of the analysis is general, and should also be applicable to other candidate estimators.

4.2 General Properties of the PLL-Type Algorithm

The PLL-type speed and position estimation algorithm presented in [26] has the following form

$$\dot{\hat{\omega}}_r = \gamma_1 e \tag{4.1}$$

$$\dot{\hat{\theta}} = \hat{\omega}_r + \gamma_2 e \tag{4.2}$$

where $\hat{\omega}_r$ is the estimated rotor speed, $\hat{\theta}$ is the estimated rotor position, γ_1 and γ_2 are estimator gains, and e is the error signal used to correct the estimator updates (in [26], ε is used to denote the error signal). The error signal, e, contains an angular estimation error and is obtained using information from a back-EMF estimate or using signal-injection techniques. These two methods will be described in detail in this chapter. However, both methods will produce an error signal in the following

form[1]

$$e = \sin\tilde{\theta} \tag{4.3}$$

where $\tilde{\theta}$ denotes the angular estimation error, $\tilde{\theta} = \theta - \hat{\theta}$.

The function of the estimator can be explained as follows. For small angular estimation errors, the error signal, e, can be approximated as $e = \sin\tilde{\theta} \approx \tilde{\theta}$. Hence, if $\theta > \hat{\theta}$, and provided that $\gamma_1 > 0$, (4.1) states that $\hat{\omega}_r$ will increase, i.e., the estimator will "catch up" and this update in $\hat{\omega}_r$ will increase as long as $\tilde{\theta} \neq 0$. As seen in (4.2), the rotor-angular estimate is not only updated as the integral of the speed estimate, but corrected with error the signal, $\gamma_2 e$ to further assure correct operation.

Local Stability

For $e = \sin\tilde{\theta}$ and assuming $\dot{\omega}_r = 0$, i.e., no acceleration (the impact of $\dot{\omega}_r \neq 0$ is investigated below), the error dynamics of (4.1) and (4.2) are governed by

$$\dot{\tilde{\omega}}_r = -\dot{\hat{\omega}}_r = -\gamma_1 \sin\tilde{\theta} \tag{4.4}$$

$$\dot{\tilde{\theta}} = \dot{\theta} - \dot{\hat{\theta}} = \tilde{\omega}_r - \gamma_2 \sin\tilde{\theta}. \tag{4.5}$$

Equilibrium points of (4.4) and (4.5) are given by $\{\tilde{\omega}_r^\star, \tilde{\theta}^\star\} = \{0, n\pi\}$ where n is an integer. Naturally, the equilibrium points given by $\{\tilde{\omega}_r^\star, \tilde{\theta}^\star\} = \{0, 2n\pi\}$ should be stable and well damped, since they correspond to perfect field orientation. Linearizing (4.4) and (4.5) around $\{\tilde{\omega}_r^\star, \tilde{\theta}^\star\} = \{0, 2n\pi\}$, the characteristic polynomial, $c(p)$, is found as

$$c(p) = p^2 + \gamma_2 p + \gamma_1. \tag{4.6}$$

By choosing the gain constants γ_1 and γ_2, arbitrary placement of the two poles, i.e., the solutions to $c(p) = 0$, is possible. In order to obtain a well damped system (reducing the impact of noise and oscillations), the poles of the linearized system are placed in $p_{1,2} = -\rho$, where ρ is a positive, real constant, which can be chosen arbitrarily. This leads to the following selection for the gain parameters γ_1 and γ_2:

$$\gamma_1 = \rho^2, \quad \gamma_2 = 2\rho. \tag{4.7}$$

With this selection of γ_1 and γ_2, the poles of the equilibrium points $\{\tilde{\omega}_r^\star, \tilde{\theta}^\star\} = \{0, n\pi\}$, n odd, are given by $p_{1,2} = \rho(1 \pm \sqrt{2})$. As $p_1 > 0$, this set of equilibrium

[1] For the signal-injection method, $\sin\tilde{\theta}$ should be replaced by $\frac{\sin 2\tilde{\theta}}{2}$.

points are unstable, which is attractive since they correspond to an angular estimation error of π electrical radians.[2]

Impact of Noise

Around the stable equilibrium points, $\sin\tilde{\theta}$ can be approximated as $\sin\tilde{\theta}\approx\tilde{\theta}$, an approximation which also was used in the linearizing procedure above. However, in practice, there will be noise in the error signal e, arising due to disturbances such as harmonics and measurement noise. Hence, $e\approx\tilde{\theta}-\nu$, where ν is the noise term. A block diagram of the error dynamics (4.4) and (4.5) is shown in Fig. 4.1.

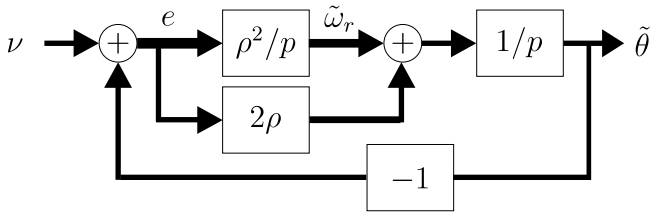

Fig. 4.1 Block diagram of the error dynamics (4.4) and (4.5), where ν represents additional noise added to the error signal e.

The transfer functions from ν to $\tilde{\omega}_r$ and ν to $\tilde{\theta}$ are given as

$$G_{\nu,\tilde{\omega}_r}(p)=\frac{\rho^2 p}{(p+\rho)^2} \tag{4.8}$$

$$G_{\nu,\tilde{\theta}}(p)=\frac{\rho(2p+\rho)}{(p+\rho)^2} \tag{4.9}$$

respectively. As the estimated speed is used in the current controller, it is vital that the noise content of the speed estimation error is low. A Bode diagram of $|G_{\nu,\tilde{\omega}_r}(j\omega)|$ for $\rho=0.05$, 0.1 and 0.2 pu is shown in Fig. 4.2. As seen, the impact of noise on the speed estimate is most severe for noise frequencies around $\omega\approx\rho$. Also, the peak magnitude of $|G_{\nu,\tilde{\omega}_r}(j\omega)|$ is given by $\max(|G_{\nu,\tilde{\omega}_r}(j\omega)|)=\rho/2$; it is increasing linearly with increased ρ. Thus, ρ should not be selected larger than necessary (to achieve good tracking) as the sensitivity to noise then would increase.[3]

Regarding $|G_{\nu,\tilde{\theta}}(j\omega)|$, the peak magnitude is found as $\max\big(|G_{\nu,\tilde{\theta}}(j\omega)|\big)=2/\sqrt{3}$, which is obtained at $\omega=\rho/\sqrt{2}$.

[2]The estimated d-axis is then aligned to a magnetic south pole of the rotor rather than a north pole, which corresponds to perfect field orientation.

[3]A typical choice for ρ used in the experiments is $\rho=0.1$ pu. Hence, noise of frequencies around $\omega\approx0.1$ pu, will be magnified by approximately 35 dB (obtained from Fig. 4.2).

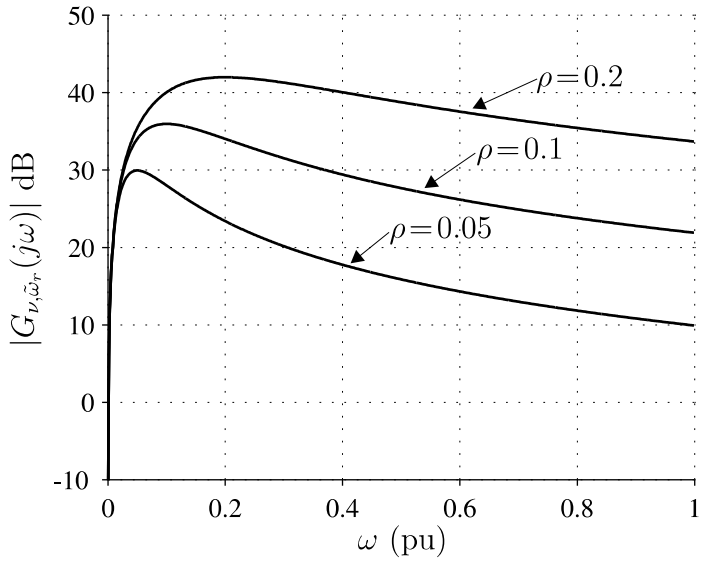

Fig. 4.2 Bode diagram of $|G_{\nu,\tilde{\omega}_r}(j\omega)|$ for three typical selections of the gain constant ρ.

4.2.1 Non-Linear Effects

Proof of Stability

The error dynamics given by (4.4) and (4.5) are nonlinear due to the $\sin\tilde{\theta}$ expression. Therefore, not only the local stability properties of the equilibrium points, determined by the locations of the poles, but also the global stability properties should be taken into account. In [26], stability of (4.4) and (4.5) is shown using Lyapunov theory [39].

Loss of Synchronism – Cycle Slips

The described estimator possesses many attractive properties. First, the estimator will always converge to the locally stable equilibrium points, which was shown using Lyapunov theory. Thus, any estimation error will be recovered from. Secondly, the poles of the equilibrium points are located at $p_{1,2} = -\rho$. Thus, the system is well damped which will increase the estimator's ability to quickly recover from minor deviations from the equilibrium points.

By normalizing the angular frequency and time by introducing $\tilde{\Omega}_r = \tilde{\omega}_r/\rho$ and $\tau = \rho t$, the error dynamics, given by (4.4) and (4.5), with the selection of γ_1 and γ_2 given by (4.7), can be expressed as

$$\dot{\tilde{\Omega}}_r = -\sin\tilde{\theta} \tag{4.10}$$

$$\dot{\tilde{\theta}} = \tilde{\Omega}_r - 2\sin\tilde{\theta}. \tag{4.11}$$

Studying (4.10) and (4.11) instead of (4.4) and (4.5) allows conclusions to be made which are not directly dependent on the parameter ρ, although the time scale, of course, is changed.

Since the system is of second order, drawing phase portraits is a useful technique for analyzing the systems behavior far away from the equilibrium points and by doing this, an interesting property is revealed.

Fig. 4.3 shows a phase portrait of (4.10) and (4.11). Of particular importance are the *separatrices*, i.e., the solutions that converge to the saddle points at $\tilde{\Omega}_r = \tilde{\omega}_r/\rho = 0$, $\tilde{\theta} = n\pi$, n odd. These divide the phase plane into convergence regions. If the estimator is initialized in the region enclosed by separatrices A and B, $\tilde{\theta}$ will converge to 0. However, if initialized in the region enclosed by separatrices B and C, $\tilde{\theta}$ will converge to 2π, and so forth. This means that the estimator falls one or more revolutions behind the machine (*cycle slips* in PLL terminology [80] and *pole slipping* in synchronous machine terminology [74]); synchronism is temporarily lost. Note that the separatrices are stacked densely for $|\tilde{\Omega}_r| > 3 \Rightarrow |\tilde{\omega}_r| > 3\rho$; initialization at $\tilde{\theta} \approx 0$, $|\tilde{\omega}_r| > 3\rho$ may, thus, lead to numerous cycle slips, giving a long re-synchronization process. This is unacceptable, and should, if possible, be avoided.

While selecting ρ larger (a selection rule is given in (4.74)) would improve the situation, this also increases the estimator's sensitivity to disturbances, as discussed above. Therefore, ρ should only be large enough to cope with accelerations that occur normally, while a function by which abnormally rapid accelerations can be handled safely should be incorporated. A method to achieve this is presented in Section 4.6.

4.3 Signal Injection

The input of the PLL-type estimator discussed in the previous section is the error signal, e, which ideally has the form $e = \sin\tilde{\theta}$. Two methods how to obtain this signal will be discussed, here and in Section 4.4, respectively.

The first method is based on adding an additional high-frequency voltage and obtaining the error signal from the produced high-frequency content in the current. The method was, in this form, first presented by Corley and Lorenz [19]. The key idea is to inject a high-frequency voltage, $V_e \cos\omega_e t$, in the d-direction *seen by the control system*, i.e., determined by $\hat{\theta}$. Due to saliency, spatial information can obtained in the estimated q-component of the current. The technique can be explained as follows.

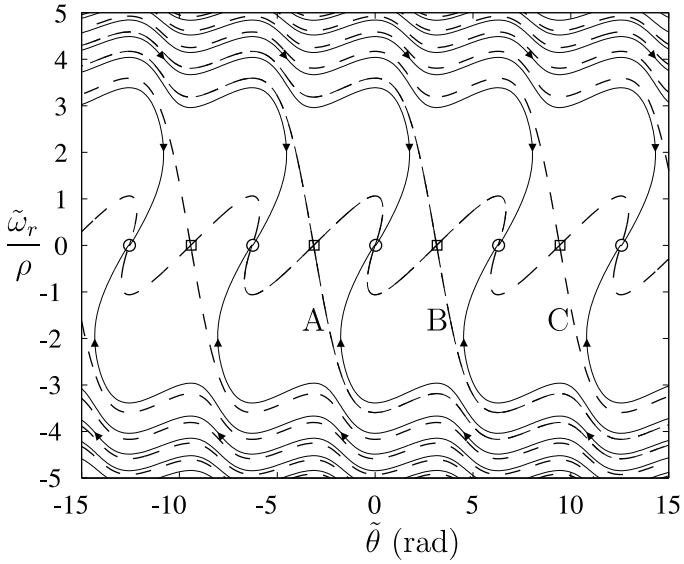

Fig. 4.3 Phase portrait of the error dynamics of the estimator. Solid lines indicate solution curves. The dashed lines are the separatrices of the saddle points at $\{\tilde{\omega}_r, \tilde{\theta}\} = \{0, n\pi\}$, n odd, indicated by squares (□). The circles (○) mark the stable equilibrium points at $\tilde{\theta} = n\pi$, n even.

The voltage equation in rotor-fixed dq-coordinates is, from (2.14), given as

$$\mathbf{v} = (\mathbf{Z} + p\mathbf{L})\,\mathbf{i} + \omega_r \boldsymbol{\psi}_m \tag{4.12}$$

where $p \to d/dt$ and the subscripts, dq, have been dropped. Neglecting the inductance harmonics, $\mathbf{Z}$ and $\mathbf{L}$ are found as

$$\mathbf{Z} = \begin{bmatrix} R_s & -\omega_r L_q \\ \omega_r L_d & R_s \end{bmatrix} \qquad \mathbf{L} = \begin{bmatrix} L_d & 0 \\ 0 & L_q \end{bmatrix}. \tag{4.13}$$

Furthermore, neglecting the flux-linkage harmonics, $\boldsymbol{\psi}_m = [0\ \psi_m]^T$.

Now, a set of *estimated rotor coordinates* is introduced, displaced with the angle $\tilde{\theta} = \theta - \hat{\theta}$. The true dq-coordinate system, fixed to a magnetic north pole of the rotor, as well as the estimated coordinate system are shown in Fig. 4.4. The transformation of a general current or voltage vector, $\mathbf{f} = [f_d\ f_q]^T$, is given by $\hat{\mathbf{f}} = e^{\mathbf{J}\tilde{\theta}}\mathbf{f}$, where $\hat{\mathbf{f}} = [f_{\hat{d}}\ f_{\hat{q}}]^T$. The matrices $\mathbf{J}$ and $e^{\mathbf{J}\tilde{\theta}}$ are introduced as:

$$e^{\mathbf{J}\tilde{\theta}} = \begin{bmatrix} \cos\tilde{\theta} & -\sin\tilde{\theta} \\ \sin\tilde{\theta} & \cos\tilde{\theta} \end{bmatrix}, \quad \mathbf{J} = \begin{bmatrix} 0 & -1 \\ 1 & 0 \end{bmatrix}. \tag{4.14}$$

Now, a high-frequency voltage, with amplitude V_e and angular frequency ω_e, is injected in the $\hat{d}$-direction. Thus, the voltage vector, expressed in the set of estimated

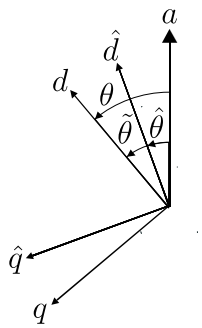

Fig. 4.4 Definition of the rotor-fixed dq-coordinates and their estimates.

coordinates, is given by

$$\hat{\mathbf{v}} = [V_e \cos \omega_e t \;\; 0]^T . \tag{4.15}$$

As will be shown, the method has drawbacks which makes it suitable only for zero- and low-speed operation. Therefore, $\omega_r \approx 0$ is assumed. The current vector, expressed in estimated rotor coordinates, is then given by

$$\hat{\mathbf{i}} = e^{\mathbf{J}\tilde{\theta}} \left(\mathbf{Z} + p\mathbf{L}\right)^{-1} e^{-\mathbf{J}\tilde{\theta}} \hat{\mathbf{v}}. \tag{4.16}$$

Assuming that $\tilde{\theta}$ changes slowly as compared to the frequency ω_e, it can be viewed as a slowly varying parameter. Eq. (4.16) can then be solved analytically using the traditional $j\omega$-method. The steady-state solution for the current in the $\hat{q}$-direction can then be found as

$$i_{\hat{q}} = \frac{\omega_e (L_d + L_q) R_s \cos \omega_e t + (\omega_e^2 L_d L_q - R_s^2) \sin \omega_e t}{2(R_s^2 + \omega_e^2 L_d^2)(R_s^2 + \omega_e^2 L_q^2)} V_e \omega_e \Delta L \sin 2\tilde{\theta}. \tag{4.17}$$

Thus, rotor position information is found in $i_{\hat{q}}$, due to the term $\sin 2\tilde{\theta}$, provided that the machine possesses saliency, i.e., $\Delta L \neq 0$. Naturally, $i_{\hat{q}}$ will also contain a dc component if $i_q^{\text{ref}} \neq 0$. This can be removed by adding a high-pass filter with a very low angular cut-off frequency, ω_{hp}, typically corresponding to only a few Hertz [46]. Since the frequency of the added signal is perfectly known, demodulation of the signal can easily be performed. Thus, the $\hat{q}$-current is then demodulated, i.e., multiplied by $\sin \omega_e t$, and filtered using a low-pass filter with the angular cut-off frequency ω_{lp}. Since $\sin^2 \omega_e t = (1 - \cos 2\omega_e t)/2$, the low-pass filtered current is a dc component containing rotor position information. This signal, e_{si}, is then found as

$$\begin{aligned} e_{\text{si}} &= \text{LPF}\{\text{HPF}\{i_{\hat{q}}\} \sin \omega_e t\} \\ &= \frac{V_e \omega_e \Delta L \left(\omega_e^2 L_d L_q - R_s^2\right)}{4(R_s^2 + \omega_e^2 L_d^2)(R_s^2 + \omega_e^2 L_q^2)} \sin 2\tilde{\theta} = K_e' \sin 2\tilde{\theta} \end{aligned} \tag{4.18}$$

where ideal filters has been assumed. Provided that $R_s \ll \omega_e L_d$ (which is a reasonable assumption), e_{si} can be simplified to

$$e_{\text{si}} \approx \frac{V_e \Delta L}{4\omega_e L_d L_q} \sin 2\tilde{\theta} = K_e \sin 2\tilde{\theta}. \tag{4.19}$$

Hence, e_{si} contains suitable information of the angular error and (4.19) can be used as an error signal for the estimator (4.1) and (4.2). So, when using the signal-injection technique, the error signal, e, is obtained as

$$e = \frac{e_{\text{si}}}{2\hat{K}_e} \approx \frac{\sin 2\tilde{\theta}}{2} \approx \sin \tilde{\theta} \tag{4.20}$$

where the approximation is valid for no parameter errors and small $\tilde{\theta}$. $\hat{K}_e$ is an estimate of K_e using estimated parameters $\hat{L}_d$ and $\hat{L}_q$. Note that even with perfect knowledge of the inductances and assuming an ideal inverter, $\hat{K}_e$ will not be equal to the true value K_e' due to the impact of the stator resistance.

4.3.1 Operation Without Filters

As seen in Fig. 4.2, the estimator is sensitive to noise of frequencies around $\omega \approx \rho$. However, it is reasonable to assume that the frequency of the injected signal is much higher compared to ρ. Fig. 4.2 also shows that frequencies much higher than ρ are strongly damped ($\lim_{\omega \to \infty} G_{\nu,\tilde{\omega}_r}(j\omega) = 0$) . Hence, it is useful to investigate if any, or both, of the filters used can be removed (simplifying the estimator somewhat), since the estimator itself has band-pass filter characteristics.

Operation Without Low- and High-Pass Filters

As shown above, the current in the estimated q-direction (assuming accurate model parameters) is given by

$$i_{\hat{q}} = 2K_e \sin \omega_e t \sin 2\tilde{\theta} + i_{q0} \approx 4K_e \sin(\omega_e t)\tilde{\theta} + i_{q0} \tag{4.21}$$

where i_{q0} is the dc component and the approximation $\sin 2\tilde{\theta} \approx 2\tilde{\theta}$ has been used. As above, $i_{\hat{q}}$ is demodulated and the error signal is obtained as

$$e = \frac{i_{\hat{q}} \sin \omega_e t}{2K_e} \approx \tilde{\theta} + \underbrace{\frac{i_{q0} \sin \omega_e t}{2K_e} - \tilde{\theta} \cos 2\omega_e t}_{-\nu} \tag{4.22}$$

where the second and third terms on the right-hand side of the approximation in (4.22) can be considered as noise, ν. Hence, if filters are not used, a noise term

arises in the error signal which is proportional to i_{q0}. The amplitude of this noise, ω_ν, can then, from (4.8), be calculated as

$$\omega_\nu = \left| G_{\nu,\tilde{\omega}_r}(j\omega_e)\frac{i_{q0}}{2K_e} \right| = \frac{\rho^2|i_{q0}|}{2K_e\omega_e} = \frac{2\rho^2 L_d L_q |i_{q0}|}{\Delta L V_e}. \tag{4.23}$$

Note that ω_e is cancelled as it also appears as ω_e^{-1} in K_e. As a numerical example, consider the PMSM of which parameters are given in Appendix B. Assume that the voltage $V_e = 0.2$ pu is allowed for high-frequency signal injection. A very moderate demand is that when the PMSM is operated at base current, the amplitude of the noise on the speed estimate should be less than 0.01 pu (note that this noise will be also present during steady-state conditions), i.e., $\omega_\nu \leq 0.01$ pu at $i_{q0} = I_{\text{base}} = 1$ pu. From (4.23), the following limit on the bandwidth of the estimator is then obtained:

$$\rho \leq \sqrt{\frac{\omega_\nu \Delta L V_e}{2L_d L_q I_{\text{base}}}} \tag{4.24}$$

With the parameters assumed above, this gives the limit $\rho \leq 0.04$ pu. The limit imposed on ρ, with this set of motor parameters (saturation of L_q is neglected) and the selection of V_e, is fairly strong. In the experiments, choosing $\rho = 0.1$ pu has often been used (see also Section 4.5.1). Therefore, sensorless operation of the PMSM utilizing signal injection without filters is not recommended for the PMSM used in the experiments. For other drives, (4.24) can be used to predict if filters are needed when utilizing signal injection. However, as shown below, the quality of the estimates, especially at transients, is improved significantly if low- and high-pass filters are used.

Operation Without a Low-Pass Filter

As discussed above, the dc component of i_q will add additional noise to the error signal. If a high-pass filter, with a very low angular cut-off frequency, is added, the dc component will be effectively removed during steady-state conditions. However, consider a stepwise change in i_q^{ref}. In vehicle applications, where the effective inertia of the shaft of the PMSM typically is large, the rotor speed will increase very slowly (as compared to the time scale of the estimator dynamics). Since the cut-off frequency of the high-pass filter is low, the corresponding (stable) poles are located close to the origin and therefore, transients will be removed slowly. Hence, although the high-pass filter will remove the dc component arising in the error signal completely, it will be clearly apparent initially and add noise the estimates (speed and rotor position). It can therefore be expected that the quality of the estimates, when

operation with only a high-pass filter, will be good during steady-state conditions, but noise will arise during current transients.

Fig. 4.5 shows simulation results of the speed-estimation error, $\tilde{\omega}_r$, where fixed speed, $\omega_r = 0.025$ pu, is set and $i_d = i_q = 0$ at $t = 0$ s. The parameter errors $\tilde{L}_q = -0.2L_q$, $\tilde{L}_d = -0.2L_d$, $\tilde{R}_s = 0.5R_s$ are assumed and the bandwidths of the current loop and estimator are set to $\alpha_c = 1$ pu, $\rho = \alpha_c/10$. At $t = 0.01$ s, i_q^{ref} is changed to $i_q^{\mathrm{ref}} = 0.5$ pu. The carrier frequency is set to $\omega_e = 10$ pu and $V_e = 0.1$ pu.

In Fig. 4.5a), neither the high- or low-pass filters are used. As seen, there is a steady-state noise in $\tilde{\omega}_r$ with an amplitude of approximately 0.05 pu. This agrees fairly well with (4.23) which predicts an amplitude of approximately 0.04 pu. A second-order Butterworth high-pass filter with an angular cut-off frequency, $\omega_{\mathrm{hp}} = 0.025$ pu (corresponding to 5 Hz), is now added, and the results are shown in Fig. 4.5b). As mentioned above, the high-pass filter removes the dc-component in an exponential rate so noise arises initially in $\tilde{\omega}_r$, but vanishes in the steady state. In Fig. 4.5c), no high-pass filtering is being done, but a low-pass filter is added. In order not to degrade the performance of the estimator, the angular cut-off frequency of the low-pass filter is set to $\omega_{\mathrm{lp}} = 5\rho$ (see also Section 4.3.5). As seen, the major part of the noise arising in $\tilde{\omega}_r$ vanishes, but some noise is still apparent even in the steady state. In the results shown in Fig. 4.5d), both the high- and low-pass filters are used and the noise in $\tilde{\omega}_r$ is very small and vanishes in the steady state.

From the discussion above and the corresponding simulation results, it can be concluded that sensorless control for the estimator without using low- and high-pass filters is possible, although a steady-state noise will arise in the estimates. To improve the quality of the estimates, especially at current transients, it is recommended to use both low- and high-pass filters. Regarding the selection of cut-off frequencies for the filters, see Section 4.3.5.

4.3.2 Impact of Inductance Saturation

The inverter is not an ideal voltage source and cannot produce the ideal carrier voltage $V_e \cos \omega_e t$. Also, the filters used in (4.18) to obtain e_{si} should be of low order (first or second) in order to reduce the amount of computations for the DSP used in the implementation. Other phenomena, such as inverter dead time and measurement errors in the current sensors, will further affect the obtained signal e_{si}. Thus, (4.18) represents a somewhat idealized situation. Nevertheless, it is important to analyze the effect of parameter variations on e_{si}, since this will affect the obtained error signal, in the actual implementation, in a similar way.

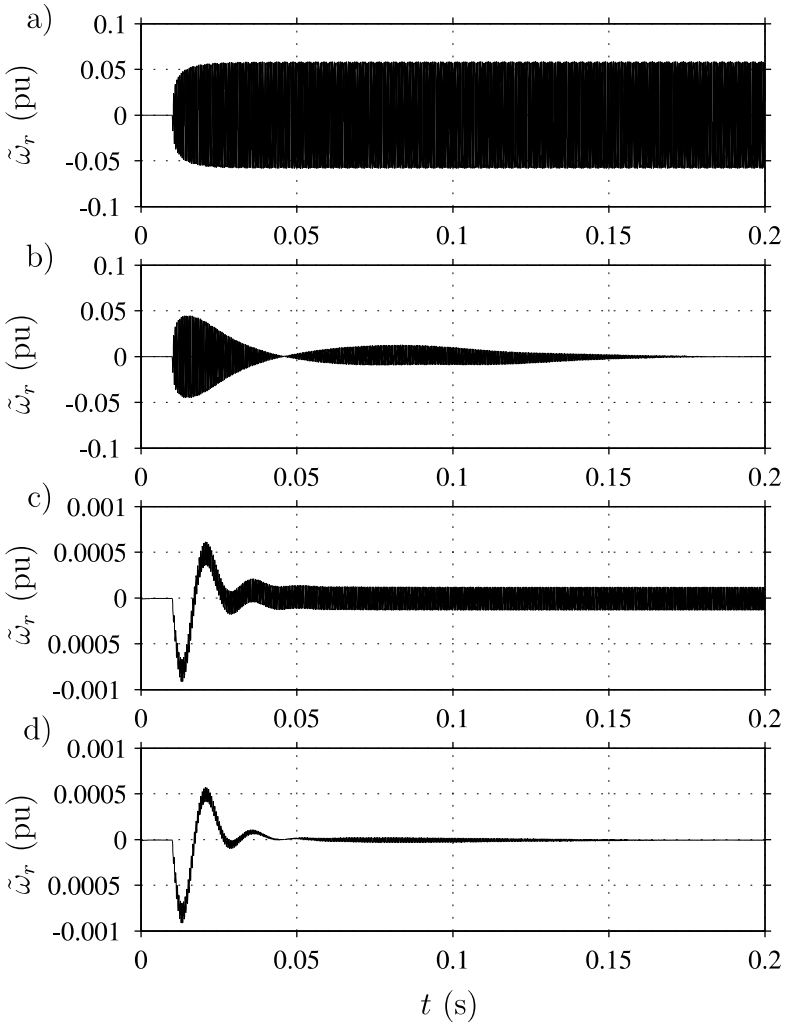

Fig. 4.5 Simulation showing the speed estimation errors arising due to a step in i_q at $t = 0.01$ s. a) Without low- and high-pass filters. b) With high-pass filter only. c) With low-pass filter only. d) With high- and low-pass filters.

As shown above, the impact of the stator resistance is minor, so $K_e' \approx K_e$ is typically a good approximation. With the selection of the gain constants given by (4.7), the error dynamics, when using (4.20) as error signal, are found to be

$$\dot{\tilde{\omega}}_r = -\frac{K_e}{2\hat{K}_e}\rho^2 \sin 2\tilde{\theta} \tag{4.25}$$

$$\dot{\tilde{\theta}} = \tilde{\omega}_r - \frac{K_e}{\hat{K}_e}\rho \sin 2\tilde{\theta}. \tag{4.26}$$

Ideally, $\hat{K}_e$ equals to K_e and the quotient $K_e/\hat{K}_e = 1$. However, since L_q saturates for large q-currents, the value of K_e will decrease for increased i_{q0}. For a saturation level of L_q given by (2.25), the quotient $K_e/\hat{K}_e$, when using a non-saturated value

of L_q when calculating $\hat{K}_e$, will decrease from $K_e/\hat{K}_e = 1$ (for $i_{q0} = 0$), down to $K_e/\hat{K}_e \approx 0.76$ for $i_{q0} = 1$ pu. The error dynamics, given by (4.25) and (4.26), can easily be linearized around the stable equilibrium point $\{\tilde{\omega}_r^\star,\ \tilde{\theta}^\star\} = \{0,\ 0\}$ by replacing $\sin\tilde{\theta}$ by $\tilde{\theta}$. The poles of the linearized error dynamics are then found as

$$p_{1,2} = -\rho\xi\left(1 \pm \sqrt{1 - \frac{1}{\xi}}\right), \quad \xi = \frac{K_e}{\hat{K}_e}. \tag{4.27}$$

Hence, for $\hat{K}_e = K_e \Rightarrow \xi = 1$, the poles (eigenvalues) of the error dynamics are given by $p_{1,2} = -\rho$, which is the desired pole placement. Fig. 4.6 shows the root loci of $p_{1,2}$ when the ξ is varied as $0.5 \leq \xi \leq 1.5$. It is seen that the damping is reduced when ξ is decreasing. This is unwanted, since it would yield a "less stable" estimator, increasing the risk of large deviations from the equilibrium point during transients. During the convergence procedure back to an equilibrium point, the estimator might converge to an equilibrium point corresponding to incorrect magnetic polarity (see below). Computing an accurate value of $\hat{K}_e$, by taking saturation of L_q into account and update $\hat{K}_e$ at each sample step is possible. A simpler solution is to calculate $\hat{K}_e$ using a saturated value of $\hat{L}_q$. The poles of the error dynamics will then be real (even for loaded conditions) and both placed near $p = -\rho$. A drawback, that typically is minor, is that the estimator will be slightly slower when L_q is not saturated than otherwise.

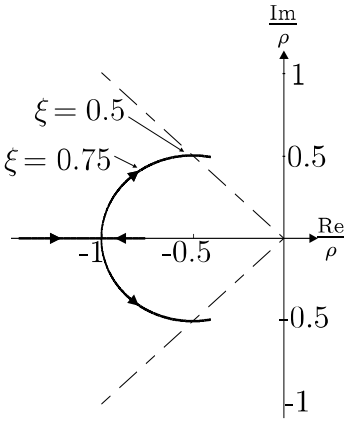

Fig. 4.6 Root loci for the linearized error dynamics (4.25) and (4.26), linearized around $\tilde{\omega}_r^\star = \tilde{\theta}^\star = 0$, when $\hat{K}_e$ is computed excluding the effect of saturation of L_q. The arrows indicate the direction of decreasing ξ.

4.3.3 Magnetic Polarity

The equilibrium points of (4.25) and (4.26) are given by $\{\tilde{\omega}_r^\star,\ \tilde{\theta}^\star\} = \{0, \frac{n\pi}{2}\}$, where the stable equilibrium points correspond to even ns. It is important to note that the

equilibrium points corresponding to $n = \pm 2, \pm 6, \pm 10, \ldots$ *also* are stable (due to the $\sin 2\tilde{\theta}$ expression). These equilibrium points correspond to a field orientation aligned to a magnetic south pole of the rotor rather than a north pole, which is incorrect. Hence, the $\hat{d}$-axis is aligned to the negative d-axis.

The fact that the signal injection method (at least as it is formulated in this thesis) is unable to determine magnetic polarity is a disadvantage, especially during a start-up procedure. Several different schemes to detect the correct magnetic polarity have been proposed in the literature. Many of these schemes rely on the fact that the saturation of L_d and L_q are different due to a smaller effective air gap for L_q. Although not covered in this thesis, some examples of methods to detect the polarity are found in [22, 34, 65].

4.3.4 Summary of Properties of the Signal Injection Method

In the opinion of the author, the signal injection method has several important properties, of which only one can be considered as an advantage. They can be summarized as follows:

1. **Potential to operate at very low, including zero, speed**
   As mentioned, speed and position estimation at zero and low speeds when utilizing back-EMF estimation methods can be considered very challenging. Although the signal injection method requires that the PMSM possesses saliency (at least in the form discussed in this thesis), the possibility to operate at zero and low speeds must be considered as a major advantage.

2. **Magnet polarity cannot be detected**
   The fact that the magnetic polarity cannot be detected directly is a disadvantage, since it requires some, perhaps time-consuming, initiation procedure to detect the true rotor position at start-up. This will increase the complexity of the estimation algorithm.

3. **Additional losses**
   Since the inverter must produce the additional high-frequency carrier voltage, this will naturally produce additional losses, both in the PMSM and inverter. The resistive losses in the stator can be estimated by solving for the steady-state solution of (4.16) assuming $\tilde{\theta} \approx 0$. The solutions are found as

$$i_{\hat{d}} = i_d = \frac{V_e \left(R_s \cos \omega_e t + \omega_e L_d \sin \omega_e t \right)}{R_s^2 + \omega_e^2 L_d^2} \tag{4.28}$$

$$i_{\hat{q}} = i_q = 0. \tag{4.29}$$

The resistive losses in the stator (solely due to the signal injection) can then be estimated as

$$P_{\text{loss,PMSM}} = \frac{3}{2}\hat{\mathbf{v}}^T\hat{\mathbf{i}} = \frac{3}{2}V_e\cos(\omega_e t)i_d \tag{4.30}$$

where the expression of i_d is given by (4.28). The mean value of P_{loss} is found as

$$\overline{P}_{\text{loss,PMSM}} = \frac{3V_e^2 R_s}{4\left(R_s^2 + \omega_e^2 L_d^2\right)} \approx \frac{3V_e^2 R_s}{4\omega_e^2 L_d^2}. \tag{4.31}$$

The rms value of the carrier current in each phase is

$$I_{\text{rms}} = \frac{i_d}{\sqrt{2}} \approx \frac{V_e}{\sqrt{2}\omega_e L_d} \tag{4.32}$$

where $R_s \ll \omega_e L_d$ is used in the approximation. The additional conducting losses in the inverter are from (3.11) and (3.14) given by

$$P_{\text{loss,inv}} \approx \frac{3V_e}{\omega_e L_d}\left(\frac{2V}{\pi} + \frac{rV_e}{2\omega_e L_d}\right). \tag{4.33}$$

Assuming $V_e = 0.1$ pu, $\omega_e = 2.5$ pu and using the inverter parameters given in Appendix B, the additional losses, consisting of $P_{\text{loss,PMSM}}$ and $P_{\text{loss,inv}}$ correspond to approximately 50 W (0.001 pu), where the major part arises due to the on-stage voltage drops of the transistor and diode. Naturally, due to the simplicity of the loss models used, this value is very approximative.

Though not considered in this thesis, additional losses in the magnet due to the high-frequency carrier injection can be estimated using finite-element methods.

4. **Reduction of available inverter voltage**
   Since the carrier voltage is added to the fundamental voltage, produced by the current controller, this reduces the available voltage that can be used for control purposes. If the signal injection method is utilized in the whole speed region, this will reduce the maximum speed that can be reached.

5. **Dependency of inverter dead time**
   For PMSMs with small saliency, as shown in [78], the voltage distortion due to the inverter's dead time can have a significant influence on the speed and position estimates. Therefore, choosing a suitable dead-time compensation method is of essence when signal injection techniques are used for PMSMs with small saliency [78].

6. **Introduction of additional parameters**
   An attractive property that simplifies the implementation of any estimator is if design rules for each parameter introduced are included. The rules (formulas) should preferably be based on parameters of the PMSM and inverter. For the signal injection method, the parameters introduced are:

   1. Amplitude of the injected carrier signal.
      The amplitude of the carrier signal, V_e, should be set so that the amplitude of the produced high-frequency current is large enough to be detected clearly by the current sensors [18]. However, increasing the carrier voltage naturally also increases losses and reduces the amount of voltage available for producing the fundamental currents.
   2. Frequency of the injected carrier signal.
      Increasing the carrier frequency, ω_e, is an advantage since, as indicated earlier, it reduces the sensitivity to the stator resistance. Results given in [71][4] also indicate that the carrier frequency should be selected as high as possible (up to the limit set by the motor parasitic effects). The limiting factor here is the inverter switching frequency which, with increased carrier frequency, limits the possibility to obtain a carrier signal with sufficient quality.
   3. Filter bandwidths.
      The error signal, e, which is obtained from e_{si} is obtained using two filters. Angular cut-off frequencies of these filters should be recommended in order to simplify the implementation.

4.3.5 Parameter Selections for the Signal Injection Method

To obtain proper estimates with the signal injection method, the amplitude and frequency of the injected carrier frequency must be chosen correctly, as well as bandwidths of the low- and high pass filters utilized. Rules of thumb for the selection of these parameters can be determined as follows.

First, the frequency of the carrier signal is limited by the switching frequency, f_{sw}. Thus, keeping $\omega_e \leq \omega_{\mathrm{sw}}/10$ will produce a carrier voltage of high quality. However, the carrier frequency must also be set high enough so that it does not affect the current controller. These two demands are somewhat contradictory, since it is

[4]The paper contains a sensitivity analysis, with respect to rotor position, of the transfer function between the injected carrier voltage and its corresponding high-frequency current.

often natural to increase the current controller bandwidth, α_c, to obtain as fast dynamic response as possible. Selecting ω_e at least five times higher than α_c will keep the carrier frequency sufficiently separated from the current control loop. Thus, ω_e should be selected as

$$5\alpha_c \leq \omega_e \leq \omega_{\mathrm{sw}}/10. \tag{4.34}$$

Due to high harmonic content in the magnetic-flux linkage and inductances, it is sometimes desired to increase the current controller bandwidth as much as possible to obtain sinusoidal currents. A result of this can be that the lower limit in (4.34) can be hard to fulfill.[5] In this case, it can be recommended to reduce the lower limit and replace the decoupling elements $\pm\hat{\omega}_r L_{d,q} i_{d,q}$ in the current controller with their reference values, i.e., $\pm\hat{\omega}_r L_{d,q} i_{d,q}^{\mathrm{ref}}$. With this choice, the current controller will be less sensitive to the high-frequency carrier current at the cost of a higher impact of cross coupled currents during current transients.

Remark: Since the carrier frequency is perfectly known, the carrier frequency visible in the current signals fed to the current controller could also be removed by adding a notch filter. This technique is, however, not utilized in this thesis.

The amplitude of the injected carrier current, proportional to V_e, must be high enough so that it can be detected with good accuracy from the current measurement. In order to reduce the effects of current sensor and analog-to-digital-quantization noise, it is natural to select the maximum amplitude of the current containing the error signal (given by (4.21)) at least larger than five percent of base current, since it will then be accurately sensed by the current sensors. This gives the following rule for the selection of V_e:[6]

$$V_e \geq \frac{I_{\mathrm{base}}\omega_e L_d L_q}{10\Delta L}. \tag{4.35}$$

Remark: When utilizing (4.35) to select V_e, the impact of the quality of the current sensors, as described above, has a large influence and should be taken into account.

The bandwidth of the high-pass filter, ω_{hp}, should be selected very low, typically a few Hertz, to remove only the dc component in i_q. Regarding the selection of ω_{lp}, a rule of thumb is to select ω_{lp} 5–10 times larger than ρ, in order to avoid degrading the performance of the estimator.

[5] As a numerical example, consider a desired rise time of 1 ms for the closed-loop current control. The closed-loop current bandwidth (expressed in SI units) is then $\alpha_c = \ln 9/(1\cdot 10^{-3})$. With the recommendation in (4.34), the carrier frequency should not be lower than $f_e \geq 5\alpha_c/(2\pi) \approx 1700$ Hz.

[6] With the setup of motor parameters for the PMSM used in the experiments and a carrier frequency of $f_e = 500$ Hz, this gives $V_e \geq 0.15$ pu, which corresponds to 28 V.

4.4 Back-EMF Estimation

Above low speeds, the back EMF becomes significant and rotor position information can be obtained using a back-EMF estimate. Error signals, suitable for the estimator, can be obtained as follows.

The voltage equation in rotor-fixed dq-coordinates is given by (4.12), where $\mathbf{Z}$ and $\mathbf{L}$ are defined in (4.13). Using the set of estimated rotor coordinates, (4.12) can be expressed as

$$\begin{aligned}\hat{\mathbf{v}} &= e^{\mathbf{J}\tilde{\theta}}\left(\mathbf{Z}+p\mathbf{L}\right)e^{-\mathbf{J}\tilde{\theta}}\hat{\mathbf{i}} + e^{\mathbf{J}\tilde{\theta}}\omega_r\boldsymbol{\psi}_m \\ &= e^{\mathbf{J}\tilde{\theta}}\mathbf{Z}e^{-\mathbf{J}\tilde{\theta}}\hat{\mathbf{i}} - e^{\mathbf{J}\tilde{\theta}}\mathbf{L}\left(\mathbf{J}(\omega_r-\hat{\omega}_r)e^{-\mathbf{J}\tilde{\theta}}\right)\hat{\mathbf{i}} + e^{\mathbf{J}\tilde{\theta}}\mathbf{L}e^{-\mathbf{J}\tilde{\theta}}p\hat{\mathbf{i}} + e^{\mathbf{J}\tilde{\theta}}\omega_r\boldsymbol{\psi}_m. \qquad (4.36)\end{aligned}$$

Selecting the bandwidth (gain) of the estimator, ρ, a decade lower than the bandwidth of the closed-loop current dynamics, α_c, the current dynamics can safely be neglected (i.e., $p = d/dt = 0$). Since accurate current control is assumed, $\hat{\mathbf{v}}$ is the output voltage from the inverter. Hence, $\hat{\mathbf{v}} = [v_d^{\text{ref}}\ v_q^{\text{ref}}]^T$ can be assumed. An error vector, $\mathbf{e} = [e_d\ e_q]^T$, can now be obtained by subtracting the resistive and rotational voltage drops from $\hat{\mathbf{v}}$ as

$$\mathbf{e} = \hat{\mathbf{v}} - \hat{\mathbf{Z}}\hat{\mathbf{i}}, \quad \hat{\mathbf{Z}} = \begin{bmatrix}\hat{R}_s & -\hat{\omega}_r\hat{L}_q \\ \hat{\omega}_r\hat{L}_d & \hat{R}_s\end{bmatrix}. \qquad (4.37)$$

In component form, e_d and e_q are computed as

$$e_d = v_d^{\text{ref}} - \hat{R}_s i_d^{\text{ref}} + \hat{\omega}_r\hat{L}_q i_q^{\text{ref}} \qquad (4.38)$$

$$e_q = v_q^{\text{ref}} - \hat{R}_s i_q^{\text{ref}} - \hat{\omega}_r\hat{L}_d i_d^{\text{ref}} \qquad (4.39)$$

where the measured currents (expressed in the set of estimated rotor coordinates) have been replaced by their reference values in order to reduce noise. Substituting (4.36) in (4.37), expressions for e_d and e_q are found as

$$\begin{aligned}e_d &= -\omega_r\psi_m\sin\tilde{\theta} + (\omega_r+\tilde{\omega}_r)\Delta L\sin\tilde{\theta}\left(i_d\cos\tilde{\theta} + i_q\sin\tilde{\theta}\right) \\ &\quad + \tilde{R}_s i_d - \left((\omega_r-\tilde{\omega}_r)\tilde{L}_q + \tilde{\omega}_r\Delta L\right)i_q \qquad (4.40) \\ e_q &= \omega_r\psi_m\cos\tilde{\theta} + (\omega_r+\tilde{\omega}_r)\Delta L\sin\tilde{\theta}\left(i_d\sin\tilde{\theta} - i_q\cos\tilde{\theta}\right) \\ &\quad + \tilde{R}_s i_q + \left((\omega_r-\tilde{\omega}_r)\tilde{L}_d - \tilde{\omega}_r\Delta L\right)i_d \qquad (4.41)\end{aligned}$$

where $\hat{\omega}_r$ has been replaced with $\hat{\omega}_r = \omega_r - \tilde{\omega}_r$.

Remark: If a rotor position sensor is used, no angular or speed estimation errors arise in e_d and e_q, i.e., $\tilde{\omega}_r = \tilde{\theta} = 0$. The error signals, e_d and e_q are then simplified to

$$e_d = \tilde{R}_s i_d - \omega_r \tilde{L}_q i_q \tag{4.42}$$

$$e_q = \tilde{R}_s i_q + \omega_r \tilde{L}_d i_d + \omega_r \psi_m. \tag{4.43}$$

Hence, e_d and e_q can (provided that a rotor position sensor is mounted) be used to estimate the electrical parameters of the PMSM [40, 58].

The first term on the right-hand side of (4.40) contains the factor $\sin\tilde{\theta}$, which can be used for updating the estimator. Assuming no parameter errors and a non-salient PMSM ($\Delta L = 0$), e_d is simplified to

$$e_d = -\omega_r \psi_m \sin\tilde{\theta}. \tag{4.44}$$

For this case, the proposed error signal used in the estimator is [26]

$$e = -\frac{e_d}{\hat{\omega}_r \hat{\psi}_m} = -\frac{e_d}{(\omega_r - \tilde{\omega}_r)(\psi_m - \tilde{\psi}_m)} \approx \sin\tilde{\theta} \tag{4.45}$$

where the approximation is valid assuming $\tilde{\psi}_m = \tilde{\omega}_r \approx 0$.

4.4.1 Impact of Saliency

Modification for Large d-currents

As mentioned in Chapter 2, many PMSM concepts in HEV applications have a salient rotor structure. Furthermore, they are designed to operate deep into the field-weakening region; results in [23] indicate that a base-to-maximum speed ratio between 1:3-4 is optimal. The impact of not taking large negative d-currents into account for a PMSM possessing saliency is demonstrated by studying the error dynamics of (4.1) and (4.2):

$$\dot{\tilde{\omega}}_r = -\rho^2 e \tag{4.46}$$

$$\dot{\tilde{\theta}} = \tilde{\omega}_r - 2\rho e. \tag{4.47}$$

Selecting e as in (4.45), the characteristic polynomial, $c(p)$, of (4.46) and (4.47) around the (stable) equilibrium point $\tilde{\omega}_r^\star = \tilde{\theta}^\star = 0$ is given by

$$c(p) = p^2 + 2\rho\left(1 - x + \frac{\rho \Delta L i_q}{2\omega_r \psi_m}\right) p - \rho^2(x-1) \tag{4.48}$$

where $x = \Delta L i_d/\psi_m$ and no parameter errors have been assumed. Large negative d-currents arise (due to field weakening) only for high speeds, so the approximations $|(\rho\Delta L i_q)/(2\omega_r\psi_m)| \ll |x|$ and $|(\rho\Delta L i_q)/(2\omega_r\psi_m)| \ll 1$ are reasonable. This simplifies the characteristic polynomial to

$$c(p) \approx (p+\rho)^2 - \rho(2p+\rho)x. \tag{4.49}$$

For $i_d = 0 \Rightarrow x = 0$, the poles are strictly real, both located at $p = -\rho$. However, for $i_d < 0 \Rightarrow x < 0$, the poles are moved according to

$$p_{1,2} = -\rho + \rho\left(x \pm \sqrt{x(x-1)}\right). \tag{4.50}$$

Thus, although strictly real, the poles are moved away from $p = -\rho$. At maximum speed, the d-current is opposing the total magnet flux, i.e., $i_d = -\psi_m/L_d \Rightarrow x = 1 - L_q/L_d$. With the set of motor parameters given in Appendix B, the poles are moved to $\{p_1, p_2\} \approx \{-4.3\rho, -0.6\rho\}$, i.e., the bandwidth of the estimator is reduced down to 60% of the nominal value. Depending on the saliency ratio, i.e., the quotient L_q/L_d, p_1 is moved to the left in the p-plane. This is also unwanted since, if current derivatives can be neglected when calculating e_d, the poles of the estimator must be located far to the right of $p = -\alpha_c$ in the p-plane. Hence, the result is a slower estimator which is also more sensitive to noise and current transients. This is unwanted at high speeds, since oscillations in speed and position estimates can cause the back EMF, reduced by the negative d-current, to grow larger than the available inverter voltage with an increased risk of inverter shutdown or failure.

However, the negative impact of the terms containing ΔL in (4.40) (similar to the concept *extended electromotive force* in [14]) are, with this type of estimator, taken into account by computing the error signal as

$$e = -\frac{e_d}{\hat{\omega}_r\left(\hat{\psi}_m - \widehat{\Delta L} i_d^{\text{ref}}\right)}. \tag{4.51}$$

With the selection of e as in (4.51), the characteristic polynomial around $\tilde{\omega}_r^\star = \tilde{\theta}^\star = 0$ is found as

$$c(p) = p^2 + 2\rho\left(1 + \frac{\rho\Delta L i_q}{2\omega_r(\psi_m - \Delta L i_d)}\right)p + \rho^2. \tag{4.52}$$

The assumption $|(\rho\Delta L i_q)/(2\omega_r(\psi_m - \Delta L i_d))| \ll 1$ is reasonable if very low speeds are disregarded. This simplifies the characteristic polynomial to

$$c(p) \approx (p+\rho)^2. \tag{4.53}$$

Hence, the ideal pole placement in $p_{1,2} = -\rho$ is obtained.

Low-Speed Instability due to Saliency

An interesting observation can be made regarding the low-speed properties of the estimator, if the back-EMF estimation method is relied upon. Assuming $i_d = 0$, the characteristic polynomial around the equilibrium point $\tilde{\omega}_r^\star = \tilde{\theta}^\star = 0$ are the same, regardless if e is chosen as in (4.45) or (4.51). It is simply obtained by setting $x = i_d = 0$ in either (4.48) or (4.52). The resulting polynomial becomes

$$c(p) = p^2 + 2\rho\,(1+\beta)\,p + \rho^2. \tag{4.54}$$

where $\beta = (\rho \Delta L i_q)/(2\omega_r \psi_m)$. A necessary and sufficient condition for stability is that the sign of all coefficients in the characteristic polynomial are equal. The following condition for stability is then obtained

$$2\rho\,(1+\beta) > 0. \tag{4.55}$$

Hence, the limits

$$i_q < -\frac{2\psi_m}{\rho \Delta L}\omega_r, \quad \omega_r < 0 \tag{4.56}$$

$$i_q > -\frac{2\psi_m}{\rho \Delta L}\omega_r, \quad \omega_r > 0 \tag{4.57}$$

are put on i_q in order to guarantee stability. These limits are also visualized in Fig. 4.7(a). The slope of the line, $i_q = k\omega_r$, indicating the region of instability, is also shown. The characteristic polynomial, given by (4.54), can be rewritten by introducing $p' = p/\rho$. The result is

$$c(p') = \rho^2 \left(p'^2 + 2\,(1+\beta)\,p' + 1\right). \tag{4.58}$$

As the poles are governed by $c(p') = 0$, there is no direct dependency on ρ (although it is still apparent in β). The root loci of (4.58) is shown in Fig. 4.7(b) where the parameter β has been varied as $-1 \leq \beta \leq 0.5$. For the poles to be located within 45° of the real axis, $\beta > -0.3$ which can be used as a rule for determine below which speeds signal-injection methods must be relied upon. Hence, the following rule is obtained

$$\omega_{\text{min1}} = \frac{\rho \Delta L I_{\max}}{2 \cdot 0.3 \psi_m} = \frac{5\rho \Delta L I_{\max}}{3\psi_m}. \tag{4.59}$$

As a numerical example, consider $\rho = 0.1$ pu and using the parameter of the PMSM as given in Appendix B, this gives $\omega_{\text{min1}} \approx 0.1$ pu.

The nature of this instability was derived assuming no parameter errors, which is not a reasonable assumption. However, it still demonstrates an inherent property

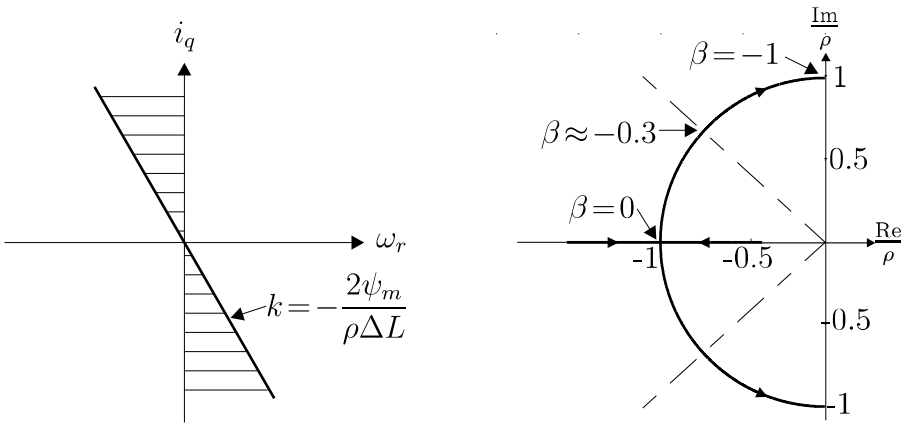

(a) Region of low-speed instability arising due to saliency. The hatched area indicates where instability arises.

(b) Root loci for (4.58) when β is varied as $-1 \leq \beta \leq 0.5$. The arrows indicate decreasing β.

Fig. 4.7 Stability region and root loci for (4.58).

of the estimator, if used a low speeds with a salient PMSM. This instability will also arise for PMSMs with round rotors since a small saliency, due to saturation, will typically arise for large torques (large i_q). This indicates that the estimator presented here, is not, in its present form, a good candidate for low-speed operation of non-salient PMSMs.

Results from simulations are shown in Fig. 4.8, where fixed speed, $\omega_r = 0.02$ pu, no harmonics and no parameter errors have been assumed. In Fig. 4.8(a), i_q is reduced down to $i_q = -(2\psi_m\omega_r)/(\rho\Delta L) + 0.1$ pu. As predicted, the error dynamics are stable, although poorly damped. In Fig. 4.8(b), i_q is reduced down to $i_q = -(2\psi_m\omega_r)/(\rho\Delta L) - 0.1$ pu. As predicted, the error dynamics become unstable.

Bifurcations

Another phenomenon, also arising due to saliency, can be observed. Assuming no parameter errors and $i_d^{\text{ref}} \approx 0$, e_d and e_q can be approximated as

$$e_d \approx -\omega_r\psi_m \sin\tilde{\theta} + \omega_r\Delta L i_q \sin^2\tilde{\theta} \tag{4.60}$$

$$e_q \approx \omega_r\psi_m \cos\tilde{\theta} - \omega_r\Delta L i_q \sin\tilde{\theta}\cos\tilde{\theta} \tag{4.61}$$

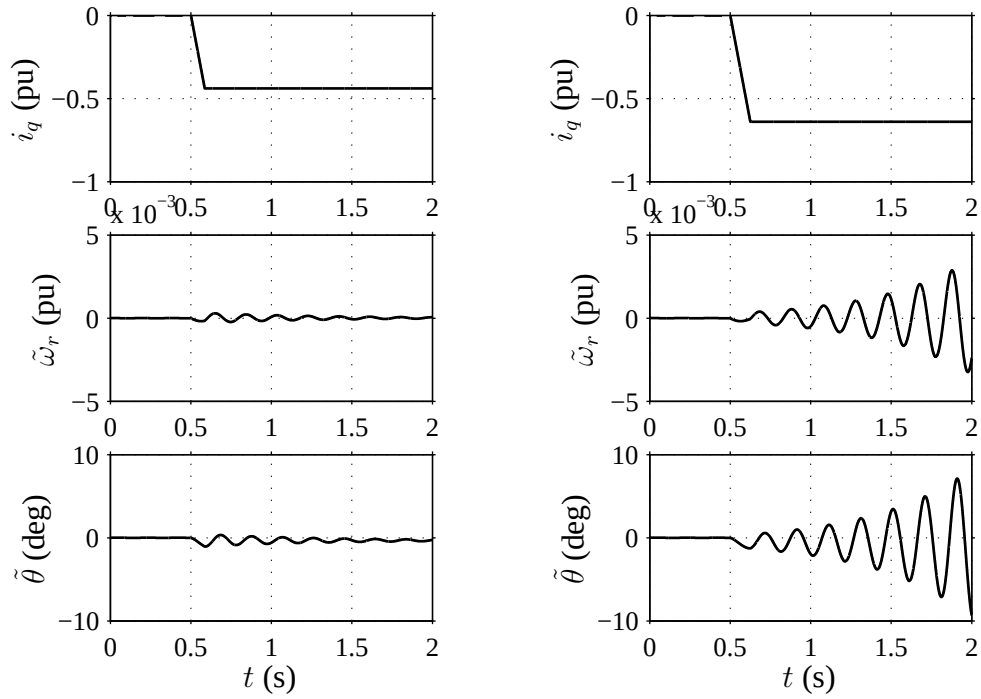

(a) $i_q > -\dfrac{2\psi_m\omega_r}{\rho\Delta L} \Rightarrow$ Stable.

(b) $i_q < -\dfrac{2\psi_m\omega_r}{\rho\Delta L} \Rightarrow$ Unstable.

Fig. 4.8 Demonstration of low-speed instability, caused by saliency. Fixed rotor speed, $\omega_r = 0.02$ pu, $\rho = \alpha_c/10 = 0.1$ pu and no parameter errors is assumed.

where $\hat{\omega}_r \approx \omega_r$ is assumed. With these approximations and using (4.51) to derive the error signal, the error dynamics are given by

$$\dot{\tilde{\omega}}_r = -\rho^2 \sin\tilde{\theta} + \frac{\rho^2\Delta L i_q \sin^2\tilde{\theta}}{\psi_m} \tag{4.62}$$

$$\dot{\tilde{\theta}} = \tilde{\omega}_r - 2\rho\sin\tilde{\theta} + \frac{2\rho\Delta L i_q \sin^2\tilde{\theta}}{\psi_m}. \tag{4.63}$$

For small error angles, $\sin^2\tilde{\theta} \approx 0$ and these terms can be neglected, yielding the desired error dynamics. This is not the case for large position estimation errors, however. The equilibrium points of (4.62) and (4.63) are given by $\{\tilde{\omega}_r^\star, \tilde{\theta}^\star\} = \{0, n\pi\}$ and

$$\tilde{\omega}_r^\star = 0 \tag{4.64}$$

$$\tilde{\theta}^\star = \begin{cases} \arcsin\left(\frac{\psi_m}{\Delta L i_q}\right) + 2\pi n \\ -\arcsin\left(\frac{\psi_m}{\Delta L i_q}\right) + (2n+1)\pi. \end{cases} \tag{4.65}$$

This extra set of equilibrium points (bifurcations) will not arise if the following inequality is fulfilled

$$|i_q| \leq \frac{\psi_m}{\Delta L}. \tag{4.66}$$

The equilibrium points corresponding to $\tilde{\theta}^\star = -\arcsin\left(\psi_m/(\Delta L i_q)\right) + (2n+1)\pi$ are stable and clearly unwanted, since they yield an erroneous field orientation. However, for the machine parameters of the experimental motor, (4.66) sets the limit $|i_q| \leq 1.4$ pu. This value is obtained by not taking saturation of L_q into account. Saturation of L_q for large q-currents will decrease the effective saliency, so $|i_q| \leq 1.3$ pu should be considered as a conservative limit.

4.4.2 Steady-State Impact of Parameter Errors

In [26], the impact of erroneous model parameters on the position estimation error was analyzed for $i_d = 0$. As mentioned previously, this is not the general case for a salient PMSM or if field weakening is utilized. Hence, the analysis is here extended to cover also the case of a nonzero i_d. As noted previously, in the steady state with $\dot{\omega}_r = 0$ and choosing the error signal, e, as in (4.51), it follows from (4.46) and (4.47) that $e = e_d = \tilde{\omega}_r^\star = 0$, i.e., there is no steady-state speed estimation error. To calculate the asymptotic rotor position estimation error, consider

$$\begin{aligned} e_d = &-\omega_r \psi_m \sin\tilde{\theta} + \omega_r \Delta L \sin\tilde{\theta}\left(i_d \cos\tilde{\theta} + i_q \sin\tilde{\theta}\right) \\ &+ \tilde{R}_s i_d - \omega_r \tilde{L}_q i_q = 0. \end{aligned} \tag{4.67}$$

For small rotor-position estimation errors, a Taylor series expansion of (4.67) around $\tilde{\theta} \approx 0$ is accurate. The asymptotic rotor-position estimation error is obtained as

$$\tilde{\theta}^\star \approx -\frac{\tilde{L}_q i_q}{\psi_m - \Delta L i_d} + \frac{\tilde{R}_s i_d}{\omega_r\left(\psi_m - \Delta L i_d\right)}. \tag{4.68}$$

For $i_d = 0$, the only sensitive parameter is L_q, while for $i_d \neq 0$, there is a singularity for $\omega_r = 0$. This clearly shows the need for a transition to the signal-injection method as the speed becomes small. With the recommendations given in [26], the value of $\hat{L}_q$ used in the estimator should be that of a saturated condition. With this choice, the first term on the right-hand side of (4.68) can be neglected, even for large i_q. With these assumptions, the minimum speed, $\omega_{\min}$, that will not yield a too large angular estimation error is given by solving for ω_r in (4.68). The following rule is obtained

$$\omega_{\min 2} = \left| \frac{\tilde{R}_s i_d}{\tilde{\theta}^\star(\psi_m - \Delta L i_d)} \right|. \tag{4.69}$$

Allowing for an angular error of 10°; for the machine used in the experiments, assuming $\tilde{R}_s = 2R_s$, (4.69) gives $\omega_{\min 2} \approx 0.05$ pu. A modification of the estimator so that it relies on signal-injection techniques at zero and low speeds and the back-EMF estimation technique at higher speeds is presented in Section 4.5.

Remark: The estimator's sensitivity to $\tilde{L}_q$ is clearly shown in (4.68). It is interesting to note that the same property also is found in [8] where speed and position is estimated using an extended Kalman filter. In [8], results from experimentes are presented to support the sensitivity to $\tilde{L}_q$ (no analytical results are presented though).

4.5 Combination of Signal Injection and Back-EMF Estimation

The two methods described in the previous sections can be combined by modifying the estimator as follows

$$\dot{\hat{\omega}}_r = \rho^2 e \tag{4.70}$$

$$\dot{\hat{\theta}} = \hat{\omega}_r + 2\rho e \tag{4.71}$$

$$e = \frac{f_{\rm tr}(\hat{\omega}_r) e_{\rm si}}{2\hat{K}_e} + [1 - f_{\rm tr}(\hat{\omega}_r)] \frac{e_d}{\hat{\omega}_r(\hat{\psi}_m - \widehat{\Delta L} i_d^{\rm ref})}. \tag{4.72}$$

Here, $\widehat{\Delta L} = \hat{L}_q - \hat{L}_d$ and $f_{\rm tr}$ is a transition function that determines which error signal to rely on. The shape of the transition function is shown in Fig. 4.9. It is similar to the weight-coefficient algorithm given in [3]. Reasonable choices are $\omega_{\rm ls} = 2\omega_{\min}$ and $\omega_{\rm hs} = 2\omega_{\rm ls}$. This modification provides a smooth transition between the two available error signals. The recommended parameter selections for the estimator, presented in Section 4.3.5 and 4.4.2, are also summarized in Table 4.1. With the recommended selections of $\omega_{\rm ls}$ and $\omega_{\rm hs}$, it can easily be verified that the position estimation error remains small for all speeds and reasonable motor parameters.

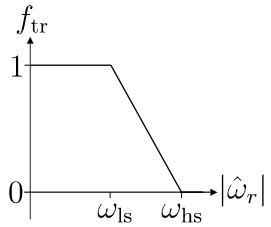

Figure 4.9: Transition function $f_{\rm tr}(\hat{\omega}_r)$.

Table 4.1: Recommended Parameter Selections

Parameter	Recommended selection
ρ	$\rho \leq \alpha_c/10$
ω_{ls}	$\max(\omega_{\mathrm{min1}}, \omega_{\mathrm{min2}})$
ω_{hs}	$2\omega_{\mathrm{ls}}$
ω_e	$5\alpha_c \leq \omega_e \leq \omega_{\mathrm{sw}}/10$
ω_{hp}	Corresponding to a few Hertz
ω_{lp}	$5\rho \leq \omega_{\mathrm{lp}} \leq 10\rho$
V_e	$V_e \geq \left(I_{\mathrm{base}}\omega_e L_d L_q\right)/(10\Delta L)$

4.5.1 Experimental Evaluation

The proposed estimator is evaluated on the PMSM of which parameters are found in Appendix B. The PMSM is current controlled and the rotor speed is maintained by the speed controller on the dc machine. The closed-loop bandwidth of the current control is set to $\alpha_c = 1.17$ pu. (corresponding to a desired current rise time of 1.5 ms) which was found to be near the upper practical limit. Estimator parameters (used in all experiment results given in this section): $\rho = 0.06$ pu, $\omega_{\mathrm{ls}} = 0.5\omega_{\mathrm{hs}} = 0.1$ pu, $\omega_e = 2.5$ pu, $\omega_{\mathrm{hp}} = 0.015$ pu, $\omega_{\mathrm{lp}} = 5\rho$, $V_e = \left(I_{\mathrm{base}}\omega_e L_d L_q\right)/(10\Delta L)$, which all are in accordance with Table 4.1. The forward difference approximation is used for discretization. The filters implemented are of second-order Butterworth type. Naturally, the true rotor position and rotor speed are measured to obtain the amount of error in the estimated speed and position.

Properties of the Transition Function

To demonstrate the properties of the transition function f_{tr}, Fig. 4.10 shows an experimental result of a slow speed reversal with high load torque. As seen, the transition between the two estimation methods is performed smoothly and only small estimation errors is observed, $|\tilde{\theta}| \lesssim 10^\circ$, $|\tilde{\omega}_r| \leq 0.01$ pu (not shown). The additional high-frequency component in i_d, due to the signal injection, is clearly seen. The predicted amplitude of this high-frequency signal is $V_e/(\omega_e L_d) \approx 0.2$ pu, which corresponds well to the results obtained from the measurements. The q-current also contains a 6th order harmonic component because of the cross coupling between i_d and i_q due to the inductance harmonics (see Section 2.1.4).

As discussed in Section 4.2, the estimator is sensitive to noise with frequencies near ρ. Noise in $\hat{\omega}_r$ is particulary crucial as it is used in the current controller. The bandwidth of the estimator is set to $\rho = 0.06$ pu. At these low speeds, the dominant noise sources are inductance- and flux-linkage harmonics of which the lowest are of

order 6 (see Section 2.1.4). Hence, the speed estimation should be most sensitive to noise for rotor speeds around $\omega_r \approx \rho/6 = 0.01$ pu, i.e., at very low rotor speeds. As seen in Fig. 4.10d), the noise content in $\tilde{\omega}_r$ is very low but, as expected, the noise content is increasing around the lowest speeds.

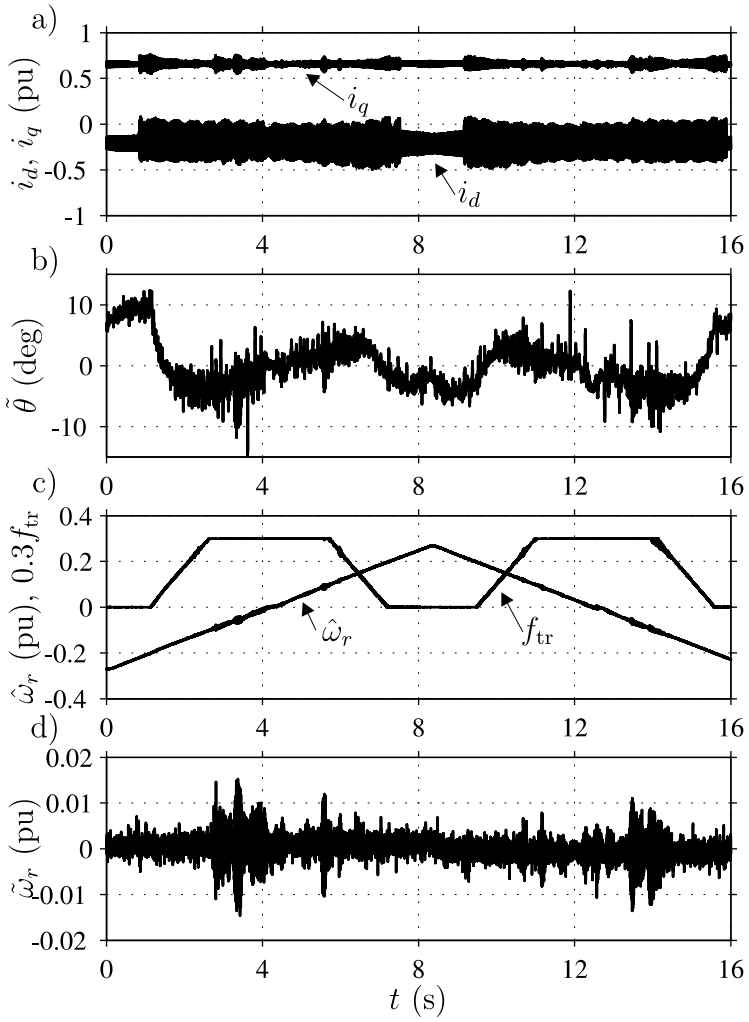

Figure 4.10: Experimental results from a slow speed reversal with high load torque.

It is interesting also to investigate the performance of the estimator when it relies equally much on both error signals, i.e., when $f_{\rm tr} = 0.5$. In Fig. 4.11, a step in i_q at $t = 0.1$ s is shown when $f_{\rm tr} \approx 0.5$. As seen, the initial current transient causes only minor influence on the angular estimation error also in this case. Due to the slow dynamics of the speed controller on the dc machine, the rotor speed is increasing, causing $f_{\rm tr}$ to drop down to zero at $t \approx 0.25$ s. Additional measurements with $i_q \leq 1$ pu have been made, showing similar results (although the rotor speed is increasing much faster due to the limitations of the speed controller on the dc machine).

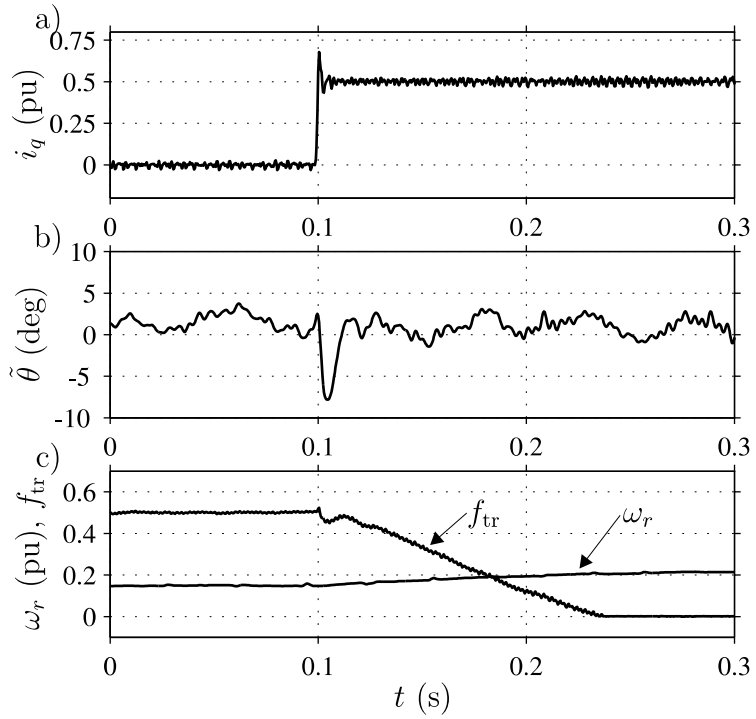

Figure 4.11: Experimental results showing the impact of a step in i_q at $f_{\rm tr} \approx 0.5$.

Vehicle Operation

The U.S. FTP-72 driving cycle, shown in Fig. 3.4a), is again chosen as a relevant driving cycle since it simulates an urban route with frequent stops [20].

Fig. 4.12 presents one-second samples of operating points for the PMSM (torque and speed). The operating points that are chosen for experimental evaluation are indicated as squares in the figure. Fig. 4.13 shows measured angular estimation errors for two electrical periods at operating points A, B, and C, respectively. Clearly, the angular estimation error is small (less than 10°) in all cases.

At rotor speeds below 0.1 pu, signal injection is utilized. Due to the frequent stops in the U.S. FTP-72 driving cycle, the drive cycle-simulation shows that the signal-injection technique is utilized in approximately 23% of the whole cycle. However, the estimated energy loss due to the signal injection in inverter and PMSM, estimated using (4.31) and (4.33), during the drive cycle is less than 0.9% of the total energy loss in the PMSM and inverter. Thus, it is reasonable to assume that the impact of additional losses in PMSM and inverter, due to the signal injection, are low in a vehicle application.

Remark: The parameters of the estimator are set according to Table 4.1 and no additional tuning is being done. Hence, the measurement results presented in

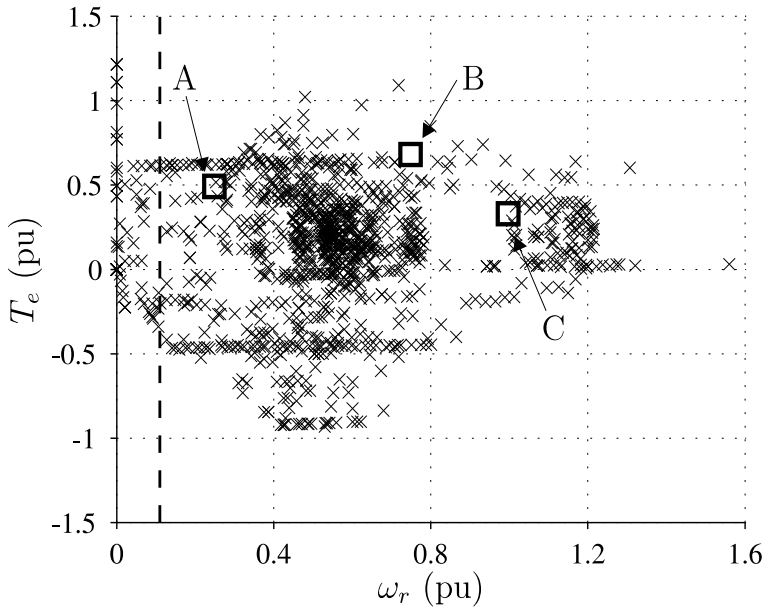

Figure 4.12: One-second samples of operating points for the PMSM in the U.S. FTP-72 driving cycle (also shown in Fig. 3.4a)). The dashed line indicates the region up to where the signal injection method is utilized.

Fig. 4.11 and Fig. 4.13 could possibly be improved somewhat further by additional (time consuming) tuning of the estimator's parameters. Other possible sources of error include inaccuracies of the current sensors and impact of dead time and additional voltage drops in the VSI. However, as the purpose of the experiments is to demonstrate significant properties of the estimator, no additional tuning is being done.

4.6 Modification for Improved Tracking

The tracking performance of the estimator for $\dot{\omega}_r \neq 0$ (accelerations) is also of importance to study. In a well-designed estimator, the bandwidth ρ should be selected so that accelerations that occur normally are tracked with only small excursions about the equilibrium point $\tilde{\omega}_r = \tilde{\theta} = 0$.

Consider a moderate, and approximately constant, acceleration (which is reasonable, seen over a short time interval); this implies adding $\dot{\omega}_r$ to the right-hand side of (4.4). Setting $\dot{\tilde{\omega}}_r = \dot{\tilde{\theta}} = 0$ in (4.4) and (4.5) and solving for $\{\tilde{\omega}_r^\star, \tilde{\theta}^\star\}$ yields the following asymptotic tracking errors

$$\tilde{\omega}_r^\star = \frac{2\dot{\omega}_r}{\rho}, \quad \tilde{\theta}^\star = \arcsin \frac{\dot{\omega}_r}{\rho^2}. \tag{4.73}$$

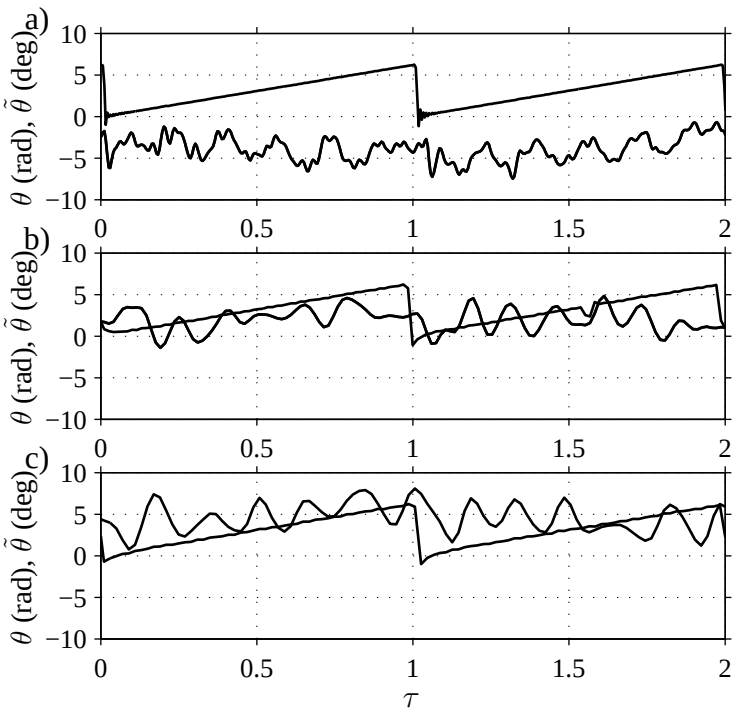

Figure 4.13: Experimental angular estimation error, $\tilde{\theta}$ in electrical degrees, and rotor angle, θ in radians, at operation points a) A, b) B, and c) C, respectively. The time is normalized with the period time T, i.e., $\tau = t/T$.

From this, a rule for selecting ρ can be obtained [26]

$$\rho = \sqrt{\frac{|\dot{\omega}_r|_{\max}}{\sin |\tilde{\theta}|_{\max}}} \tag{4.74}$$

where $|\dot{\omega}_r|_{\max}$ is the maximal *normally occurring* acceleration, while $|\tilde{\theta}|_{\max}$ is the maximum allowed transient error angle (e.g., 5° to 10°).

This, however, does not take into account rapid accelerations of short duration. An example is a vehicle where the speed changes abnormally fast at slipping or locked wheels. The result is a quick buildup of the speed estimation error. Another example is if the speed and position estimates are re-set (due to some fault) while the rotor speed is high. A similar case is the initiation of a sensorless drive if the rotor is rotating with unknown speed.

The resulting behavior of the estimator can be found by studying (4.10) and (4.11) initialized at $\tilde{\theta} \approx 0$, $|\tilde{\Omega}_r| > 0$. As discussed in Section 4.2.1, due to the dense stacking of the separatrices at $|\tilde{\Omega}_r| \geq 3$, numerous cycle slips can arise, giving a long, unacceptable, re-synchronization process.

The desired improvement can be achieved by also using the error signal e_q which, assuming no parameter errors and a non-salient machine, is, from (4.41), given by

$$e_q = \omega_r \psi_m \cos\tilde{\theta}. \tag{4.75}$$

Of interest is that $e_{\text{abs}} = \sqrt{e_d^2 + e_q^2}$ gives the modulus of the speed, regardless of $\tilde{\theta}$:

$$e_{\text{abs}} = \sqrt{e_d^2 + e_q^2} = |\omega_r|\psi_m. \tag{4.76}$$

Consequently, given that the sign of ω_r is known, (4.76) can be used to obtain an approximate speed estimation error $\tilde{\omega}_r'$

$$\tilde{\omega}_r' = \frac{e_{\text{abs}}}{\hat{\psi}_m}\text{sign}(\hat{\omega}_r) - \hat{\omega}_r. \tag{4.77}$$

This can be utilized by adding a "resetting" term to the estimator (4.70)–(4.72) as follows

$$\dot{\hat{\omega}}_r = \rho^2 e + \gamma_0(\tilde{\omega}_r')\tilde{\omega}_r' \tag{4.78}$$

$$\dot{\hat{\theta}} = \hat{\omega}_r + 2\rho e \tag{4.79}$$

$$e = \frac{f_{\text{tr}}(\hat{\omega}_r)e_{\text{si}}}{2\hat{K}_e} + [1 - f_{\text{tr}}(\hat{\omega}_r)]\frac{e_d}{\hat{\omega}_r(\hat{\psi}_m - \widehat{\Delta L} i_d^{\text{ref}})}. \tag{4.80}$$

The error dynamics can, for nominal and high speeds, with $\tilde{\omega}_r' \approx \tilde{\omega}_r$, now be expressed as

$$\dot{\tilde{\omega}}_r = -\gamma_0\tilde{\omega}_r - \rho^2\sin\tilde{\theta} \tag{4.81}$$

$$\dot{\tilde{\theta}} = \tilde{\omega}_r - 2\rho\sin\tilde{\theta}. \tag{4.82}$$

Comparing to (4.10) and (4.11), the error dynamics is now modified with the addition of the term $-\gamma_0(\tilde{\omega}_r')\tilde{\omega}_r$. As will soon be evident, $-\gamma_0(\tilde{\omega}_r')$ is chosen as

$$\gamma_0(\tilde{\omega}_r') = \begin{cases} 0, & |\tilde{\omega}_r'| \le \Delta\omega_1 \\ \frac{\rho(|\tilde{\omega}_r'| - \Delta\omega_1)}{\Delta\omega_2 - \Delta\omega_1}, & \Delta\omega_1 < |\tilde{\omega}_r'| < \Delta\omega_2 \\ \rho, & |\tilde{\omega}_r'| \ge \Delta\omega_2. \end{cases} \tag{4.83}$$

Stability of the modified error dynamics given by (4.81) and (4.82) can be shown by considering the following Lyapunov function candidate

$$V(\tilde{\omega}_r, \tilde{\theta}) = \frac{\tilde{\omega}_r^2}{2} + \rho^2(1 - \cos\tilde{\theta}) \ge 0,\ \{\tilde{\omega}_r \ne 0, \tilde{\theta} \ne n\pi\}. \tag{4.84}$$

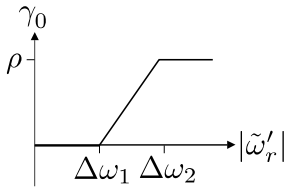

Fig. 4.14 Choice of the gain γ_0.

In order for $V(\tilde{\omega}_r, \tilde{\theta})$ to be a Lyapunov function, $\dot{V} \leq 0,\ \{\tilde{\omega}_r \neq 0, \tilde{\theta} \neq n\pi\}$. The time derivative is found as

$$\dot{V} = -\gamma_0 \tilde{\omega}_r^2 - 2\rho^2 \sin^2 \tilde{\theta} \leq 0, \{\tilde{\omega}_r \neq 0, \tilde{\theta} \neq n\pi\}. \tag{4.85}$$

Thus, V is a Lyapunov function and stability of (4.81) and (4.82) is therefore shown. Reasonable selections for $\Delta\omega_{1,2}$ are $\Delta\omega_1 = \rho$ and $\Delta\omega_2 = 2\rho$; the "resetting" term is then fully phased in when $|\tilde{\omega}_r|$ reaches the critical 3ρ. Fig. 4.15 shows the phase portrait of the modified estimator. The separatrix stacking has now disappeared. An initial speed estimation error of $|\tilde{\omega}_r| \approx 7\rho$ can now be handled without risk for cycle slips, while larger errors yield only at the most a few cycle slips (compare to Fig. 4.3).

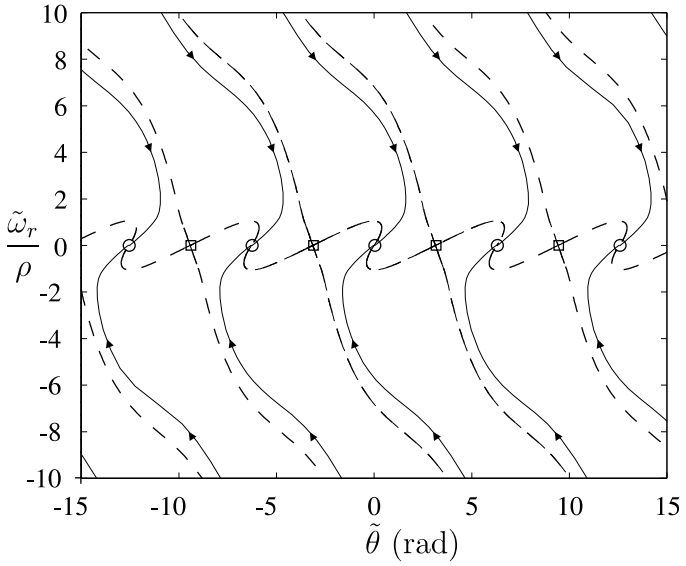

Fig. 4.15 Phase portrait of the error dynamics of the proposed estimator with "resetting term". Solid lines indicate solution curves. The dashed lines are the separatrices of the saddle points at $\{\tilde{\omega}_r, \tilde{\theta}\} = \{0, n\pi\}$, n odd, indicated by squares (□). The circles (○) mark the stable equilibrium points at $\tilde{\theta} = n\pi$, n even.

4.6.1 Limit Cycles due to Saliency

The advantage of the method to improve the tracking of the estimator was clearly seen for a machine that does not posses saliency. However, the impact of saliency should also be considered. Using (4.60) and (4.61), e_{abs} can be approximated as

$$e_{\text{abs}} = \sqrt{e_d^2 + e_q^2} \approx |\omega_r|(\psi_m - \Delta L i_q \sin\tilde{\theta}) \tag{4.86}$$

provided that $|i_q| < \psi_m/\Delta L$. Assuming $\text{sign}(\hat{\omega}_r) = \text{sign}(\omega_r)$ and $\sin^2\tilde{\theta} \approx 0$, the error dynamics are then, with $\hat{\psi}_m = \psi_m$, given as

$$\dot{\tilde{\omega}}_r \approx -\gamma_0\tilde{\omega}_r - \rho^2 \underbrace{\left(1 - \frac{\gamma_0\omega_r\Delta L i_q}{\rho^2\psi_m}\right)}_{\kappa} \sin\tilde{\theta} \tag{4.87}$$

$$\dot{\tilde{\theta}} \approx \tilde{\omega}_r - 2\rho\sin\tilde{\theta}. \tag{4.88}$$

For $\gamma_0 = 0$—i.e., for small $\tilde{\omega}_r' \approx \tilde{\omega}_r - [(\omega_r\Delta L i_q)/(\psi_m)]\sin\tilde{\theta}$—these equations are identical to (4.4) and (4.5), which is a stable system. As an indicator of the performance for large $\tilde{\omega}_r$, consider the following Lyapunov function candidate

$$V(\tilde{\omega}_r, \tilde{\theta}) = \frac{\tilde{\omega}_r^2}{2} + \kappa\rho^2(1 - \cos\tilde{\theta}). \tag{4.89}$$

The time derivative is found as

$$\dot{V} = \frac{\partial V}{\partial\tilde{\omega}_r}\dot{\tilde{\omega}}_r + \frac{\partial V}{\partial\tilde{\theta}}\dot{\tilde{\theta}} = -\gamma_0\tilde{\omega}_r^2 - 2\kappa\rho^3\sin^2\tilde{\theta}. \tag{4.90}$$

Thus, for V to be a Lyapunov function, $V > 0$ ($V = 0$ for $\tilde{\omega}_r = \tilde{\theta} = 0$) and $\dot{V} \leq 0$, it is required that $\kappa > 0$. One way of assuring this is to select ρ sufficiently large, which, however, may have the negative impact of increased noise sensitivity, as argued previously. A better alternative would be to impose the following constraint on the reference for i_q

$$|i_q^{\text{ref}}| < \frac{\rho^2\psi_m}{\gamma_0\omega_r\Delta L}. \tag{4.91}$$

But, since ω_r of course is not known in a sensorless drive, instead it is recommended to use

$$|i_q^{\text{ref}}| < \frac{\rho^2\hat{\psi}_m}{\gamma_0\omega_{\max}\widehat{\Delta L}}. \tag{4.92}$$

where $\omega_{\max}$ is the maximum occurring rotor speed. Note that this restriction vanishes when $\gamma_0 = 0$, i.e., for normal operation. Hence, if $\gamma_0 \neq 0$, arising if a large speed

estimation error occurs, the limit put on i_q (4.92) is used to simplify the convergence procedure back to an equilibrium point corresponding to $\{\tilde{\omega}_r^\star, \tilde{\theta}^\star\} = \{0, 2n\pi\}$. Hence, the limit put on i_q is not critical since during large estimation errors, large i_q will not produce a constant torque component since the field orientation is incorrect. As the estimator is converging and correct field orientation is reached, the limit put on i_q vanishes.

Through simulations it is found that limit cycles tend to occur when $\kappa < 0$, as illustrated in Fig. 4.16.

Remark: Observe that the Lyapunov function candidate (4.89) is applied to an approximation, (4.87) and (4.88), of the estimation error dynamics. Therefore, it does not give a strict proof of stability for $\kappa > 0$ (except when $\Delta L = 0$; the proof is then identical to that in [26]).

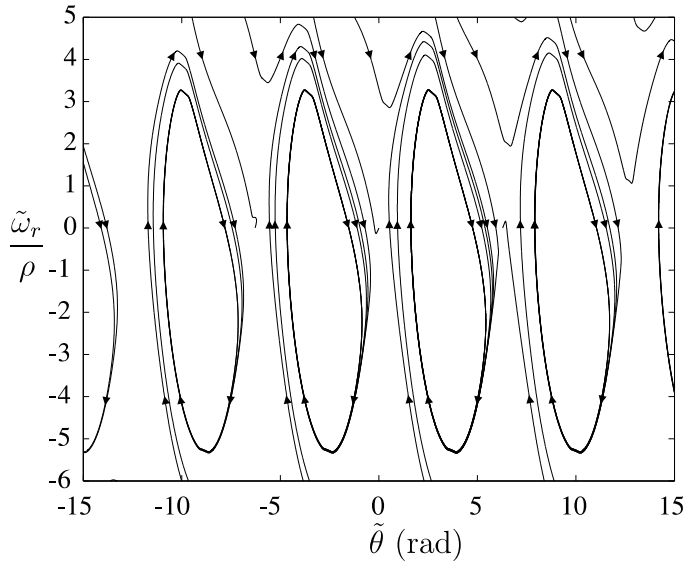

Fig. 4.16 Phase portrait of the error dynamics of the estimator using the error signals given by (4.40) and (4.41). $\rho = 0.1$ pu, $\omega_r = 1$ pu, $i_q = 2$ pu, and $i_d = 0$ pu. The presence of limit cycles is clearly seen.

4.6.2 Simulation and Experimental Evaluation

Recovery from a Large Speed Estimation Error – Simulation

To investigate the proposed estimator's capability of handling rapid accelerations, Figs. 4.17 and 4.18 show results from simulations where the rotor speed is changed rapidly from $\omega_r = 1$ pu, down to $\omega_r = 0.5$ pu at $t = 0.1$ s. The PMSM is current controlled with $i_d^{\text{ref}} = i_q^{\text{ref}} = 0$ (similar results are obtained for $i_q^{\text{ref}} \neq 0$ provided

that the limit given by (4.92) is imposed. The desired closed-loop bandwidth of the current loop is set to $\alpha_c = 1$ pu and the bandwidth of the estimator is set to $\rho = \alpha_c/10$. The parameter errors $\tilde{L}_q = -0.2L_q$, $\tilde{L}_d = -0.2L_d$ and $\tilde{R}_s = 0.5R_s$ are also introduced.

In Fig. 4.17, the parameter γ_0 is zero for all times and the large speed estimation error is not recovered from quickly. During the convergence procedure, the estimator undergoes 14 cycle slips, and large transients in i_d and i_q arise.

In the simulation results shown in Fig. 4.18, the parameter γ_0 is activated and the speed estimation error is recovered from quickly, no cycle slips arise and only small transients arise in i_d and i_q.

Recovery from a Large Speed Estimation Error – Experiment

In this experiment, the rotor speed is controlled by a dc machine, connected to the shaft of the PMSM. The purpose of the experiment is to demonstrate how a large speed estimation error can be quickly recovered from as a consequence of the added "resetting term." The speed is adjusted to $\omega_r = 0.32$ pu and the PMSM is current controlled with the references $i_d^{\text{ref}} = i_q^{\text{ref}} = 0$. The bandwidth of the current controller is set to $\alpha_c = 0.87$ pu and the bandwidth of the estimator is selected as $\rho = \alpha_c/30$. At $t = 0.05$ s, $\hat{\omega}_r$ is set to zero, yielding a large speed estimation error, $\tilde{\omega}_r = \omega_r$.

Fig. 4.19 shows an experimental result where the "resetting term" is not used, i.e., $\gamma_0 = 0$. For this case, $f_{\text{tr}} = 0$ in order not to activate the signal injection when $\hat{\omega}_r$ is small. Here, the large speed estimation error is not recovered from quickly. During the time of recovery, transients arise in i_d and i_q, which can be reduced by further increasing the bandwidth of the current controller. When the estimator has converged, it has undergone five cycle slips.

Fig. 4.20 shows an experimental result of the proposed estimator. The large estimation error vanishes quickly (within 50 ms) due to the "resetting term." Small transients in i_d and i_q occur due to the estimation error. For clarity, also the phase portrait of the two experiments is shown in Fig. 4.21, which corresponds well to Figs. 4.3 and 4.15.

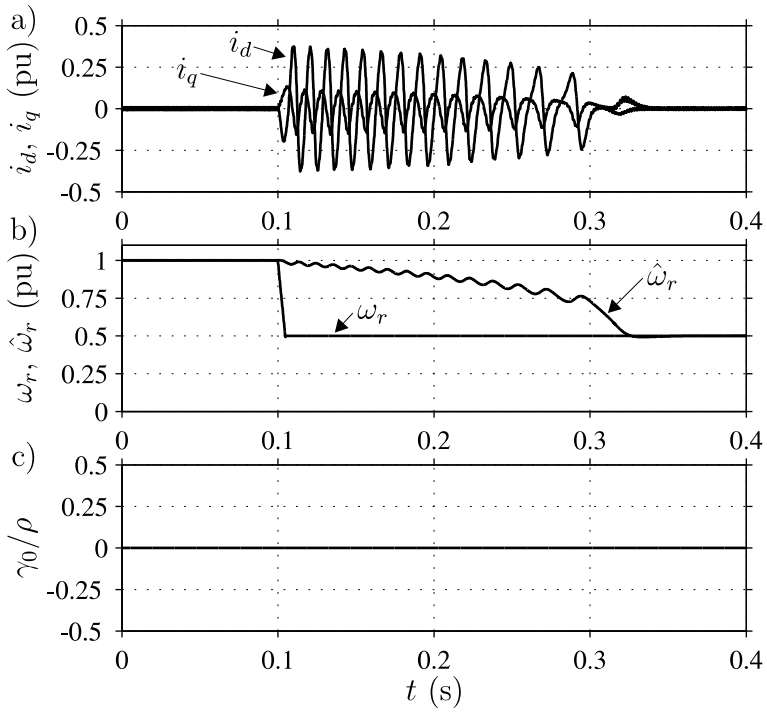

Fig. 4.17 Simulation of recovery from a large speed estimation error with $\gamma_0 = 0$.

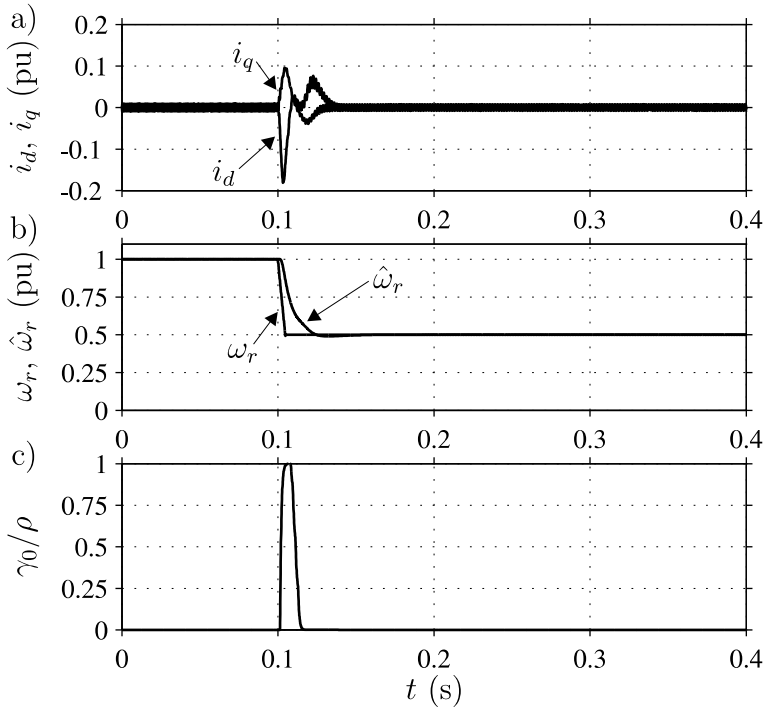

Fig. 4.18 Simulation of recovery from a large speed estimation error with γ_0 given by (4.83).

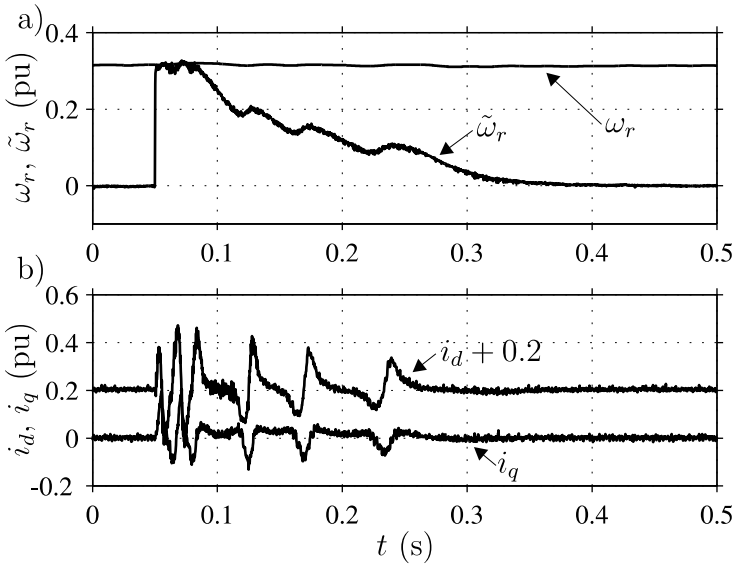

Figure 4.19: Experimental evaluation of recovery from a large speed estimation error with $\gamma_0 = 0$.

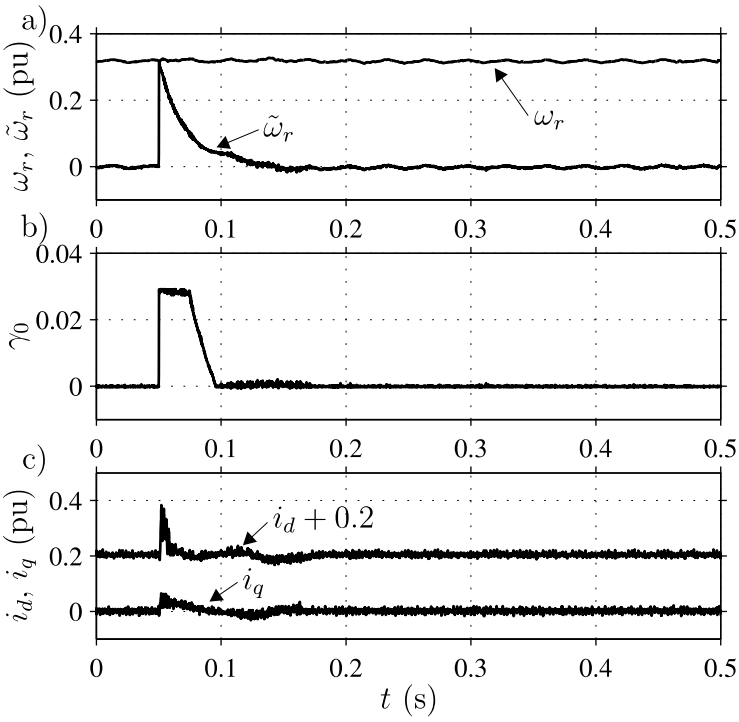

Figure 4.20: Experimental evaluation of recovery from a large speed estimation error with γ_0 given by (4.83).

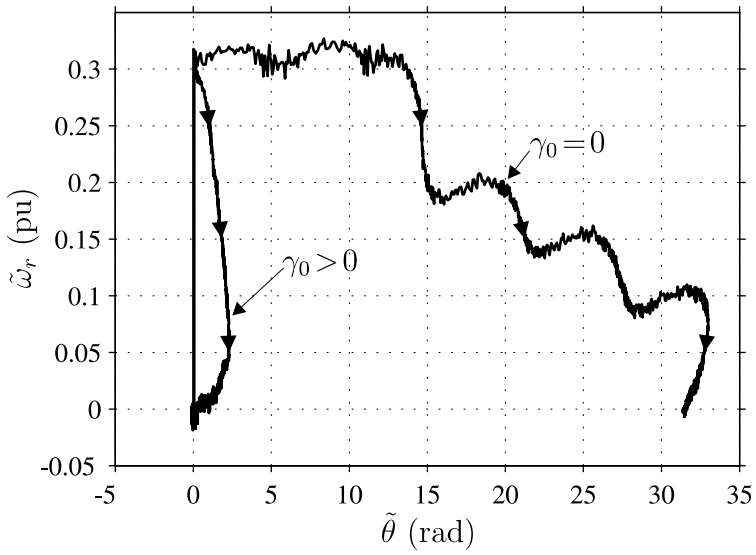

Figure 4.21: Phase portrait of the experimentally evaluated error dynamics.

4.7 Summary of Chapter

In this chapter, the PLL-type speed and position estimator, previously developed by Harnefors and Nee, was investigated further, particulary with respect to parameter variations and the impact of saliency. Modifications were proposed for use in an HEV application which requires operation in the whole speed region, including zero speed. Recommended selections for each parameter introduced were given, simplifying the implementation since the tuning procedure is avoided. A "resetting term," with the gain factor γ_0 was added, which improved the estimator's ability to handle large speed estimation errors. The results of the experimental setup showed that the estimator works properly. This indicates that the algoritm, with the modifications presented, is suitable in electric vehicle applications.

Chapter 5

Conclusions

5.1 Summary

In this thesis, control algorithms for PMSM drives used in EV and HEV applications, were studied. Particular focus was on operation without a rotor position sensor, i.e., sensorless control. In a vehicle application, the PMSM must operate at very different operating points, including zero speed with large torques and at very high speeds, thus utilizing field-weakening techniques. Therefore, the attention was on analysis of the estimation algorithm with respect to the different operating conditions that may arise.

The following summarizes the most important conclusions from Chapter 4, regarding sensorless control of salient PMSMs.

- The PLL-type algorithm, originally presented in [26], was modified to allow for operation at all speeds (including zero speed).
- The resulting error dynamics, that govern the speed and position estimation errors, were analyzed with respect to both parameter variations and shifting operation conditions. The impact of saliency, that reduces the robustness of the estimator if not taken into account, was highlighted and modifications were proposed to circumvent these issues.
- A modification was proposed to improve the estimator's capacity of handling large speed estimation errors. Situations in which this can arise include rapid accelerations and the initialization of the estimator when the initial rotor speed is unknown.
- Simple parameter selection rules were derived for the estimator, thus elimi-

nating the amount of trial-and-error tuning needed to implement the estimator. The results obtained from measurements, using these selection rules, were of good quality with only small transient and steady-state estimation errors.

The following summarizes the most important conclusions from Chapters 2 and 3.

- The selection rule of the integral gain of the field-weakening controller presented in [27] (considering induction motors) was verified with a similar analysis, but considering salient PMSMs.
- A transient model that takes harmonics into account was reviewed, and its impact on current harmonics, when utilizing synchronous-frame PI current controllers, was verified, both through simulations and experiments.
- The theory reviewed (and somewhat extended) in Chapter 3, on loss minimization by means of control, can be useful as a tool when designing the control system of any electrical drive consisting of a PMSM and VSI.

5.2 Proposed Future Work

This thesis has considered control algorithms for electrical drives in EV and HEV applications. As always, there are many more interesting aspects that can be considered.

Regarding the development of speed and position estimation techniques, an interesting issue is the development of estimators capable of low and zero-speed operation of PMSMs with small (or zero) saliency. Due to increased potential to utilize the compartment space as well as reduced mechanical complexity, electrical in-wheel motors are promising candidates for propulsion in future EVs and HEVs. Analysis and design of control algorithms for this application is therefore recommended. Examples of interesting issues are experimental studies of the impact of loss minimization control, the correct management of a common dc-link voltage feeding each motor and the detection and handling of faults (in the inverters or electrical machines) by means of control.

Appendix A

Per-Unit System

The base values of the per-unit system used in the present thesis are given in Table A.1. The system is intended for a motor with rated current I_n, rated electric angular frequency ω_n, and n_p pole pairs. The available inverter voltage is used as base voltage.

Table A.1: Base values of the per-unit system.

Base value	Denomination	Definition
Base voltage	V_{base}	$V_{\text{max}} = \frac{V_{\text{dc}}}{\sqrt{3}}$
Base current	I_{base}	$\sqrt{2} I_n$
Base impedance	Z_{base}	$\frac{V_{\text{base}}}{I_{\text{base}}}$
Base angular frequency	ω_{base}	$2\pi f_n$
Base flux	ψ_{base}	$\frac{V_{\text{base}}}{\omega_{\text{base}}}$
Base inertia	J_{base}	$\frac{V_{\text{base}} I_{\text{base}}}{\omega_{\text{base}}^3}$
Base power	P_{base}	P_n
Base torque	T_{base}	T_n

Appendix B

Laboratory Setup and Data of PMSM and VSI

B.1 Laboratory Setup

Fig. B.1 shows a schematic diagram of the laboratory setup used in the experiments and which parameters also been used in the simulations in this thesis. The PMSM is connected to a dc machine through a 3.09:1 reduction gearbox (GB). The dc machine is fed through a thyristor inverter and can be both speed and torque controlled. A torque sensor is mounted on the shaft of the PMSM to measure the mechanical torque (T_{mech}). The output flow rate (q_{v}) as well as input (T_{in}) and output (T_{out}) temperature of the cooling water are available for calorimetric measurements.

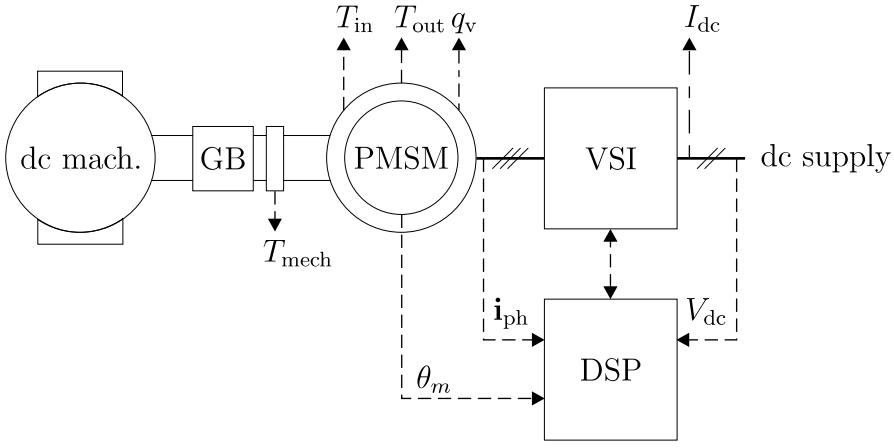

Figure B.1: Laboratory setup. Thick lines indicate power cables while dashed lines indicate measurement signals.

The VSI is fed by a dc supply (0–450 V). Conducting voltage drops and dead

time of the inverter are compensated for [44, 81]. The dc-link voltage (V_{dc}), phase currents ($\mathbf{i}_{\mathrm{ph}}$) and resolver angle (θ_m) are available signals for the DSP, which controls the VSI. The dc current (I_{dc}) is also available for measurements. The control algorithms are written in the C language and downloaded to the DSP (Texas Instruments TMS320c30). The voltage references to the VSI are modulated digitally and sent from the DSP to the VSI via optic fibers. The DSP is also equipped with 8 analog output channels for signals that are desired to be fed to the measurement system.

A more thorough description of the laboratory setup can be found in [45].

B.2 Data of the PMSM and VSI

The nominal values of the PMSM are given in Table B.1. The parameters of the PMSM are given in Table B.2. Corresponding per-unit values are also given. The per-unit system used is defined in Appendix A.

Table B.1: Nominal values of the PMSM.

Connection	Y	
No. of pole pairs	n_p	2
Rated current	I_n	160 A
Rated frequency	f_n	200 Hz
Rated power	P_n	50 kW
Rated torque	T_n	80 Nm

Table B.2: Parameters of the PMSM (cold, condition).

Stator res. ($f=0$ Hz)	R_s	7.9 mΩ	$\Leftrightarrow$	0.010 pu
d-axis inductance	L_d	0.23 mH	$\Leftrightarrow$	0.35 pu
q-axis inductance (non sat.)	L_q	0.56 mH	$\Leftrightarrow$	0.86 pu
q-axis inductance ($i_q=1$ pu)	L_q	0.42 mH	$\Leftrightarrow$	0.65 pu
Magnet flux linkage	ψ_m	104 mWb	$\Leftrightarrow$	0.71 pu
6:th harm. d-axis	$\psi_{d,6}$	2.1 mWb	$\Leftrightarrow$	0.014 pu
12:th harm. d-axis	$\psi_{d,12}$	0.5 mWb	$\Leftrightarrow$	0.0034 pu
6:th harm. q-axis	$\psi_{q,6}$	6.0 mWb	$\Leftrightarrow$	0.041 pu
12:th harm. q-axis	$\psi_{q,12}$	1.2 mWb	$\Leftrightarrow$	0.0082 pu

The parameters of the VSI are given in Table B.3, where the values are adapted from the manufacturers data sheet [57].

Table B.3: Parameters of the VSI.

Type	Mitsubishi PM600DSA060
$I_{c,\mathrm{nom}}$	600 A
r_{CE}	2.7mΩ
V_{CEO}	0.9 V
$E_{\mathrm{on}} + E_{\mathrm{off}}$	306 mJ
r_T	2.5mΩ
V_T	0.84 V
E_{rr}	15 mJ

Appendix C

Derivation of the Analytical Loss Minimization Condition

In this appendix, the details of the derivation of the analytical loss minimization condition used in Chapter 3 are presented.

The left-hand side of (3.8) can be expanded, using (3.3) and (3.4), into

$$\begin{aligned}\frac{\partial P_{\text{loss,PMSM}}}{\partial i_d} = 3 \Bigg[& \frac{\omega_r^2 L_q^2 R_c \left(R_c i_q - \omega_r (L_d i_d + \psi_m)\right) \left(R_c \frac{\partial i_q}{\partial i_d} - \omega_r L_d\right)}{(R_c^2 + \omega_r^2 L_d L_q)^2} \\ & + \frac{\omega_r^2 L_d R_c ((L_d i_d + \psi_m) R_c + \omega_r L_d L_q i_q) \left(R_c + \omega_r L_q \frac{\partial i_q}{\partial i_d}\right)}{(R_c^2 + \omega_r^2 L_d L_q)^2} \\ & + R_s \left(i_d + i_q \frac{\partial i_q}{\partial i_d}\right) \Bigg] = 0. \end{aligned} \tag{C.1}$$

Here, saturation of L_q is neglected, i.e., $\partial L_q / \partial i_q = 0$ is assumed. The expression for the partial derivative $\partial i_q / \partial i_d$ can be obtained by noting that, since the torque and rotor speed are kept constant, $\partial T_e / \partial i_d = 0$ must hold for constant ω_r. Evaluating $\partial T_e / \partial i_d = 0$ using (3.6), the partial derivative is found as

$$\begin{aligned}\frac{\partial i_q}{\partial i_d} = & \left[(2\Delta L (L_d i_d + \psi_m) - 2\Delta L^2 i_d - L_q \psi_m) R_c^2 \omega_r - \omega_r^3 L_d L_q^2 \psi_m \right. \\ & \left. - \Delta L R_c i_q (R_c^2 - \omega_r^2 L_d L_q) \right] / \left[R_c ((\Delta L i_d - \psi_m) R_c^2 + 2\omega_r \Delta L L_q R_c i_q \right. \\ & \left. - \omega_r^2 L_q ((\Delta L + L_q)\psi_m - L_d \Delta L i_d)) \right]. \end{aligned} \tag{C.2}$$

Substituting (C.2) in (C.1) and solving for $i_d(i_q)$, the loss-minimization condition

that minimizes the electrical losses is obtained as

$$\begin{aligned} i_d(i_q) = \big[&(-2i_q(L_d+L_q)\Delta L R_c^2\omega_r(R_c^2R_s+\omega_r^2L_dL_q(R_c+R_s)) \\ &+\psi_m R_c(R_c^4R_s+R_c^2(2\Delta L^2R_c-3L_q\Delta LR_c+L_q^2(R_c+2R_s))\omega_r^2 \\ &+\omega_r^4L_q^2(L_q^2-\Delta L^2)(R_c+R_s))-\{R_c(R_c^2+\omega_r^2L_dL_q)^2((4i_q^2\Delta L^2 \\ &+\psi_m^2)R_c^5R_s^2-4\omega_r\Delta L(2L_q-L_d)i_q\psi_mR_c^4R_s^2+2R_c^3R_s(L_q\Delta L\psi_m^2(-R_c \\ &+R_s)+4L_q^2\Delta L^2(R_c+R_s)i_q^2-4L_q\Delta L^3(R_c+R_s)i_q^2+2\Delta L^4i_q^2(R_c \\ &+R_s)+L_q^2\psi_m^2(R_c+R_s))\omega_r^2-4i_qL_q\Delta L(2L_q^2-L_q\Delta L \\ &+\Delta L^2)\psi_mR_c^2R_s(R_c+R_s)\omega_r^3+L_q^2R_c(R_c+R_s)(L_d^2(4i_q^2\Delta L^2 \\ &+\psi_m^2)R_c+(4L_d^2\Delta L^2i_q^2+(2L_q-L_d)^2\psi_m^2)R_s)\omega_r^4 \\ &-4L_d^2L_q^3\Delta Li_q\psi_m(R_c+R_s)^2\omega_r^5)\}^{1/2})\big] \,/\, \big(2R_c\Delta L(R_c^4R_s+ \\ &\omega_r^2L_d^2R_c^3-\omega_r^4L_d^2L_q^2(R_c+R_s)\big)\,. \end{aligned} \tag{C.3}$$

Hence, the solution, $i_d(i_q)$, given by (C.3), will minimize the total losses. As seen, the solution is very complicated and hardly usable in a DSP implementation. To demonstrate the validity of the solution, $i_d(i_q)$ is computed in the limits $R_c \to \infty$ and $\omega_r \to 0$ (corresponding to no core losses and zero speed respectively). The results are

$$\lim_{R_c\to\infty} i_d(i_q) = \lim_{\omega_r\to 0} i_d(i_q) = \frac{\psi_m}{2\Delta L} - \sqrt{\left(\frac{\psi_m}{2\Delta L}\right)^2 + i_q^2} \tag{C.4}$$

As expected, the well-known max torque-per-ampere solution is obtained in both cases, see also Fig. 3.1. An analytical max torque-per-ampere solution, taking saturation of L_q into account, can be found in [50].

Appendix D

Sample Software Implementation

The piece of C code below implements the current controller with incorporated field-weakening control for operation above base speed. Speed and position is estimated using the estimator presented in Chapter 4. Declarations of constants, variables and certain functions are not shown. The limit on i_q^{ref}, (4.92), is not included. Forward difference discretization with the sample period `Ts` is used.

```
//Speed and position estimation**********************
te=te+Ts*we;  //Compute added high-frequency signal
if (te>TwoPi)  te=te-TwoPi;
udhf=Ve*cos(te);
iqhpf=hpf(iq);         //High-pass filter iq
esidem=iqhpf*sin(te);  //Demodulate
esi=lpf(esidem);       //Low-pass filter esi

//Compute Lq taking saturation into account
Lq=Lqcomp(iqref);

ed=vd+Lq*wh*iqref-Rs*idref;  //Compute ed
eq=vq-Ld*wh*idref-Rs*iqref;  //Compute eq
eabs=sqrt(ed*ed+eq*eq);      //Compute eabs

//Compute approximate speed est. error
wrt=(eabs/psi)*(fsign(wh))-wh;
if (fabs(wrt)<dw1)  //Compute g0
  g0=0.0;
else {
```

```
  if (fabs(wrt)>dw2)
    g0=rho;
  else
    g0=(rho/(dw2-dw1))*(fabs(wrt)-dw1);

ed=ed/(-wh*(psi-(Lq-Ld)*idref));

//Compute transition function
ftr=ftrans(wh,wls,whs);
e=(ftr*esi)/(2.0*Ke)+(1.0-ftr)*ed;

//Update estimates
wh+=Ts*(rho*rho*e+g0*wrt);
th+=Ts*(wh+2.0*rho*e);
if (th<-pi) th+=2*pi;
if (th>pi)  th-=2*pi;
sinth=sin(th+1.5*Ts*wh);  //Compute sinth and costh
costh=cos(th+1.5*Ts*wh);

//Transform to the dq-reference frame
abc2dq (i1,i2,i3,sinth,costh,&id,&iq);
//End of estimation algorithm************************

//Current control incorporating field weakening******
wfw=wfwcomp(wh);

//Max torque per amp including saturation of Lq
idrefnom=maxTi(iqref);
gf=af/(2*wfw*Ld*Vmax);
//Reduce idref if available voltage is insufficient
idref+=Ts*gf*(Vmax*Vmax-vd*vd-vq*vq);
//Limit idref
if (idref>idrefnom)  idref=idrefnom;
if (idref<-imax)     idref=-imax;

iqzero=read_ad(iqzero);  //Find iqref from A/D-input
iqref=iqzero;
```

```
//Limit iq if mode B operation
if (idref*idref+iqzero*iqzero>imax*imax)
    iqref=fsign(iqzero)*sqrt(imax*imax-idref*idref);

ed_curr=idref-id;
eq_curr=iqref-iq;
//Compute ideal voltages
vd=kid*xd+kpd*ed_curr-wh*Lq*iq-Rad*id;
vq=kiq*xq+kpq*eq_curr+wh*Ld*id-Raq*iq;
vabs=sqrt(vd*vd+vq*vq);  //Limit voltages
if(vabs>Vmax)
{
    ud=(vd*Vmax)/vabs;
    uq=(vq*Vmax)/vabs;
}
else
{
    ud=vd;
    uq=vq;
}
xd+=Ts*(ed_curr+(ud-vd)/kpd);  //Back calculation
xq+=Ts*(eq_curr+(uq-vq)/kpq);

//Add additional carrier voltage
if (fabs(wh)<=1.1*whs)  ud=ud+udhf;
//End of current control*****************************
dq2abc(ud,uq,sinth,costh,&ua,&ub,&uc);
pwm(ua,ub,uc);
```

Appendix E

Glossary of Symbols, Subscripts, Superscripts and Abbreviations

Symbols

$\mathbf{A}$	system matrix
B_r	radial flux density
b	viscous damping constant
$\mathbf{E}$	back-EMF vector
E_{off}	transistor turn-off energy
E_{on}	transistor turn-on energy
E_{rr}	diode reverse recovery energy
e	control error
$\mathbf{F}$	controller transfer function matrix
f_{sw}	switching frequency
f_{tr}	transition function
G, $\mathbf{G}$	transfer function and transfer function matrix
$\mathbf{I}$	identity matrix
I	current or integration state
$I_{c,\text{nom}}$	nominal transistor current
i, $\mathbf{i}$	current and current vector
$i_{d,\max(T/i)}$	max torque-per ampere curve
$\mathbf{J}$	rotational matrix, $\mathbf{J} = \begin{bmatrix} 0 & -1 \\ 1 & 0 \end{bmatrix}$
J	inertia
j	imaginary unit, $\sqrt{-1}$
K	Park-transformation scaling constant or gain constant

k_i	integration gain
k_p	proportional gain
L, $\mathbf{L}$	inductance and inductance matrix
l_s	length of stator
N	turn distribution
N_s	number of turns in each phase
n_p	number of pole pairs
P	power
$P_{s,D}$	diode switching losses
$P_{s,T}$	transistor switching losses
p	d/dt
R	resistance
r_{CE}	transistor lead resistance
r_s	inner radius of stator
r_T	diode lead resistance
$\mathbf{S}$	sensitivity function
$\mathbf{T}_{dq,\mathrm{ph}}$	Park transformation matrix
T	period time, temperature or torque
T_e	electro-mechanical torque
T_{fric}	friction torque
T_L	load torque
t	time
t_r	rise time
V	Lyapunov function or voltage
V_{CEO}	transistor on stage voltage
V_{T0}	diode on stage voltage
v, $\mathbf{v}$	voltage and voltage vector
$\mathbf{W}$	decoupling transfer function matrix
W	coenergy
$\mathbf{x}$	state vector
Z, $\mathbf{Z}$	impedance and impedance matrix
α	bandwidth
γ	gain constant
ΔL	$\Delta L = L_q - L_d$
θ	electrical rotor angle
ϑ	rotor magnet angle
ξ	denotes a relative quantity

ρ	gain constant
ϱ	conductor-density distribution angle
τ	normalized time
τ_m	magnet pitch
ψ, $\boldsymbol{\psi}$	flux linkage and flux linkage vector
ω	angular frequency
ω_e	angular frequency of the high-frequency carrier signal
ω_r	electrical rotor speed
$\cdot$	d/dt
$\hat{}$	estimated
$\tilde{}$	error
$-$	modified, resulting

Subscripts

a	active damping or phase a component
b	phase b component
c	core, current or phase c component
cl	closed loop
co	core component
cond	conducting
d	direct axis component
fric	friction
fw	field weakening
hp	high pass (filter)
in	input (power)
L	load
loss	losses
lp	low pass (filter)
m	magnet, mutual or mechanical
n	nominal
ph	phase quantity
q	quadrature axis component
r	rotor
res	resistive
rms	root mean square
s	stator, self (inductance) or speed
ν	noise

0	zero component

Superscripts

ref	reference
T	transpose of matrix/vector
$\star$	equilibrium point

Abbreviations

batt.	battery
DSP	digital signal processor
dc	direct current
det	determinant
diag	diagonal matrix
EMF	electromotive force
EV	electric vehicle
el. mach.	electric machine
gen.	generator
HEV	hybrid electric vehicle
HPF	high-pass filter
ICE	internal combustion engine
IGBT	insulated gate bipolar transistor
IMC	internal model control
LPF	low-pass filter
max	maximal
min	minimal
PE	power electronics
PI	proportional plus integral
PLL	phase-locked loop
PMSM	permanent-magnet synchronous machine
PWM	pulse width modulation
pu	per unit
ref	reference
rms	root mean square
trans.	transmission
VSI	voltage source inverter

References

[1] F. Abrahamsen, “Energy optimal control of induction motor drives,” Ph.D. dissertation, Aalborg Univ., Aalborg, Denmark, Feb. 2000.

[2] O. Aglén, “Calorimetric measurements of losses in induction motors,” Royal Institute of Technology, Stockholm, Sweden, Licentiate Thesis, 1995.

[3] T. Aihara, A. Toba, T. Yanase, A. Mashimo, and K. Endo, “Sensorless torque control of salient-pole synchronous motor at zero-speed operation,” *IEEE Trans. Power Electron.*, vol. 14, no. 1, pp. 202–208, Jan. 1999.

[4] T. D. Batzel and K. Y. Lee, “An approach to sensorless operation of the permanent-magnet synchronous motor using diagonally recurrent neural networks,” *IEEE Trans. Energy Conversion*, vol. 18, no. 1, pp. 100–106, Mar. 2003.

[5] F. F. Bernal, A. Garcia-Cerrada, and R. Faure, “Loss-minimization control of synchronous machines with constant excitation,” in *Proc. IEEE PESC’98*, vol. 1, 1998, pp. 132–138.

[6] ——, “Determination of parameters in interior permanent-magnet synchronous motors with iron losses without torque measurement,” *IEEE Trans. Ind. Applicat.*, vol. 37, no. 5, pp. 1265–1272, Sept. 2001.

[7] N. Bianchi, S. Bolognani, and M. Zigliotto, “High-performance PM synchronous motor drive for an electrical scooter,” *IEEE Trans. Ind. Applicat.*, vol. 37, no. 5, pp. 1348–1355, Sept./Oct. 2001.

[8] S. Bolognani, L. Tubiana, and M. Zigliotto, “EKF-based sensorless IPM synchronous motor drive for flux-weakening applications,” *IEEE Trans. Ind. Applicat.*, vol. 39, no. 3, pp. 768–775, May/June 2003.

[9] F. Briz, M. W. Degner, and R. D. Lorenz, "Analysis and design of current regulators using complex vectors," *IEEE Trans. Ind. Applicat.*, vol. 36, no. 3, pp. 817–825, May/June 2000.

[10] F. Briz, A. Diez, M. W. Degner, and R. D. Lorenz, "Current and flux regulation in field-weakening operation," *IEEE Trans. Ind. Applicat.*, vol. 37, no. 1, pp. 42–50, Jan./Feb. 2001.

[11] C. C. Chan, "The state of the art of electric and hybrid vehicles," *Proc. IEEE*, vol. 90, no. 2, pp. 247–275, Feb. 2002.

[12] P. L. Chapman, S. D. Sudhoff, and C. A. Whitcomb, "Optimal current control strategies for surface-mounted permanent magnet synchronous machine drives," *IEEE Trans. Energy Conversion*, vol. 14, no. 4, pp. 1043–1050, Dec. 1999.

[13] K. T. Chau and Y. S. Wong, "Overview of power management in hybrid electric vehicles," *Energy Conversion and Management*, vol. 43, no. 15, pp. 1953–1968, Oct. 2002.

[14] Z. Chen, M. Tomita, S. Doki, and S. Okuma, "An extended electromotive force model for sensorless control of interior permanent-magnet synchronous motors," *IEEE Trans. Ind. Electron.*, vol. 50, no. 2, pp. 288–295, Apr. 2003.

[15] Y. J. Chin and J. Soulard, "A permanent magnet synchronous motor for traction applications of electric vehicles," in *Conf. Rec. IEEE-IEMDC'03*, vol. 2, 2003, pp. 1035–1041.

[16] F. Colamartino, C. Marchand, and A. Razek, "Torque ripple minimization in permanent magnet synchronous servodrive," *IEEE Trans. Energy Conversion*, vol. 14, no. 3, pp. 616–621, Sept. 1999.

[17] R. S. Colby and D. W. Novotny, "An efficiency-optimizing permanent-magnet synchronous motor drive," *IEEE Trans. Ind. Applicat.*, vol. 34, no. 3, pp. 462–469, May/June 1988.

[18] A. Consoli, G. Scarcella, and A. Testa, "Industry application for zero-speed sensorless control techniques for PM synchronous motors," *IEEE Trans. Ind. Applicat.*, vol. 37, no. 2, pp. 513–520, Mar./Apr. 2001.

[19] M. J. Corley and R. D. Lorenz, "Rotor position and velocity estimation for a salient-pole permanent magnet synchronous machine at standstill and high speeds," *IEEE Trans. Ind. Applicat.*, vol. 34, no. 4, pp. 784–789, July/Aug. 1998.

[20] Dieselnet. [Online]. Available: http://www.dieselnet.com/standards/cycles/ftp72.html

[21] K. Fukuo, A. Fujimura, M. Saito, K. Tsunoda, and S. Takiguchi, "Development of the ultra-low-fuel-consumption hybrid car-INSIGHT," *JSAE Review*, vol. 22, no. 1, pp. 95–103, Jan. 2001.

[22] J.-I. Ha, K. Ide, T. Sawa, and S.-K. Sul, "Sensorless rotor position estimation of an interior permanent-magnet motor from initial states," *IEEE Trans. Ind. Applicat.*, vol. 39, no. 3, pp. 761–767, May/June 2003.

[23] M. E. Hall and J. C. Balda, "Permanent magnet synchronous motor drive for HEV propulsion: optimum speed ratio and parameter determination," in *Proc. 56th Vehicular Technology Conf.*, vol. 3, 2002, pp. 1500–1504.

[24] L. Harnefors, M. Jansson, R. Ottersten, and K. Pietiläinen, "Unified sensorless vector control of synchronous and induction motors," *IEEE Trans. Ind. Electron.*, vol. 50, no. 1, pp. 153–160, Feb. 2003.

[25] L. Harnefors and H.-P. Nee, "Model-based current control of ac machines using the internal model control method," *IEEE Trans. Ind. Electron.*, vol. 34, no. 1, pp. 133–141, Jan./Feb. 1998.

[26] ——, "A general algorithm for speed and position estimation of ac motors," *IEEE Trans. Ind. Electron.*, vol. 47, no. 1, pp. 77–83, Feb. 2000.

[27] L. Harnefors, K. Pietiläinen, and L. Gertmar, "Torque-maximizing field-weakening control: design, analysis, and parameter selection," *IEEE Trans. Ind. Electron.*, vol. 48, no. 1, pp. 161–168, Feb. 2001.

[28] J. Hellsing, "Design and optimization of a permanent magnet motor for a hybrid electric vehicle," Chalmers University of Technology, Göteborg, Sweden, Licentiate Thesis 282L, Mar. 1998.

[29] J. R. Hendershot and T. J. E. Miller, *Design of Brushless Permanent-Magnet Motors*. Oxford, U.K.: Magna Physics Publishing and Clarendon Press, 1994.

[30] Y. Honda, T. Nakamura, T. Higaki, and Y. Takeda, "Motor design considerations and test results of an interior permanent magnet synchronous motor for electric vehicles," in *Conf. Rec. IEEE-IAS Annu. Meeting*, 1997, pp. 75–82.

[31] A. Jack, B. Mecrow, and C. Weimes, "Switched reluctance and permanent magnet motors suitable for vehicle drives-a comparison," in *IEE Seminar on Electric, Hybrid and Fuel Cell Vehicles*, 2000, pp. 6/1–6/5.

[32] T. M. Jahns, "Flux-weakening regime operation of an interior permanent-magnet synchronous motor drive," *IEEE Trans. Ind. Applicat.*, vol. IA-23, no. 4, pp. 681–689, July/Aug. 1987.

[33] T. M. Jahns and W. L. Soong, "Pulsating torque minimization techniques for permanent magnet ac motor drives—a review," *IEEE Trans. Ind. Electron.*, vol. 43, no. 2, pp. 321–330, Feb. 1996.

[34] Y. Jeong, R. D. Lorenz, T. M. Jahns, and S. Sul, "Initial rotor position estimation of an interior permanent magnet synchronous machine using carrier-frequency injection methods," in *Proc. IEEE Int. Conf. Elect. Mach. and Drives*, vol. 2, 2003, pp. 1218–1223.

[35] K. Jonasson, "Analysing hybrid drive system topologies," Lund University, Lund, Sweden, Licentiate Thesis TEIE-1031, May 2002.

[36] W. D. Jones, "Hybrids to the rescue [hybrid electric vehicles]," *IEEE Spectr.*, vol. 40, no. 1, pp. 70–71, Jan. 2003.

[37] M. P. Kazmierkowski, R. Krishnan, and F. Blaabjerg, Eds., *Control in Power Electronics—Selected Problems*. London, UK: Academic Press, 2002.

[38] M. P. Kazmierkowski and L. Malesani, "Current control techniques for three-phase voltage-source pwm converter: A survey," *IEEE Trans. Ind. Electron.*, vol. 45, no. 5, pp. 691–703, Oct. 1998.

[39] H. K. Khalil, *Nonlinear Systems*. New York, NY: Macmillan, 1992.

[40] H. Kim and R. D. Lorenz, "Improved current regulators for IPM machine drives using on-line parameter estimation," in *Conf. Rec. IEEE-IAS Annu. Meeting*, vol. 1, 2002, pp. 86–91.

[41] J.-M. Kim and S.-K. Sul, "Speed control of interior permanent magnet synchronous motor drive for the flux weakening operation," *IEEE Trans. Ind. Applicat.*, vol. 33, no. 6, pp. 43–48, Jan./Feb. 1997.

[42] P. C. Krause, O. Wasynczuk, and S. D. Sudhoff, *Analysis of Electric Machinery and Drive Systems*. Piscataway, NJ: IEEE Press, 1994.

[43] G. Kylander, "Modellering och mätning av temperatur och förluster i mindre asynkronmaskiner," Chalmers University of Technology, Göteborg, Sweden, Licentiate Thesis, 1993.

[44] M. Lindgren, "Modeling and control of voltage source converters connected to the grid," Ph.D. dissertation, Chalmers University of Technology, Göteborg, Sweden, Nov. 1998.

[45] J. Lindström, "Development of an experimental permanent-magnet motor drive," Chalmers University of Technology, Göteborg, Sweden, Licentiate Thesis 312L, Apr. 1999.

[46] R. D. Lorenz, "Practical issues and research opportunities when implementing zero speed sensorless control," in *Proc. 5th Int. Conf. Elect. Machines and Systems*, vol. 1, 2001, pp. 1–10.

[47] T. S. Low, K. J. Tseng, T. H. Lee, K. W. Lim, and K. S. Lock, "Strategy for the instantaneous torque control of permanent-magnet brushless dc drives," *IEE Proc. B*, vol. 137, no. 6, pp. 355–363, Nov. 1990.

[48] C. Mademlis and V. G. Agelidis, "High-efficiency drive due to power factor control of a permanent magnet synchronous motor," *IEEE Trans. Power Electron.*, vol. 10, no. 2, pp. 247–253, Mar. 1995.

[49] ——, "A high-performance vector controlled interior PM synchronous motor drive with extended speed range capability," in *Proc. IEEE IECON'01*, vol. 2, 2001, pp. 1475–1482.

[50] ——, "On considering magnetic saturation with maximum torque to current control in interior permanent magnet synchronous motor drives," *IEEE Trans. Energy Conversion*, vol. 16, no. 3, pp. 246–252, Sept. 2001.

[51] C. Mademlis and N. Margaris, "Loss minimization in vector-controlled interior permanent-magnet synchronous motor drives," *IEEE Trans. Ind. Electron.*, vol. 49, no. 6, pp. 1344–1347, Dec. 2002.

[52] J. Malan and M. J. Kamper, "Performance of a hybrid electric vehicle using reluctance synchronous machine technology," *IEEE Trans. Ind. Applicat.*, vol. 37, no. 5, pp. 1319–1324, Sept./Oct. 2001.

[53] D. S. Maric, S. Hiti, and C. C. Stancu, "Two improved flux weakening schemes for surface mounted permanent magnet synchronous machine drives employing space vector modulation," in *Proc. IEEE IECON'98*, vol. 1, 1998, pp. 508–512.

[54] D. S. Maric, S. Hiti, C. C. Stancu, J. M. Nagashima, and D. B. Rutledge, "Two flux weakening schemes for surface-mounted permanent-magnet synchronous drives–design and transient response considerations," in *Proc. IEEE ISIE'99*, vol. 2, 1999, pp. 673–678.

[55] K. Maruo, private communication, 2003.

[56] M. Mekhiche, S. Nichols, J. L. Kirtley, J. Young, D. Boudreau, and R. Jodoin, "High-speed, high-power density PMSM drive for fuel cell powered HEV application," in *Conf. Rec. IEEE-IEMDC'01*, 2001, pp. 658–663.

[57] "PM600DSA060 data sheet," Mitsubishi Electric, 2000.

[58] B. N. Mobarakeh, F. Meibody-Tabar, and F. M. Sargos, "On-line identification of PMSM electrical parameters based on decoupling control," in *Conf. Rec. IEEE-IAS Annu. Meeting*, vol. 1, 2001, pp. 266–273.

[59] ——, "Mechanical sensorless control of PMSM with on-line estimation of stator resistance," in *Conf. Rec. IEEE-IAS Annu. Meeting*, vol. 1, 2002, pp. 628–635.

[60] M. Morari and M. Zafiriou, *Robust Process Control*. Englewood Cliffs, NJ: Prentice Hall, 1989.

[61] S. Morimoto, K. Kawamoto, M. Sanada, and Y. Takeda, "Sensorless control strategy for salient-pole PMSM based on extended EMF in rotating reference frame," *IEEE Trans. Ind. Applicat.*, vol. 38, no. 4, pp. 1054–1061, July/Aug. 2002.

[62] S. Morimoto, M. Sanada, and Y. Takeda, "Effects and compensation of magnetic saturation in flux-weakening controlled permanent magnet synchronous motor drives," *IEEE Trans. Ind. Applicat.*, vol. 30, no. 6, pp. 1632–1637, Nov./Dec. 1994.

[63] S. Morimoto, Y. Takeda, and T. Hirasa, "Expansion of operating limits for permanent magnet motor by current vector control considering inverter capacity," *IEEE Trans. Ind. Applicat.*, vol. 26, no. 5, pp. 866–871, Sept./Oct. 1990.

[64] S. Morimoto, Y. Tong, Y. Takeda, and T. Hirasa, "Loss minimization control of permanent magnet synchronous motor drives," *IEEE Trans. Ind. Electron.*, vol. 41, no. 5, pp. 511–517, Oct. 1994.

[65] S. Östlund and M. Brokemper, "Sensorless rotor-position detection from zero to rated speed for an integrated PM synchronous motor drive," *IEEE Trans. Ind. Applicat.*, vol. 32, no. 5, pp. 1158–1165, Sept./Oct. 1996.

[66] R. Ottersten, "On control of back-to-back converters and sensorless induction machine drives," Ph.D. dissertation, Chalmers University of Technology, Göteborg, Sweden, June 2003.

[67] P. D. C. Perera, F. Blaabjerg, J. K. Pedersen, and P. Thøgersen, "A sensorless, stable V/f control method for permanent-magnet synchronous motor drives," *IEEE Trans. Ind. Applicat.*, vol. 39, no. 3, pp. 783–791, May/June 2003.

[68] A. Petersson and S. Lundberg, "Energy efficiency comparision of electrical systems for wind turbines," in *Proc. IEEE Nordic Workshop Power and Ind. Electron.*, 2002.

[69] V. Petrović, R. Ortega, A. M. Stanković, and G. Tadmor, "Design and implementation of an adaptive controller for torque ripple minimization in PM synchronous motors," *IEEE Trans. Power Electron.*, vol. 15, no. 5, pp. 871–880, Sept. 2000.

[70] V. Petrović, A. M. Stanković, and V. Blaško, "Position estimation in salient PM synchronous motors based on pwm excitation transients," *IEEE Trans. Ind. Applicat.*, vol. 39, no. 3, pp. 835–843, May/June 2003.

[71] V. Petrović, A. M. Stanković, and M. Vélez-Reyes, "Sensitivity analysis of injection-based position estimation in PM synchronous motors," in *Proc. IEEE Int. Conf. Power Electron. and Drive Systems*, vol. 2, 2001, pp. 738–742.

[72] K. M. Rahmand, B. Fahimi, G. Suresh, A. V. Rajarathnam, and M. Ehsani, "Advantages of switched reluctance motor applications to EV and HEV: design and control issues," *IEEE Trans. Ind. Applicat.*, vol. 36, no. 1, pp. 111–121, Jan./Feb. 2000.

[73] H. Rasmussen, P. Vadstrup, and H. Borsting, "Sensorless field oriented control of a PM motor including zero speed," in *Proc. IEEE Int. Conf. Elect. Mach. and Drives*, vol. 2, 2003, pp. 1224–1228.

[74] M. A. Redfern and M. J. Checksfield, "A review of pole slipping protection," in *IEE Colloquium on Gen. Prot.*, 1996, pp. 6/1–6/9.

[75] M. Schroedl, "Sensorless control of ac machines at low speed and standstill based on the "INFORM" method," in *Conf. Rec. IEEE-IAS Annu. Meeting*, vol. 1, 1996, pp. 270–277.

[76] Y. F. Shi, Z. Q. Zhu, Y. S. Chen, and D. Howe, "Influence of winding resistance on flux-weakening performance of a permanent magnet brushless ac drive," in *Proc. IEEE Int. Conf. Power Electron. Mach. and Drives*, 2002, pp. 392–397.

[77] H.-B. Shin, "New antiwindup pi controller for variable-speed motor drives," *IEEE Trans. Ind. Electron.*, vol. 45, no. 3, pp. 445–450, June 1998.

[78] C. Silva, G. M. Asher, and M. Sumner, "Influence of dead-time compensation on rotor position estimation in surface mounted PM machines using hf voltage injection," in *Proc. IEEE PCC'02*, vol. 3, 2002, pp. 1279–1284.

[79] L. Springob and J. Holtz, "High-bandwidth current control for torque-ripple compensation in PM synchronous machines," *IEEE Trans. Ind. Electron.*, vol. 45, no. 5, pp. 713–721, Oct. 1998.

[80] J. L. Stensby, *Phase-Locked Loops: Theory and Applications*. Boca Raton, FL: CRC Press, 1997.

[81] J. Svensson, "Grid connected voltage source converter-control principles and wind energy applications," Ph.D. dissertation, Chalmers University of Technology, Göteborg, Sweden, Apr. 1998.

[82] Toyota prius specification sheet. [Online]. Available: http://www.toyota.com/vehicles/2004/prius/specs.html

[83] M. N. Uddin, T. S. Radwand, and M. A. Rahman, "Performance of interior permanent magnet motor drive over wide speed range," *IEEE Trans. Energy Conversion*, vol. 17, no. 1, pp. 79–84, Mar. 2002.

[84] N. Urasaki, T. Senjyu, and K. Uezato, "A novel calculation method for iron loss resistance suitable in modeling permanent-magnet synchronous motors," *IEEE Trans. Energy Conversion*, vol. 18, no. 1, pp. 41–47, Mar. 2003.

[85] S. Vaez and M. A. Rahman, "Energy saving vector control strategies for electric vehicle motor drives," in *Proc. Conf. Power Conv.*, vol. 1, 1997, pp. 13–18.

[86] ——, “An on-line loss minimization controller for interior permanent magnet motor drives,” *IEEE Trans. Energy Conversion*, vol. 14, no. 4, pp. 1435–1440, Dec. 1999.

[87] J. Wai and T. M. Jahns, “A new control technique for achieving wide constant power speed operation with an interior PM alternator machine,” in *Conf. Rec. IEEE-IAS Annu. Meeting*, vol. 2, 2001, pp. 807–814.

[88] A. H. Wijenayake and P. B. Schmidt, “A more accurate permanent magnet synchronous motor model by taking parameter variations and loss components into account for sensorless control applications,” in *Proc. IEEE Conf. Electr. Mach. and Drives*, 1997, pp. TD–1.1–TD–1.3.

[89] L. Ying and N. Ertugrul, “A novel, robust dsp-based indirect rotor position estimation for permanent magnet ac motors without rotor saliency,” *IEEE Trans. Power Electron.*, vol. 18, no. 2, pp. 539–546, Mar. 2003.